



Universiteit  
Leiden  
The Netherlands

## Simple molecules as benchmark systems for molecular electronics

Djukić, D.

### Citation

Djukić, D. (2006, October 25). *Simple molecules as benchmark systems for molecular electronics*. Retrieved from <https://hdl.handle.net/1887/4927>

Version: Corrected Publisher's Version

License: [Licence agreement concerning inclusion of doctoral thesis in the Institutional Repository of the University of Leiden](#)

Downloaded from: <https://hdl.handle.net/1887/4927>

**Note:** To cite this publication please use the final published version (if applicable).

Simple molecules as benchmark  
systems  
for  
molecular electronics

Cover: Nano Lett. **2006** 6(4) 789-793.

Simple molecules as benchmark  
systems  
for  
molecular electronics

Proefschrift

ter verkrijging van  
de graad van Doctor aan de Universiteit Leiden,  
op gezag van de Rector Magnificus Dr. D. D. Breimer,  
hoogleraar in de faculteit der Wiskunde en  
Natuurwetenschappen en die der Geneeskunde,  
volgens besluit van het College voor Promoties  
te verdedigen op woensdag 25 oktober 2006  
te klokke 15:00 uur.

door

Darko Djukić

geboren te Tuzla, Bosnie - Herzegovina in 1974

**promotiecommissie**

Promotor: Prof. dr. J. M. van Ruitenbeek

Referent: Prof. dr. ir. H. S. J. van der Zant

Prof. dr. P. H. Kes

Prof. dr. L. J. de Jongh

Prof. dr. M. C. van Hemert

Prof. dr. Y. V. Nazarov

Dr. J. C. Cuevas

The work described in this thesis is part of the scientific program of the "Stichting voor Fundamenteel Onderzoek der Materie (FOM)" and has been made possible by financial support from the "Nederlandse Organisatie voor Wetenschappelijk Onderzoek (NWO)".

mami, tati, bratu  
u znak sećanja na baku Zrelu

# Contents

<b>1</b>	<b>General concepts</b>	<b>4</b>
1.1	Basic principles of transport through molecular orbitals . . . . .	4
1.2	Conductance quantization . . . . .	6
1.2.1	Two-dimensional electron gas and one-dimensional wire . . . . .	6
1.2.2	Scattering approach and Landauer formula for conductance . . . . .	8
1.3	Experimental techniques . . . . .	12
1.3.1	Atomic size contacts . . . . .	12
1.3.2	Conductance histograms . . . . .	14
1.3.3	Length histograms . . . . .	16
1.3.4	Point Contact Spectroscopy and Inelastic Electron Tunneling Spectroscopy . . . . .	17
1.4	Conductance fluctuations . . . . .	19
1.5	One Level Model . . . . .	21
<b>2</b>	<b>Characterization of Pt-H<sub>2</sub>-Pt molecular junctions by point contact spectroscopy</b>	<b>24</b>
2.1	Introduction . . . . .	24
2.2	Experiments with D <sub>2</sub> , H <sub>2</sub> and HD . . . . .	25
2.2.1	PCS measurements on a Pt-D <sub>2</sub> -Pt bridge . . . . .	27
2.2.2	PCS measurements on a Pt-H <sub>2</sub> -Pt bridge . . . . .	30
2.3	Correlation between the D <sub>2</sub> and H <sub>2</sub> vibration frequencies . . . . .	31
2.4	Conclusions based on the frequency distribution . . . . .	33
2.5	PCS measurements on a Pt-HD-Pt bridge . . . . .	33
2.6	Comparison with DFT model calculations - transmission . . . . .	36
2.7	Stretching dependence of the vibration modes . . . . .	38
2.7.1	Theory . . . . .	38
2.7.2	Experiment . . . . .	40
2.8	Conclusions . . . . .	42
<b>3</b>	<b>Shot Noise measurements on single atoms and molecules</b>	<b>44</b>
3.1	Motivation . . . . .	44
3.2	Introduction to shot noise . . . . .	45
3.2.1	Shot noise in mesoscopic systems . . . . .	45

3.2.2	Shot noise in point contacts . . . . .	46
3.3	Shot noise experiments on gold with MCBJ . . . . .	49
3.4	Shot noise in the current through a Pt-H <sub>2</sub> -Pt junction . . . . .	50
3.4.1	Motivation . . . . .	50
3.4.2	Experimental setup . . . . .	51
3.4.3	Testing of the setup on gold . . . . .	51
3.4.4	Measurements on a Pt-D <sub>2</sub> -Pt bridge . . . . .	55
3.5	Conclusions . . . . .	58
<b>4</b>	<b>The width of vibration signals in experiments with molecules</b>	<b>60</b>
4.1	Introduction . . . . .	60
4.2	Degeneracy of transversal modes . . . . .	61
4.3	Addition of independent broadening factors . . . . .	63
4.4	Discussion . . . . .	64
4.5	Conclusions . . . . .	67
<b>5</b>	<b>Single-molecule junctions for CO</b>	<b>68</b>
5.1	Motivation . . . . .	68
5.2	Technical aspects . . . . .	69
5.3	DC measurements on Pt-CO-Pt junctions . . . . .	70
5.3.1	Conductance histograms . . . . .	70
5.3.2	Breaking traces . . . . .	72
5.4	Model calculations . . . . .	73
5.5	Discussion of the conductance for CO . . . . .	74
5.6	Point contact spectroscopy on Pt-CO-Pt junctions . . . . .	76
5.7	Experimental results . . . . .	77
5.8	Stretching dependence . . . . .	80
5.9	Model calculations of vibration modes . . . . .	80
5.10	Discussion of the vibration modes for CO . . . . .	83
5.11	Conclusions . . . . .	85
<b>6</b>	<b>Towards larger molecules</b>	<b>86</b>
6.1	Motivation . . . . .	86
6.2	Experiments on acetylene (C <sub>2</sub> H <sub>2</sub> ) . . . . .	86
6.3	Experiments on benzene (C <sub>6</sub> H <sub>6</sub> ) . . . . .	89
6.3.1	Introducing C <sub>6</sub> H <sub>6</sub> molecules into the cryogenic environment	89
6.3.2	PCS spectra near 1G <sub>0</sub> . . . . .	90
6.3.3	PCS spectra at low conductances . . . . .	91
6.4	Conclusions . . . . .	92
<b>7</b>	<b>Anomalous dI/dV curves: a mechanism of intrinsic signal amplification</b>	<b>94</b>
7.1	Introduction . . . . .	94
7.2	Motivation: anomalous dI/dV curves . . . . .	95
7.3	The model . . . . .	96
7.3.1	Time evolution . . . . .	97

7.3.2	TLS excited by molecular vibration . . . . .	99
7.3.3	The scattering rates . . . . .	100
7.3.4	The timescales . . . . .	106
7.4	Comparison to experiments and discussion . . . . .	106
7.5	Conclusions . . . . .	109
 <b>Samenvatting</b>		<b>116</b>
 <b>List of publications</b>		<b>118</b>
 <b>Curriculum Vitae</b>		<b>119</b>

# Chapter 1

## General concepts

The work presented in this thesis is concerned with the conductance properties of atomically small junctions. The main characteristic of such junctions is that their size is much smaller than the electron coherence length  $l_e$ , so that the transport through them is quasi ballistic. Since conductance phenomena on such small scales are of special nature, we will start by introducing the principles of transport through molecules, then the concept of conductance quantization, first for a 2DEG (two dimensional electron gas) and then we will see that the same idea can be applied to single-atom contacts. Then, following the scattering model of Landauer, we derive the expression for current through a ballistic contact. In the second half of the chapter we will discuss the main measurement methods we have employed.

### 1.1 Basic principles of transport through molecular orbitals

A detailed study of the concept of transport through molecules can be found in the review (1). When analyzing transport properties of molecules, we would like to use the formalism developed for mesoscopic bulk systems which is presented below. The situation when a molecule is contacted from two sides by bulk

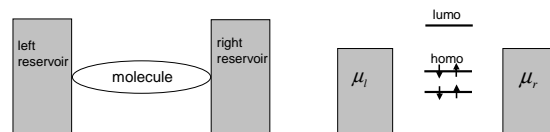


Figure 1.1: *Schematic drawing of a molecular contact. The figure on the left presents the schematic picture of a molecule situated in between the electrodes and the figure on the right presents the molecule in the form of energy levels (molecular orbitals).*

contacts is presented in Fig.1.1. The left and right contacts are bulk metals with electrochemical potentials  $\mu_l$  and  $\mu_r$ . Before contacting, the molecule has discrete energy levels which are the molecular orbitals. By coupling a molecule to bulk electrodes, the bulk metal wave functions overlap with the molecular orbitals and the strength of that coupling is given by the parameters  $\Gamma_1$  and  $\Gamma_2$  for each molecular level for the coupling to left and right lead respectively. The value of  $\Gamma$  is defined as  $\Gamma = \Gamma_1 + \Gamma_2$  and this is called the level broadening. It determines the nature of the molecular junction to a large extent. It can also be defined as  $\Gamma = \hbar/\tau$  where  $\tau$  is the time that an electron spends on the energy level before it diffuses into the leads. If the parameter  $\Gamma$  is very small, the energy levels will be only slightly broadened due to the coupling. In that case, the molecule behaves like a quantum dot which can be charged and discharged with a discrete amount of charge ( $n \cdot e$ ). If we define a parameter  $U$  as the Coulomb charging energy needed to transfer one electron from one electrode to the molecule, then the quantum dot regime will be achieved for  $U \gg \Gamma$ . In cases when  $U$  is comparable with  $\Gamma$ , the molecule is strongly coupled to the leads and only partial charge transfer is possible. That regime is called the self-consistent field regime (SCF). Figure 1.2 presents the situation when a voltage  $V$  is applied across the contact in such a way that  $\mu_r = \mu_l - eV$ . If there is a molecular level in between  $\mu_l$  and  $\mu_r$ , it will try to equilibrate with both  $\mu_l$  and  $\mu_r$ . If the level is in equilibrium with the left or right contact, it would mean that  $N_l = 2f(\epsilon, \mu_l)$  or  $N_r = 2f(\epsilon, \mu_r)$  where  $f(\epsilon, \mu) = \frac{1}{1 + e^{\frac{\epsilon - \mu}{kT}}}$ . Since the molecular level is somewhere in between  $N_l$  and  $N_r$ , the current will be determined by the rates  $\Gamma_l/\hbar$  and  $\Gamma_r/\hbar$  and the differences  $(N_l - N)$  and  $(N - N_r)$  where  $N$  is the actual average occupation of the level. The rate equations are:

$$\begin{aligned} I_l &= \frac{e\Gamma_l}{\hbar}(N_l - N) \\ I_r &= \frac{e\Gamma_r}{\hbar}(N - N_r). \end{aligned} \quad (1.1)$$

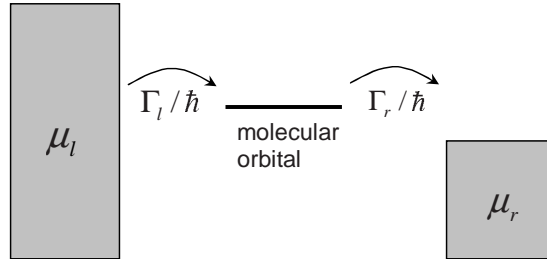


Figure 1.2: Schematic representation of conductance through a molecular level.  $\Gamma_l/\hbar$  and  $\Gamma_r/\hbar$  are the rates with which electrons are transferred between the molecular level and left and right electrode.

Since the charge is conserved,  $I_l=I_r$ , which determines the number of electron  $N$  on the molecular level:

$$N = 2 \frac{\Gamma_l f(\epsilon, \mu_l) + \Gamma_r f(\epsilon, \mu_r)}{\Gamma_l + \Gamma_r}. \quad (1.2)$$

The current through the molecule is:

$$I = \frac{2e}{\hbar} \frac{\Gamma_l \Gamma_r}{\Gamma_l + \Gamma_r} (f(\epsilon, \mu_l) - f(\epsilon, \mu_r)). \quad (1.3)$$

## 1.2 Conductance quantization

### 1.2.1 Two-dimensional electron gas and one-dimensional wire

In GaAs-AlGaAs heterostructures free electrons are confined at the interface and form a two-dimensional electron gas (2DEG). Applying an electrostatic potential to external electrodes depletes the electrons from the area underneath the electrodes, allowing one to controllably make a constriction. This separates the electron gas in three subparts: the left and right reservoir, connected by a narrow constriction of width  $W$  and length  $L \ll l_e$  the elastic scattering length. The narrow constriction has special conductance properties and is called a quantum wire. To describe the motion of an electron in such potential landscape, we start by assuming that the electron moves in an infinitely long box along the  $z$  axes, with width  $W$  along the  $x$  axes. The Schrödinger equation for electrons in cartesian coordinates is

$$-\frac{\hbar^2}{2m^*} \left[ \frac{\partial^2}{\partial x^2} + \frac{\partial^2}{\partial z^2} + V(x, z) \right] \Psi(x, z) = E \Psi(x, z)$$

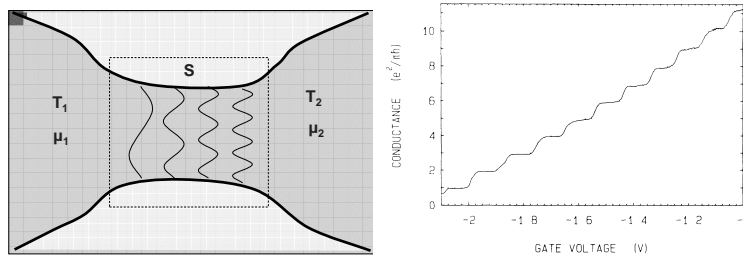


Figure 1.3: *Left: Schematic drawing of a ballistic contact. Due to the hard wall boundary conditions, the wave function is quantized in the perpendicular direction, while in the longitudinal direction it propagates as a free wave. Right: Conductance of a 2DEG point contact as a function of the gate voltage. By changing the gate voltage the width of constriction changes gradually. When the width increases by  $\lambda_F/2$ , the conductance increases by one quantum of conductance. After Ref.(2).*

where  $V(x, z)$  is the confining potential for simplicity assumed to be given by hard wall boundaries. Along the  $z$  axes electron propagates as a free wave and after solving a text book example of electrons in an infinite potential well we find that the motion in the  $x$  direction is quantized due to the hard wall boundary conditions. The eigenstates of the electron are

$$\Psi(x, z) = A\{\sin(k_x x)\} \exp^{\pm ik_z z} = A\{\sin(\frac{n_x \pi}{W} x)\} \exp^{\pm ik_z z}$$

with the eigenvalues:

$$E(k_x, k_z) = \frac{\hbar^2}{2m^*} \{k_x^2 + k_z^2\} = \frac{\hbar^2}{2m^*} \{(\frac{n_x \pi}{W})^2 + k_z^2\}$$

This means that for a given width of the constriction and given value of the Fermi energy, only a certain number of states fit in the transversal direction. By increasing the width gradually at a certain point the next mode will fit in which will be seen as a sudden step in the conductance. The basic idea of conductance quantization in a 2DEG is shown in figure 1.3 left. The first evidence of conductance quantization in 2DEG was observed by van Wees *et al.* (2) in the year 1988. The measurement results are shown in figure 1.3 right. They were able to observe 16 equally spaced steps in the conductance by changing the gate voltage from 360nm down to complete stop of the current flow. One should realize the difference between the steps in conductance due to change in the diameter of the constriction and ones created by filling of the next energy level due to increase in energy. The same effect can be achieved by using a back gate which can shift the energy levels with respect to  $E_F$ . Here, as well as in the case of 1D wires which follows, we will only consider the increase in diameter of the constrictions.

If the electron gas is confined in a such way that the electrons can propagate only along one axis, one has a one dimensional wire. One example of a such system is wire obtained in MCBJ experiments presented later in this thesis. The wave length of the transverse part of wave function of the electrons being transmitted through such a contact, similar to the case of a 2DEG point contact, will be determined by the diameter of the one dimensional wire, which for simplicity we assume to be cylindrically symmetric. In cylindrical coordinates, the transverse part can be written in the form of Bessel functions  $J_m(\gamma_{ml}r/R) \exp^{im\varphi}$  where  $\gamma_{ml}$  is the  $l$ th zero of  $m$ th order Bessel function  $J_m(x)$  with energy  $(\hbar^2/2m^*)(\gamma_{ml}/R)^2$ . Very generally, without going into the detailed calculations of energy levels (which can be found in ref.(3)), we can label the transversal energy levels as  $E_n$  and the total energy is given by  $E_n(k) = E_n + \hbar^2 k_z^2/2m^*$ . Since  $E_n$  has a discrete spectrum, the number of energy levels for which is  $E_n < E_F$  will provide the number of *transmission channels*, and each wave function with quantum numbers corresponding to a certain transmission channel is called a *mode*.

## 1.2.2 Scattering approach and Landauer formula for conductance

Conductance in point contacts can be understood using the scattering model developed by Landauer. Let us suppose that the whole problem of the conductance through a point contact can be presented by a model which consists of two macroscopic leads which we will call the reservoirs and a central region where the scattering occurs. The reservoirs are entirely classical and completely described by given temperatures  $T_1$  and  $T_2$ , and chemical potentials  $\mu_1$  and  $\mu_2$ . The distribution of the electrons in the reservoirs is determined by the Fermi-Dirac function.

In between the reservoirs we put the scattering region, which can be for example a point contact, a single molecule, a single atom or a chain of atoms. The scattering processes in the scattering region are not destroying the coherence between transmitted and reflected states, so the electron wave function remains coherent. The coupling between the reservoirs and the scattering region is through leads which have no influence on the transport, so any electronic state will be transmitted through the leads with probability 1. Let us assume that electrons can enter the scattering region through  $N$  independent modes on each side of the scattering region<sup>1</sup>. This means that they can enter either

<sup>1</sup>The number of states on left and right does not necessarily need to be the same, but this is not a significant generalization.

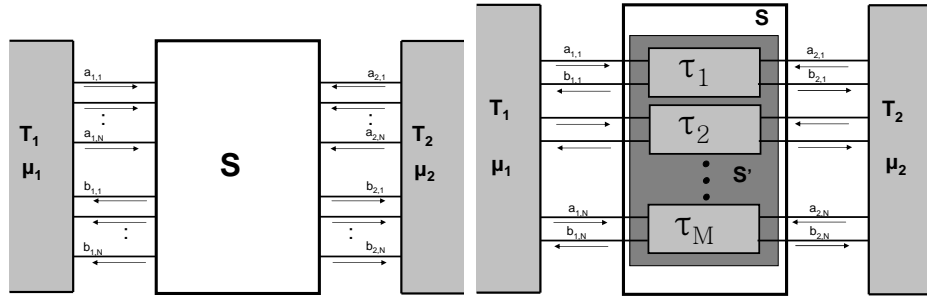


Figure 1.4: *Left: Schematic description of the scattering approach to the problem of conductance through a phase coherent conductor. Electrons are emitted from the reservoirs and transmitted through perfect leads to the scattering region where the electron wave function is partially transmitted and partially reflected. Right: Analyzing the scattering problem in an eigenbasis for the scattering matrix of a given system, one can decompose it such that it consists of  $M$  ( $m = 1 \dots M$ ) individual scattering problems in subspaces assigned by the sets of quantum numbers  $\{k^{(m)}_{\perp}, k^{(m)}_{\parallel}\}$  which now present the transport channels of the scatterer. The number of the channels  $M$  is always smaller than the number of perfect leads  $N$ . Quantum numbers  $\{k^{(m)}_{\perp}, k^{(m)}_{\parallel}\}$  will be the linear combinations of the quantum numbers  $\{k_{\perp}, k_{\parallel}\}$  originating from the states in the leads.*

from the left or right. Each of those  $2N$  states will be partially reflected and partially transmitted, so there will be  $2N$  states going out of the scattering region back to where they came from for the reflected part, and  $2N$  getting to the other reservoir, so being transmitted. The process is depicted in figure 1.4a. To summarize:

$$\begin{pmatrix} \mathbf{b}_1 \\ \mathbf{b}_2 \end{pmatrix} = \begin{pmatrix} \hat{s}_{11} & \hat{s}_{12} \\ \hat{s}_{21} & \hat{s}_{22} \end{pmatrix} \cdot \begin{pmatrix} \mathbf{a}_1 \\ \mathbf{a}_2 \end{pmatrix} \quad (1.4)$$

where  $\mathbf{a}_1$  and  $\mathbf{a}_2$  are vectors describing the amplitudes of the incoming waves from the left and right respectively. Vectors  $\mathbf{b}_1$  and  $\mathbf{b}_2$  are corresponding vectors of outgoing waves. The  $\hat{s}_{i,j}$  are matrices describing the amplitudes for scattering of the incoming waves from lead  $j$  to the outgoing waves in lead  $i$ . Explicitly, the in and out going vectors are:

$$\mathbf{a}_1 = \begin{pmatrix} a_{1,1} \\ a_{1,2} \\ \vdots \\ a_{1,n} \end{pmatrix}, \mathbf{a}_2 = \begin{pmatrix} a_{2,1} \\ a_{2,2} \\ \vdots \\ a_{2,n} \end{pmatrix}, \mathbf{b}_1 = \begin{pmatrix} b_{1,1} \\ b_{1,2} \\ \vdots \\ b_{1,n} \end{pmatrix}, \mathbf{b}_2 = \begin{pmatrix} b_{2,1} \\ b_{2,2} \\ \vdots \\ b_{2,n} \end{pmatrix}. \quad (1.5)$$

Since the total number of electrons has to be conserved, the  $S = \begin{pmatrix} \hat{s}_{11} & \hat{s}_{12} \\ \hat{s}_{21} & \hat{s}_{22} \end{pmatrix}$  matrix is unitary. It is made of four  $N \times N$  blocks. From equation (1.4) it follows that:

$$b_1 = s_{11}a_1 + s_{12}a_2, \quad b_2 = s_{21}a_1 + s_{22}a_2.$$

The diagonal blocs are reflection matrices and the off-diagonal ones are transmission matrices.

As we can see from the examples of conductance quantization in 2DEG and for simplified models of cylindrical contacts, available states for transport are identified by the perpendicular component of the wave vector  $\mathbf{k}(m)_\perp$  which is quantized due to the boundary conditions. One should make a distinction between the  $\mathbf{k}$  which is a wave vector of the electron in the lead and  $\mathbf{k}(m)$  which is the wave vector of the electron in the scattering region and it can be a linear combination of different  $\mathbf{k}$ 's. Wave functions with different  $\mathbf{k}(m)_\perp$  (same holds for  $\mathbf{k}$ 's) are linearly independent and the scatterer (in this case 2DEG or cylindrical nanowire) is linear, so, after the transmission matrix is diagonalized, the scattering between the eigen states with different  $\mathbf{k}(m)_\perp$  is forbidden. That means that each electron wave function with a particular  $\mathbf{k}(m)_\perp$  can only be transmitted with the same  $\mathbf{k}(m)_\perp$  or reflected into state with the same  $\mathbf{k}(m)_\perp$  but moving in the opposite direction. This allows us to decompose the entire problem into independent problems for each electron state, which is called a decomposition into independent conductance eigen channels. The problem for arbitrary mesoscopic contact was solved by Landauer and Bütikker (4). Applying unitary transformations

$$U = \begin{pmatrix} U_1 & 0 \\ 0 & U_2 \end{pmatrix}, V = \begin{pmatrix} V_1 & 0 \\ 0 & V_2 \end{pmatrix} \quad (1.6)$$

it is possible to transform the operator S such that it consists of 4 diagonal  $N \times N$  blocks:

$$S' = \begin{pmatrix} V_1 & 0 \\ 0 & V_2 \end{pmatrix} \cdot \begin{pmatrix} s_{1,1} & s_{1,2} \\ s_{2,1} & s_{2,2} \end{pmatrix} \cdot \begin{pmatrix} U_1 & 0 \\ 0 & U_2 \end{pmatrix} \quad (1.7)$$

$$S' = \begin{pmatrix} -ir_1^{1/2} & \cdots & 0 & t_1^{1/2} & \cdots & 0 \\ \vdots & \ddots & \vdots & \vdots & \ddots & \vdots \\ 0 & \cdots & -ir_N^{1/2} & 0 & \cdots & t_N^{1/2} \\ t_1^{1/2} & \cdots & 0 & -ir_1^{1/2} & \cdots & 0 \\ \vdots & \ddots & \vdots & \vdots & \ddots & \vdots \\ 0 & \cdots & t_N^{1/2} & 0 & \cdots & -ir_N^{1/2} \end{pmatrix} \quad (1.8)$$

The eigenvalues  $(r_1, \dots, r_N)$  and  $(t_1, \dots, t_N)$  reflection and transmission coefficients for a given channel decomposition. Since the S matrix is unitary, S' is unitary as well, so  $t_i^* t_i + r_i^* r_i = 1$ ,  $(i=1, \dots, N)$ .

The set  $(|t_1|^2, \dots, |t_N|^2)$  gives the complete characterization of the transport properties of the point contact. The set is also called the mesoscopic PIN code for the given contact.

Knowing the PIN code, we can calculate the Landauer formula for conductance. Since we know that conductance channels are independent from each other, we will derive the expression for the current through only one channel and the total current will be the sum over all conducting channels. Since the current is conserved, it can be calculated in one of the two leads only. We will take lead 1. The current operator is:

$$\hat{I}(t) = \frac{e}{\hbar} \int \int dE dE' (\hat{a}_1^\dagger(E) \hat{a}_1(E') - \hat{b}_1^\dagger(E) \hat{b}_1(E')) e^{i(E-E')t/\hbar}, \quad (1.9)$$

where the operators  $\hat{a}_\alpha^\dagger(E), \hat{a}_\alpha(E)$  and  $\hat{b}_\alpha^\dagger(E), \hat{b}_\alpha(E)$  ( $\alpha = 1, 2$ ) are creation and annihilation operators for incoming and outgoing states respectively. Since for each channel we have:

$$\begin{pmatrix} b_1 \\ b_2 \end{pmatrix} = \begin{pmatrix} s_{11} & s_{12} \\ s_{21} & s_{22} \end{pmatrix} \cdot \begin{pmatrix} a_1 \\ a_2 \end{pmatrix} \quad (1.10)$$

using the Einstein summation rule, relation (1.9) can be written as:

$$\hat{I}(t) = \frac{e}{\hbar} \int \int dE dE' (\hat{a}_1^\dagger(E) \hat{a}_1(E') - (s_{1,\alpha}^* a_\alpha^\dagger)(s_{1,\beta} a_\beta)) e^{i(E-E')t/\hbar} \quad (1.11)$$

Introducing the operator:

$$A_{\alpha\beta} = \delta_{\alpha 1}\delta_{\beta 1} - s_{1\alpha}^*s_{1\beta} \quad (1.12)$$

and taking the expected value, we obtain the expression for the current:

$$\langle \hat{I}(t) \rangle = \frac{e}{h} \int \int dE dE' A_{\alpha\beta} \langle \hat{a}_\alpha^\dagger(E) \hat{a}_\beta(E') \rangle e^{i(E-E')t/\hbar} \quad (1.13)$$

Noticing that  $\langle \hat{a}_\alpha^\dagger(E) \hat{a}_\beta(E') \rangle = f_\alpha(E) \delta_{\alpha\beta} \delta(E-E')$  where  $f_\alpha(E)$  is the Fermi-Dirac distribution function, the integration over energy  $E'$  gives:

$$\langle \hat{I}(t) \rangle = \frac{e}{h} \int dE A_{\alpha\alpha} f_\alpha(E) = \frac{e\tau}{h} \int dE (f_1(E) - f_2(E)). \quad (1.14)$$

To include the spin degeneracy, the expression for the current has to be multiplied with factor 2, which brings us to Landauer formula for conductance in a single channel conductor, at  $T=0$ :

$$I = \frac{2e^2}{h} \tau V = G_0 \tau V. \quad (1.15)$$

The constant  $G_0 = \frac{2e^2}{h} \approx 77 \mu S$  is the unit of conductance and the total conductance is obtained as the sum over all contributing channels:

$$G = G_0 \sum_{i=1}^N \tau_i \quad (1.16)$$

In the world of point contacts, as is mentioned already, transport is quasi ballistic so the resistance is not due to the scattering on impurities and defects, but due to limited ability of the contact to transport electrons. The electrons that are transported are not experiencing any difficulties passing through the single atom contact or chain of atoms if the transmission coefficient of the particular channel is  $\tau = 1$ . Electrons in such an eigen channel will form a coherent state across the whole chain of Au atoms, no matter how long it is <sup>2</sup>, so the transport through that conductance channel is ideal. The electrons in eigen channels that are not transmitted will not suffer any dissipation in contact either because they will not be transported at all. For them the conductor just does not exist. So it is more useful to speak about the conductance and transmission coefficients of ballistic conductors rather than about the resistance.

---

<sup>2</sup>The longest experimentally observed chains made of single atoms are seven atoms long and were obtained for Pt and Au(5). The ideal ballistic transmission property is expected to break down when the length approaches the inelastic scattering length.

## 1.3 Experimental techniques

### 1.3.1 Atomic size contacts

A situation similar to the one described for a 2DEG is observed in point contacts made when a metal wire of macroscopic dimensions is thinned down by pulling on the two ends. Before the wire finally breaks in two, it will be thinned down to a contact of an single atom in diameter. To break a wire in controllable way, Muller *et al.* developed a special mechanism named mechanically controllable break junction (MCBJ) (6). The basic construction of the MCBJ is very simple. A piece of wire, about 1cm long and 0.1mm in diameter is glued with epoxy glue to a phosphor bronze bending beam that is electrically isolated by a thin polymer foil. The spot between the two points where the wire is glued to the substrate is weakened by cutting a notch, which reduces the diameter by about a half, so that the wire breaks there. By pushing in the middle of the beam, as is shown in Figure (1.5), the wire is gradually thinning down until it finally breaks apart. The breaking process is first driven mechanically until the point where only a small increase in distance can break it completely. That fine breaking regime is then controlled by use of the piezo element which has a maximum expansion of about  $10\mu\text{m}$  at room temperature which reduces by a factor of 4 at 4.2K. The ratio between the elongation of piezo element and the increased distance between two arbitrary fixed points on two sides close to the point contact is usually smaller than  $3 \cdot 10^{-3}$ . This allows to increase the distance between the electrodes with a resolution of about  $10^{-4}\text{\AA}$ . For the measurements that require knowledge of the absolute values of distances between the electrodes as the function of the piezo elongation, a calibration must be obtained for each sample individually. The inset in Figure (1.5) shows a part of a computer simulation of the breaking process. Before the wire finally breaks apart a single atom contact, or even a chain of atoms can be formed between the bulk contacts.

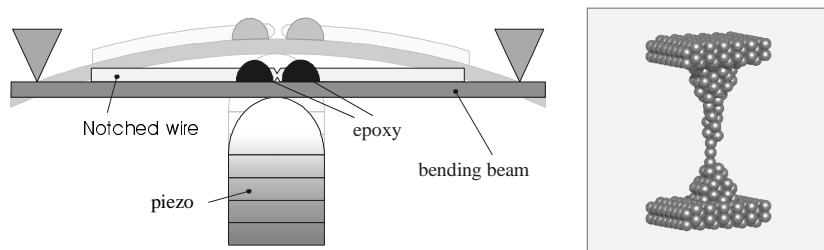


Figure 1.5: *left: Schematic drawing of a MCBJ device. A small phosphor bronze plate is electrically isolated on one side by Kapton foil. This forms a bending beam and on top of it, a sample wire is attached by Stycast epoxy. The wire can be broken in a three-point bending configuration as shown on the picture. Breaking is controlled by a piezo element. right: Numerical simulation of a configuration of the atomic contact during breaking.*

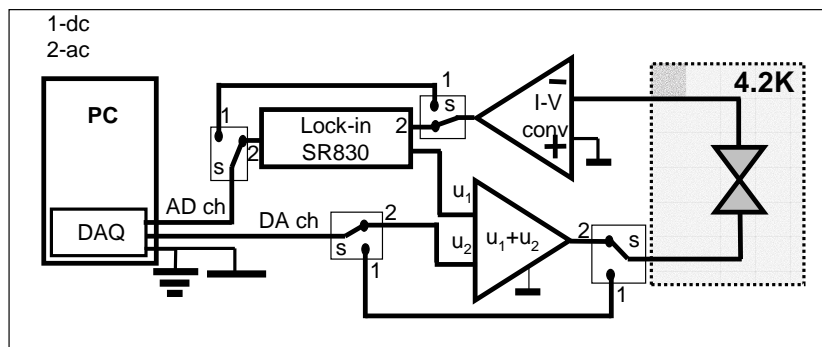


Figure 1.6: Schematic drawing of the measurement setup for dc (switches  $s$  in position 1) and ac (switches  $s$  in position 2) biased measurements. The sample is kept at  $4.2K$ . In ac measurements, a home made adder adds a dc signal from the DAC and a small ac modulation from the lock-in and provides the bias for the sample in two-point measurement configuration. The current through the circuit is converted to voltage by an I-V converter with adjustable gain  $A=10^3 - 10^7$  V/A and sent back to the lock-in, which measures the sample response to the ac modulation.

Conductance properties of such point contacts are measured by dc and ac biased measurements. The simplest schematic picture of the measurement setup is presented in Figure (1.6). If the switches  $s$  are in the positions 1, the circuit measures the dc conductance by applying a dc voltage bias and measuring the current using an I-V converter. DC biased measurements are used for conductance and length histograms presented below. In spectroscopic measurements (switches in position 2) we are interested in changes in conductance as a function of bias voltage of the order of 1-3% and still want high accuracy, by using a lock-in technique. A digital-to-analog converter as part of a National Instruments Data Acquisition Card (DAQ) provides a dc signal with 16 bits accuracy which is added to an ac modulation signal provided by a Stanford Research Lock-in amplifier SR830. In all experiments presented in this thesis, ac modulation is  $v_{mod}=1mV_{rms}$ . The adder is a home made device, especially designed to meet our low noise requirements. The total resistance of the wiring is around  $10\Omega$  which is negligible compared to the  $\sim 10k\Omega$  contact resistance that we will be measuring. The purpose of adding dc and ac signals is that the physical properties of the system will be set by the dc component (the bias) while the ac modulation allows a sensitive measurement and only weakly perturbs the system.

A dc measurement of the conductance as a function of the voltage on the piezo element in a breaking procedure is presented in Figure (1.7). The abrupt steps in the conductance are due to decrease in the wire diameter atom by atom. Important to notice in Figure (1.7) is that the last step is much longer than the other steps, while the conductance stays nearly constant at  $1G_0$ . This has been

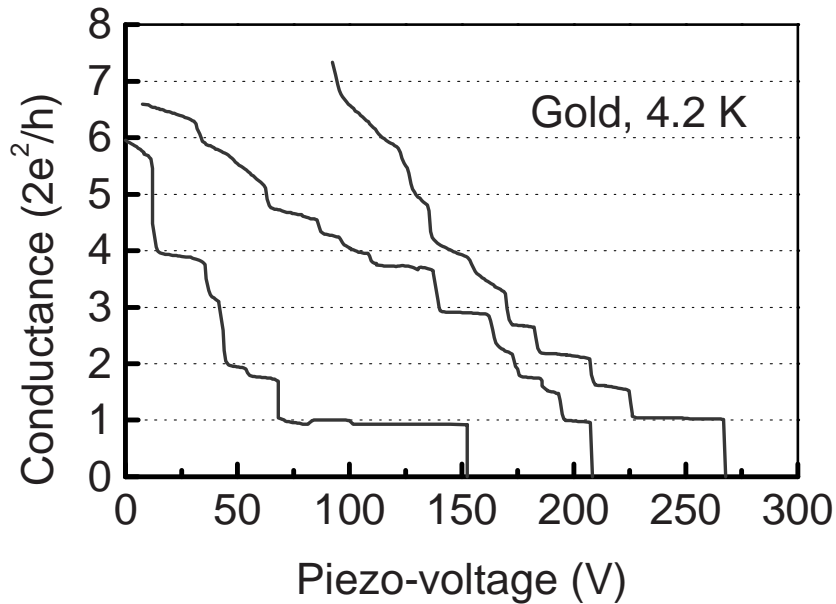


Figure 1.7: *Examples of the conductance as a function of the voltage on the piezo element for a Au contact at 4.2K. At the last stage of breaking one can clearly observe the plateau with at the conductance of one conductance unit.*

interpreted by Yanson *et al.* as the evidence of chain formation (5).

### 1.3.2 Conductance histograms

Using the MCBJ technique is possible to make and break contacts in a very controlled way. Once the contact is broken, it is enough to retract the piezo element and the elasticity of the bending beam which holds the wire will bring the two sides into contact again. Repeated the breaking process will result in a similar conductance trace, which means that just by bringing the two sides together a point contact is reestablished. Individual curves in dc voltage biased measurements, like the ones shown in Figure (1.7), are recorded without control of the local arrangement of the contact, so all traces are usually different, but with some pronounced common features. To obtain the common characteristics of all possible contact geometries, we collect the data in conductance histograms. A conductance histogram is constructed by counting how many times a certain value of conductance appears while repeatedly breaking and making the contact, so the most frequently occurring conductance values will appear as peaks in the histogram <sup>3</sup>. The range of conductance that we are interested in is divided into

<sup>3</sup>Histograms can be obtained from the conductance traces produced by breaking the wire, or while returning into contact. In this thesis, only histograms obtained from breaking traces are used.

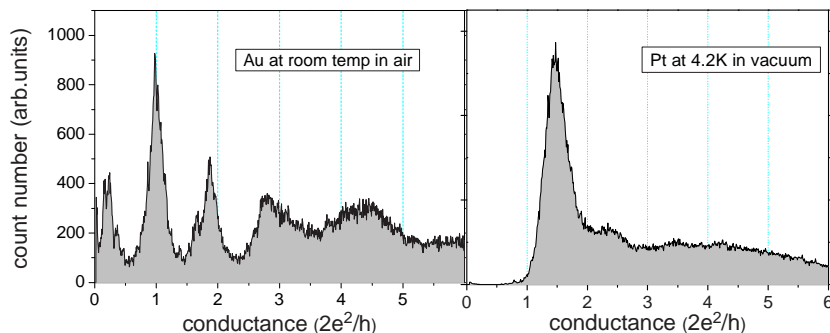


Figure 1.8: *Left: A conductance histogram for Au in room environment. Right: A conductance histogram for Pt, measured at 4.2K. The full conductance range which we are interested in ( $0 - 6G_0$  in this particular case) is divided into a certain number of bins (usually  $\sim 10000$ ) and the number of times that a certain conductance value appears within each bin is represented on the y axis. The most frequent conductance values will appear as the peaks in the histogram.*

a certain number of bins, typically a few thousand, and in each the occurrence of the conductance value is counted. Usually, a conductance histogram is constructed from about a few thousand breaking procedures. Typical histograms obtained in MCBJ experiments for Au under ambient conditions and for Pt at 4.2K are presented in Figure (1.8). Analyzing the histogram for Au we can see clear peaks near  $1G_0$ ,  $2G_0$  and  $3G_0$ . The value of  $1G_0$  corresponds to a single atom contact or a chain of atoms and if we analyze the decomposition of the channels for a single atom contact in terms of independent transmission channels using shot noise, what is discussed in detail in PhD thesis of Helko v.d. Brom (7), we see that only one conductance channel is contributing to transport. So, speaking of Au, a single atom contact has conductance of  $1G_0$  carried by one conductance channel. The conductance of  $1G_0$  for a single atom contact is a common feature of all alkali and  $s$  metals where the conductance of  $1G_0$  is carried by one completely transparent channel. In the case of  $s - p$  metals there are three conductance channels contributing with different transmissions per channel, and five in case of  $s - d$  metals. The Pt data presented in Figure (1.8) shows an example for an  $s - d$  metal. A rather broad peak can be seen around  $1.7G_0$  and it accounts for a chain of atoms, a shoulder around  $2G_0$  accounts for a single atom contacts, while at the higher conductances we find no pronounced features. A detailed analysis of the peaks in the higher conductance regime in the case of alkali and  $s$  metals can be found in references (8; 9) and the PhD thesis of Alex Yanson (3).

The main role of conductance histograms in the experiments presented in this thesis is to provide a reliable and simple tool to make quick qualitative distinction between clean point contacts of metals and the situations when a certain molecule is trapped in the junction. In addition, the peaks in histograms

indicate the preferred conductance values which reflect a stable metal-molecule complexes and which we can investigate in detail by point contact spectroscopy and noise measurements. This topic will be discussed separately for the different molecules covered in this thesis.

### 1.3.3 Length histograms

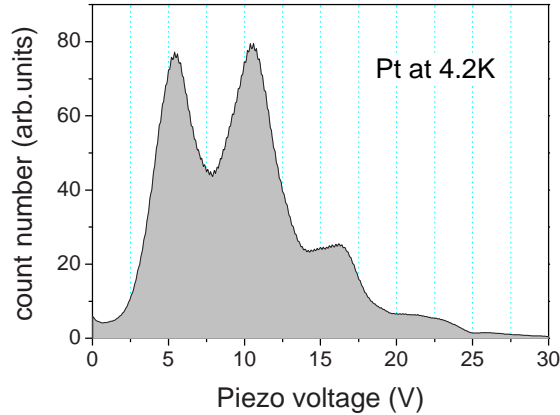


Figure 1.9: A length histogram for Pt chains measured at 4.2K. Along the horizontal axis is plotted the interatomic distance expressed as the piezo voltage. To explicitly correlate the distance and piezo voltage, we use the interatomic distance  $d = 2.3\text{\AA}$ , known from previous experiments (10). Coefficient  $k$  is easily obtained as the ratio  $k = 2.3\text{\AA}/|V_p(n) - V_p(n+1)|$  where the denominator is the piezo voltage difference between any two sequential peaks

As was mentioned before, some metals (Ir, Pt, Au) can form chains of atoms in MCBJ experiments. The total length of such a chain is expected to be approximately a multiple of the size of a single atom of the metal. If we measure the lengths of the plateaus with a conductance of a single atom which are being formed in breaking processes and plot them in the form of a histogram where the horizontal axis is the length and the vertical one is the number of occurrences of a certain length, we get a length histogram. The main difficulty in such experiment is to calibrate the actual length of a chain, measured in  $\text{\AA}$ . The chain is formed while pulling two sides of the wire apart by bending the beam on which the wire is mounted. This is done by increasing the voltage on the piezo element, as shown in Fig.1.5. In such a way one easily obtains a length histogram with the piezo voltage plotted along the horizontal axis, like presented in Figure (1.9). The length of the chain is given by the separation  $d$  between the tips on two sides, which is proportional to piezo voltage  $V_p$ , so  $d = kV_p$  and finding the coefficient  $k$  is the difficult part. The starting point is defined by the point at which the conductance first drops to the value for a single-atom contact. The calibration for  $k$  also differs from sample to sample. There are

two ways of finding that calibration. The first one was proposed by C.Muller (11) and is based on the exponential dependence of the tunnelling current as a function of the distance between the electrodes. This approach is not very precise because it explicitly depends on the work function of two electrodes, which is shape dependent and the shape is not known and differs a lot between the measurements. The other approach is rather sophisticated and based on oscillations of tunnelling resistance at biases above the work function, also called Gundlach oscillations (12; 13).

In measurements presented in this thesis, the length histograms were calibrated in a slightly different way. The interatomic distances in the chains of the different metals are already known from previous experiments (3). For Pt the distance between the peaks in the length histogram is  $2.3 \pm 0.2 \text{ \AA}$  (14). So we used the length histograms as a very simple and quick way to find  $k$  as the ratio  $k = 2.3 \text{ \AA} / |V_p(n) - V_p(n+1)|$  where the denominator is the piezo voltage difference between any two sequential peaks.

### 1.3.4 Point Contact Spectroscopy and Inelastic Electron Tunnelling Spectroscopy

There are two different limits of the mechanisms giving rise to a signal of the electron-phonon interaction in the differential conductance. Here we briefly discuss these limits and the detailed experimental results and analysis for different systems will be presented in later chapters. Figure (1.10(a)) represents Inelastic Electron Tunnelling Spectroscopy (IETS). Two electrodes are separated by a tunnelling barrier and the overlap of the electronic orbitals is small, which makes the typical resistance of this junction large ( $\gtrsim 10^6 \Omega$ ), so the tunnelling current is very small. While in the case of metallic tunnel junctions a weak overlap of the electronic orbitals can be obtained by keeping them separated by a certain distance, in the case of metal-molecule-metal junctions, a weak overlap can be obtained due to weak coupling between the molecular orbitals and the electron orbitals from the metal electrodes to which the molecule is attached or any other weak coupling between the molecular orbitals responsible for conductance.

As is depicted in the Figure (1.10 (a)), electrons from the right lead, that is biased by a voltage  $V$  higher than the left, can tunnel through the barrier, so through the so-called tunnelling channel. But when a molecule is present in the barrier, as soon as  $eV \geq \hbar\omega$ , where  $\hbar\omega$  is the energy of a vibrational excitation of the molecule placed in the contact, by exciting that vibration, the electron loses energy and gets to the other side of the contact with  $E = E_F + eV - \hbar\omega$ , as is indicated in Figure (1.10(a)). This can be seen as the opening of another conductance channel, so that the conductance at  $eV = \hbar\omega$  will increase.

Figure (1.10 (b)) presents the model, and (1.11) a typical curve obtained by Point Contact Spectroscopy (PCS). For this mechanism to be applicable, the probability for reflection of electrons due to imperfect transmission of the contact should be small, so the conductance has to be carried by highly transparent channels. In practice, we will only consider one conductance channel with

transmission  $\tau = 1$  or very close to this. At low temperatures all electron states are occupied up to the Fermi level and if no bias is applied we have coherent electron states occupied up to wave numbers  $+k_z$  and  $-k_z$  where  $z$  is pointing along the axis of the contact, so no net current flows through the contact. If a bias  $V$  is applied, the situation becomes as shown in Figure (1.10(b)). Now, if the molecule bridging the electrodes has vibration mode with  $\hbar\omega \leq eV$ , some of the electrons will excite the vibration and lose a quantum of energy. From an initial state with  $E = E_F + eV$  and  $+k_z$ , the electron would fall into the state with  $E = E_F + eV - \hbar\omega$ . The only available state with  $E = E_F + eV - \hbar\omega$  is one with  $-k_z(E)$ , so opposite to the initial direction. This scattering process is shown in Figure (1.10(b)). As a result a fraction of the electrons is scattered back, (typically  $\sim 1\%$ ) which can be observed as a small decrease in the  $dI/dV$  curve. The electron-vibration coupling differs for different molecules and for the

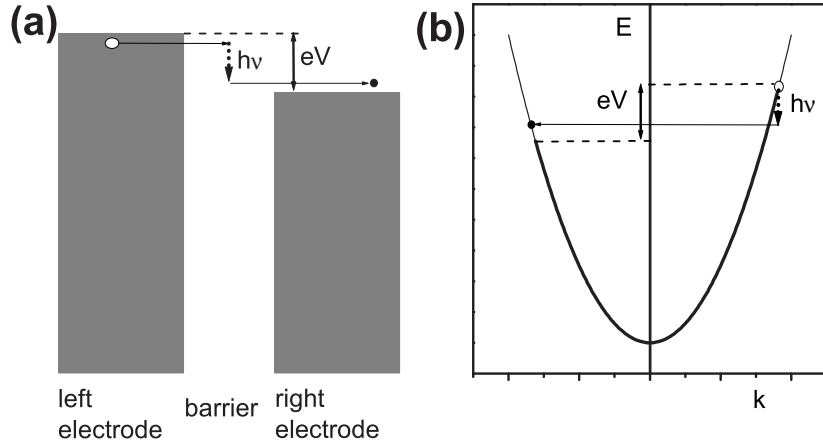


Figure 1.10: Model a) presents the basic principle of Inelastic Electron Tunneling Spectroscopy (IETS). Electrons on the left electrode are  $eV$  higher in energy than those on the right. Two electrodes are separated by the tunnelling barrier and a small tunnelling current flows through the tunnelling channel. The tunnelling barrier can also be a weakly bound or low conducting molecule. In this case, when a tunnelling electron excites a vibration mode of molecule, it scatters into a new state with  $E = E_F + eV - \hbar\omega$ , which opens a new conducting channel, so the current through the contact increases. Figure b) presents the model of Point Contact Spectroscopy (PCS). For simplicity, the contact is assumed to have a single conductance channel with transmission probability  $\tau = 1$ , so there is no back scattering. By increasing the bias, electrons will reach the level  $eV = \hbar\omega$  and by exciting the vibration mode with energy  $\hbar\omega$  of the atomic or molecular junction, they will lose energy. From an initial state with  $E = E_F + eV$  and wave number  $+k_z$ , the electron would fall into a state with  $E = E_F + eV - \hbar\omega$ . The only available state with  $E = E_F + eV - \hbar\omega$  is one with  $-k_z$ . The whole process can be observed as a decrease in differential conductance.

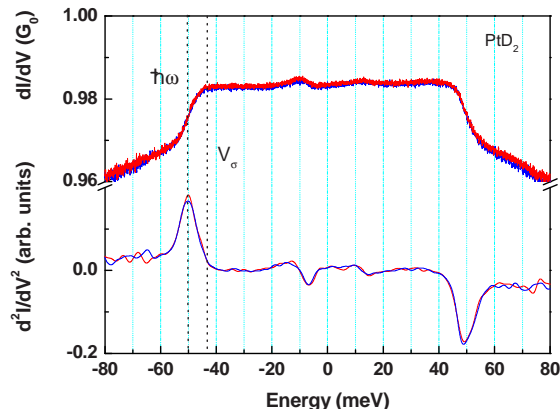


Figure 1.11: *Differential conductance as a function of the bias voltage for a junction of Pt electrodes connected by a single D<sub>2</sub> molecule (see chapter 2). At the energy  $E = \hbar\omega$  a vibration mode is excited and the conductance drops due to the electron-phonon scattering. The lower curve is the numerical derivative of the upper curve and the peaks indicate the vibration excitation energies. The line marked with  $V_\sigma$  roughly indicates the energy on which the electron-phonon scattering starts to occur.*

different modes of vibration of the same molecule. PCS is a very powerful tool for investigation of simple molecule junctions with high transmission. The only, but very serious, weakness of PCS is the requirement  $\tau = 1$  which is very often not fulfilled, especially for more complex molecules. There are two reasons for the requirement on the transmission coefficient in PCS to be  $\tau \simeq 1$ . First is that for  $\tau < 1$  conductance fluctuations become dominant (see below) and the second is that the amplitude of electron-phonon signal is expected to decrease for  $\tau < 1$  and disappear at  $\tau = 1/2$ . In fact, the sign of the signal is expected to change from PCS like at  $\tau = 1$  to IETS-like below  $\tau = 1/2$  (15)(16). Figure 1.12 illustrates this change of sign for a system Pt-H<sub>2</sub>-Pt where a vibration mode was observed both for high transmission ( $\tau \approx 1$ ) and for low  $\tau \approx 0.2$ .

## 1.4 Conductance fluctuations

The origin of the conductance fluctuations can be understood as follows (17; 18; 19). Let us assume that we have a junction with only one transmission channel with transmission  $\tau = t^*t$  ( $t$  is the probability amplitude). One of the possibilities for partial wave reflection is presented in Figure (1.13). As is shown in Figure (1.13), the electron has a probability amplitude  $t$  to be transmitted through the contact. That transmitted part of wave function has a certain probability amplitude  $a$  to be reflected back due to defects in the lattice or impurities and again can be reflected back on the contact. This reflected wave can be reflected again by the contact with probability amplitude  $r$ . So at the end, there is a

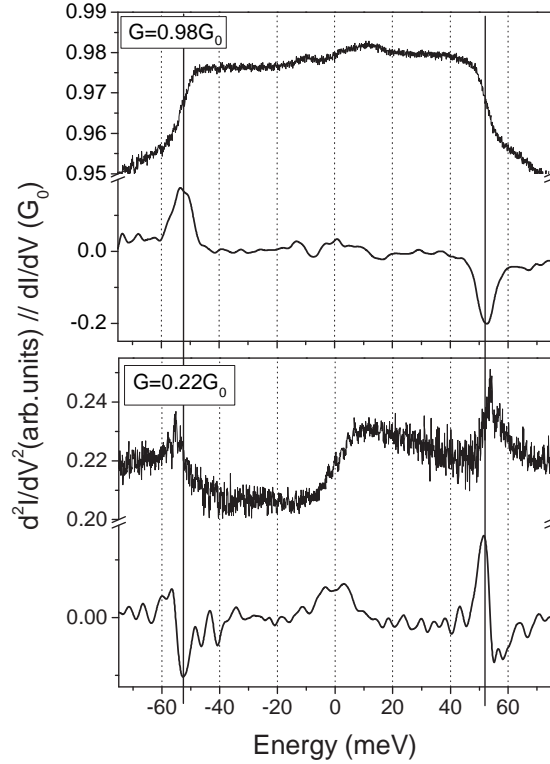


Figure 1.12: *Differential conductance as a function of the energy for PtH<sub>2</sub> contacts with conductance close to  $1G_0$  (upper panel) and the low conductance (lower panel). At the energy  $E = \hbar\omega = 52\text{meV}$  a vibration mode is excited and the conductance drops due to the electron-phonon scattering. The lower curve is the numerical derivative of the upper curve and the peaks indicate the vibration excitation energies.*

probability amplitude  $t$  for the upper path, and a probability amplitude  $tar$  for the lower one. As long as the total length of either path is still shorter than the average coherence length of the electrons they form a superposition. This superposition will be voltage dependent since it depends on the phase difference between the two partial waves. The additional phase accumulated by the lower path is  $k_z L$  where  $L$  is the total length difference between the two trajectories, and  $k_z$  is the momentum, which is energy dependent, therefore voltage dependent as well. The outcome is a  $dI/dV$  curve with large voltage dependent fluctuations among which small effects due to electron-phonon scattering may not be recognizable. The restrictions on transmission probabilities for PCS now become clear: if  $t \simeq 1$ , then  $r = 1 - t \simeq 0$ , so the lower partially reflected wave probability amplitude becomes negligible and the conductance fluctuations are suppressed.

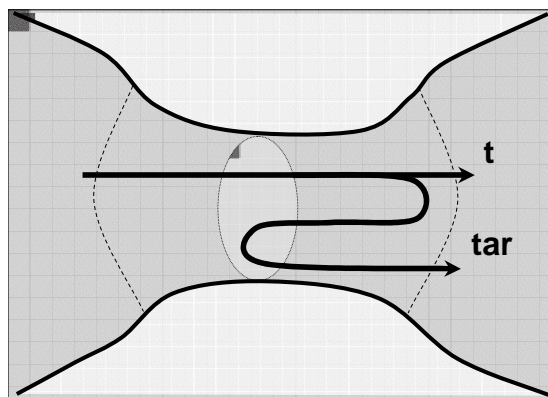


Figure 1.13: *Two possible paths for electron propagation that give rise to conductance fluctuations. If the contact is partially transmitting, electrons will pass through the contact with the probability amplitude  $t$ . There is a small probability that the wave gets reflected back on defects close to the contact, resulting in a probability amplitude for electrons to return to the contact where they can be scattered back again. The path with the probability amplitude  $tar$  represents the sum over all possible scattering paths within the electron coherence length. The interference between two indicated partial waves produces the conductance fluctuations. There is a similar contribution from the waves scattering at the left of the contact.*

## 1.5 One Level Model

The analytical model presented here and used to analyze certain experimentally observed transport properties of single molecules throughout this thesis is developed by M. Paulsson, T. Frederiksen and M. Brandbyge and presented in the reference (16). The transport through molecular systems is usually analyzed by solving complicated and computationally very demanding problems which do not yield simple formulas that can be used for a simple analyzes of experimentally obtained data. Systems such as the molecular bridges with strong coupling to the leads and high conductance, as is the case with  $H_2$  and  $CO$ , introduce some simplifications to the computational problem which reduce the complexity of the problem by several orders of magnitude, yielding very simple, intuitively understandable formulas, easy to use. The above mentioned model is valid for systems where the following conditions are met: (i) the electron-vibration coupling is weak, so the probability for multivibration excitation is small (ii) the density of states (DOS) of the molecule and the leads is slowly changing and does not change significantly from the value at the Fermi level ( $E_F$ ) over a range much larger than the vibration excitation energy. As pointed out in (16), this will be the case if (i) the time which electron spends in the device is much shorter than the electron-vibration scattering time and (ii) the closest resonant level ( $E_{res}$ ) is far away from  $E_F$  comparing to all energies involved ( $(E_{res}-E_F) \gg \Gamma, eV, \hbar\omega$ )

or the broadening by the contacts is so large that ( $\Gamma \gg (E_{res} - E_F)$ , eV,  $\hbar\omega$ ). The model starts from a self-consistent Born approximation, which is then expanded to lowest order ( $2^{nd}$ ) in the electron-phonon coupling. The smooth density of states allows one to perform the integration over energy analytically.

In our molecular bridges the above mentioned conditions are met. The simplest form of the expression is obtained for a single vibration mode of the molecule (One Level Model, OLM). Without going into the details of derivations presented in the reference (16), we write down the set of formulas for the rate equation for the bias dependent number of vibration quanta, the power dissipated in the vibration system and the current through the molecular bridge:

$$\dot{n} = \frac{P}{\hbar\omega} + \gamma_d(n_B(\hbar\omega) - n). \quad (1.17)$$

$$P = \gamma_{eh}\hbar\omega(n_B(\hbar\omega) - n) + \frac{\gamma_{eh}}{4} \frac{(\cosh(\frac{eV}{kT}) - 1) \coth(\frac{\hbar\omega}{2kT})\hbar\omega - eV \sinh(\frac{eV}{kT})}{\cosh(\frac{\hbar\omega}{kT}) - \cosh(\frac{eV}{kT})}. \quad (1.18)$$

$$I = \frac{e^2}{\pi\hbar}\tau V + \frac{e\gamma_{eh}}{\hbar\omega} \frac{1 - 2\tau}{4} (2eVn + \frac{\hbar\omega - eV}{e^{\frac{\hbar\omega - eV}{kT}} - 1} - \frac{\hbar\omega + eV}{e^{\frac{\hbar\omega + eV}{kT}} - 1}) \quad (1.19)$$

In the equations,  $n_B$  is Bose-Einstein distribution,  $\gamma_{eh}$  is electron-hole damping rate (the electron-phonon coupling strength) and  $\gamma_d$  is external damping rate (the phonon-phonon relaxing strength). In the case of transport through the systems such as a hydrogen molecule in between Pt electrodes the mass difference between the molecule and the atoms in the leads is so big that the coupling between hydrogen vibrations and platinum phonons is essentially zero. Therefore, the external damping rate  $\gamma_d$  is close to zero meaning that vibrations can relax only through electrons. From the first formula, which is the rate equation for the number of phonons, and the second which is the expression for the power dissipated in the vibration system, we obtain the number of the vibration quanta as a function of the applied bias which is then used in the expression for the current. Equation (1.19) is the expression for the current through the one level system with the electron-vibration interaction taken into the account. A perfect example of a such system is a molecule in metal contact with only one molecular orbital at the Fermi level. It is interesting to notice that, in the case of a system with  $\tau > 0.5$ , the conductance would decrease due to the electron-vibration interaction, while in if  $\tau < 0.5$ , the conductance would increase. In Fig.1.14 the authors of Ref.(16) demonstrate the fitting power of the model on a differential conductance curve for a Pt-D<sub>2</sub>-Pt bridge. The essential fitting parameter here is the electron-hole damping rate  $\gamma_{eh}$ , which determines both the height of the phonon step and the slope of the curve after the step. The different fitting curves are for the different values of the external damping factor  $\gamma_d$ . From the obtained curves it is clear that the external damping is negligible compared to relaxation of the vibration excitation by electron-hole excitations.

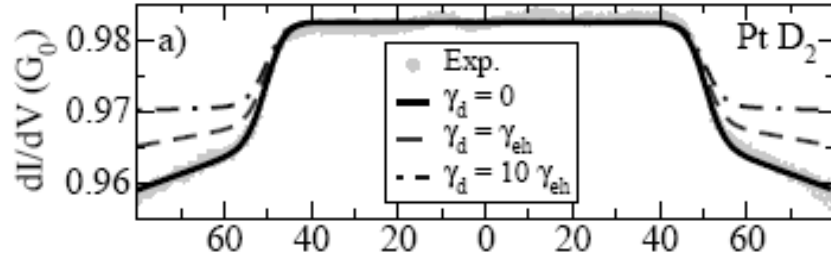


Figure 1.14: *Differential conductance as a function of the bias for a Pt-D<sub>2</sub>-Pt junction as discussed in chapter 2. The light gray curve presents the experimental data, while the rest are the fits obtained by OLM for different  $\gamma_d$ . The parameters used for the fit are  $\hbar\omega=50\text{meV}$ ,  $\tau = 0.9825$ ,  $\gamma_{eh} = 1.1 \cdot 10^{12}\text{s}^{-1}$  and  $T=17\text{K}$ . After the ref (16).*

The presented model will be used throughout this thesis as a fit to experimental measurements to extract the parameters as the vibration frequency, coupling strength which is equivalent to damping rate  $\gamma_{eh}$ , and the apparent temperature broadening.

## Chapter 2

# Characterization of Pt-H<sub>2</sub>-Pt molecular junctions by point contact spectroscopy

This work is performed in collaboration with K.Thygesen, K.Jacobsen, M. Paulsson, R.Smit and C. Untiedt. Published as Phys Rev B **71**, 161402(R)(2005)

### 2.1 Introduction

The experiments on D<sub>2</sub>, H<sub>2</sub>, HD, CO, C<sub>6</sub>H<sub>6</sub> and C<sub>2</sub>H<sub>2</sub> molecular junctions form the core of this thesis and a natural continuation of work started by Roel Smit, Yves Noat and Carlos Untiedt (20; 21). The above mentioned order of molecules is perhaps the best way to represent the order of the value that each molecule through the different experiments added to this thesis. As a small guide through this chapter it is worth mentioning which was the main goal of our measurements and to what extent and in which way different molecules contributed to that goal. The idea of using molecules as the functional units in electronic circuits exists since 1974 (22) and it triggered many ideas and experiments (23; 24; 25; 26; 27; 28; 29; 30; 31). It resulted in a new field of research named "Molecular Electronics". But if one walks into our "Molecular Electronics Shop" one will find the shelves loaded with fancy components with quite uncertain performances and quite often very far from theoretically predicted behaviors. Our approach was to try to understand the behavior of the simplest molecules (not even qualified to be placed at the above mentioned shelves) and try to understand the measurements in detail, hoping that it will build a more solid base to proceed towards the more complex systems. What we developed in the end is a simple system that helps developing new measurement techniques,

DFT calculation models and scientific intuition.

In the present chapter, the construction of that simple system is presented.  $D_2$ ,  $H_2$  and HD form an ideal set of molecules to start with, since they have identical and very simple electronic configurations but large mass differences so that one can observe clear vibration frequency shifts. The mass difference is, as it will become clear later, very important for the analysis of vibration properties, which can be used as a signature of the molecule in the junction. In point contact spectroscopy (PCS) we identify the vibration frequencies of  $D_2$ ,  $H_2$  and HD. We also obtain the dependence of those vibration modes as a function of the molecule-metal bond stretching. The frequencies of corresponding vibration modes for different isotopes scales as the square root of the mass ratio, as expected for harmonic oscillators. Shot noise measurements analyzing the number of conducting channels involved in transport through the Pt- $D_2$ -Pt bridge are presented in a separate chapter. A new technique for observing vibrational excitations based on vibrationally assisted two level fluctuations is presented in Chapter 7 and used for analyzing anomalous spectra that were previously unexplained, as well as for analyzing the vibrations of  $H_2$  incorporated in Pt chains and the vibration modes of  $C_6H_6$ . Testing and implementing the new measurement technique would not have been possible without having spent enough effort in understanding the Pt- $D_2$ -Pt bridge.

The set of measurements on  $D_2$ ,  $H_2$  and HD forms a complete and well understood unit from experimental but also theoretical point of view. The need for simple test models for theory becomes clear if one considers the calculations obtained by the different groups (32; 33; 34; 35; 16), all dealing with the conductance properties of a Pt- $H_2$ -Pt bridge. Some of them are in very good agreement with our measurements (34; 16), but others disagree on essential points. We shall briefly discuss the differences between these calculations.

## 2.2 Experiments with $D_2$ , $H_2$ and HD

### Conductance histograms for Pt and Pt+ $D_2$

Although historically the experiments started with hydrogen, the presentation of the experimental results here will start with those for deuterium, since they provide the most complete set. As mentioned before, all measurements on molecules presented in this thesis are performed at 4.2K under cryogenic vacuum conditions. Before the measurements, the sample chamber containing a clean Pt wire MCBJ device is evacuated to about  $10^{-6}$ mBar at room temperature and lowered into a liquid helium dewar. The chamber is fitted with active charcoal for cryogenic pumping, so that the pressure in the sample chamber during the measurement is estimated to be below  $10^{-12}$ mBar. Once cold, the Pt wire is broken at the pre-cut notch by mechanical bending of the substrate to which it is fixed. First, we collect a clean Pt conductance histogram in order to verify that the surface is not contaminated by some eventual residual gas condensed on the contact. A clean histogram has a peak near the typical

conductance of a single Pt atom,  $\simeq 1.5G_0$ , and a low count below  $1G_0$  as shown in Fig.(2.1 *left*). Next, we inject a small amount of molecular  $D_2$  gas and observe the conductance histogram changing from the clean Pt characteristics, with a pronounced conductance peak near  $1.5G_0$ , into one typical for a Pt- $D_2$ -Pt bridge, having strong weight at low conductance values and a peak near  $1G_0$  as shown in Fig.(2.1 (*right*)). Both measurements are obtained at a dc bias voltage of 100mV. Once  $D_2$  gas was added to the chamber, the clean Pt conductance histogram can not be recovered unless a large bias ( $\sim 300$ mV) is applied. This means that it is very likely that all surfaces are covered with  $D_2$  and a large applied bias during the breaking and making process can heat up the contact area such that  $D_2$  molecules get repelled. However, as soon as the bias is lowered,  $D_2$  is seen to come back in the contact again.

From the measurements presented above we can draw the following conclusions. The presence of  $D_2$  in the sample chamber certainly changes the conductance of the point contacts, so we can conclude that the molecules do something to the contact. If one looks at the conductance traces presented as the insets in Fig.(2.1), even in the presence of  $D_2$  gas they show a step like behavior and the plateau near  $1G_0$  results in a sharp peak in the conductance histogram at  $1G_0$ . If the contact configuration responsible for the peak at  $1G_0$  is due to a  $D_2$  molecule bridging the gap between two Pt electrodes, one should be able to excite the vibrations and, according to the model for point contact spectroscopy, observe a small decrease in the conductance due to electron back scattering. Indeed, it turns out to be possible to obtain a fairly flat  $dI/dV$  vs. voltage curve, with symmetric steps downward due to electron-phonon interaction and the results are presented in the following sections.

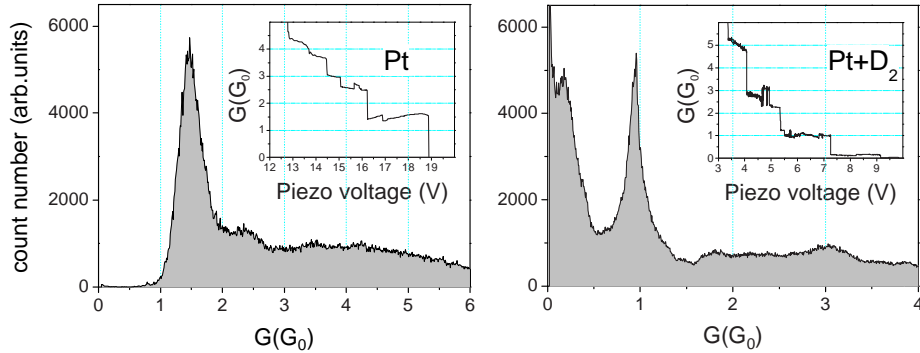


Figure 2.1: *Left: Conductance histogram for a clean Pt contact at 4.2K. The peak close to  $1.5G_0$  corresponds to a chain of atoms while the shoulder close to  $2G_0$  corresponds to a single atom contact. Right: Conductance histogram for a Pt contact after molecular  $D_2$  was added in the sample chamber. Both measurements are taken at a dc bias of 100mV and the insets show examples of breaking traces from which the conductance histogram is built.*

### 2.2.1 PCS measurements on a Pt-D<sub>2</sub>-Pt bridge

As explained in Chapter 1, a molecular contact with conductance close to  $1G_0$  is a system on which Point Contact Spectroscopy (PCS) can be used to analyze the vibration properties of the junction. If the conductance of  $1G_0$  is mostly due to one conductance channel, electrons are shooting through the contact without any backscattering, unless the bias is large enough, so that they have enough energy to excite the vibrations of the bridging structure. That would cause a small decrease in conductance, as was already explained. Sweeping the dc bias from -100mV to +100mV while recording the first harmonic of the lock-in signal gives the differential conductance ( $dI/dV$ ) as a function of the bias. Figure (2.2) presents a selection of  $dI/dV$  curves obtained in different experiments on Pt-D<sub>2</sub>-Pt bridges. To record a single curve typically takes about 20 seconds to 1 minute, depending on the chosen number of sample points in the measurement range. To select a configuration on which it is possible to obtain nice PCS measurement is very tricky and the success rate is based on experience. Usually, the sample is biased with 100mV and dc conductance is monitored on the oscilloscope while the contact is being broken and made manually, searching for a stable configuration with conductance of  $1G_0$  and low noise over a certain stretching distance (roughly 0.1Å). Only a small fraction of all selected contacts give nice  $dI/dV$  curves. Our experimental range is limited to 100mV since on higher biases the contact becomes unstable and breaks. Such a situation is shown in Fig. (2.2 (b)) where the bias voltage has been swept from -150mV to +150mV. In the range above 100mV the curve is, due to the heating, very noisy. On all curves presented in Fig.(2.2) one can see the steps downwards in the conductance, produced by the electron-vibration interaction and the peaks in the second derivative indicate the centers of the vibration frequencies. Judging from these curves, the excitations are spread between 30meV and 100meV. Multiple steps in one curve could mean either that they belong to different modes, or that they are due to a multiple vibrations excitations of the same mode. In Fig.(2.2 (a)) a curve is shown with one excitation close to 38meV and a second one close to 75meV. Since the second frequency is nearly double the value of the first one, one could expect that the second excitation is due to a process where a single electron excites two phonons with  $\hbar\omega \approx 38\text{meV}$ . But since the step height is correlated with the number of the electrons which excite vibrations, from the curve one should conclude that two-phonon processes are more frequent than the single ones, which is unlikely to be the case. Later we will show by measuring the dependance of the frequencies upon the stretching that we are dealing with two different modes. The excitation frequencies can be seen as peaks in the  $d^2I/dV^2$  curves obtained from the fitted curves, but to determine the width of the transition steps and the electron-phonon coupling constant, we use the One Level Model (OLM) presented in Chapter 1. The fitting parameters for the  $dI/dV$  curve in Fig.(2.2(a)) obtained from the OLM

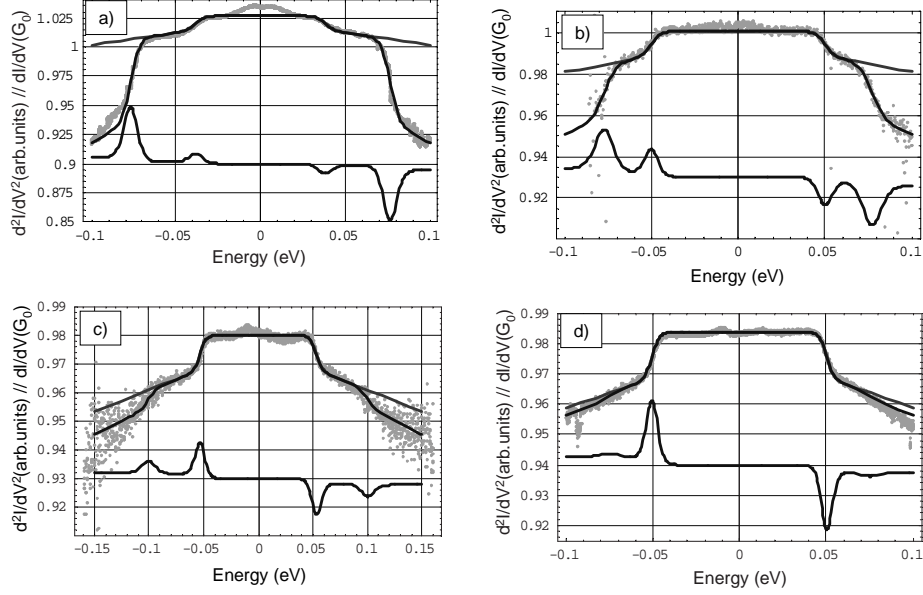


Figure 2.2: *Differential conductance measurements obtained on the plateau close to  $1G_0$  for different Pt-D<sub>2</sub>-Pt bridges, like the one presented in the inset in Fig.2.1 right. Fits through the data are obtained using the One Level Model explained earlier. Lower curves are derivatives of the upper fits and the peaks identify the frequencies of the excitation. All presented curves have two modes excited, which can be seen from two peaks in the second derivative. The uppermost curves are fits where only one vibration frequency is assumed. The fitting parameters are optimized for the positive bias side.*

are:

$$\begin{aligned} & \{ \hbar\omega_1 = 38\text{meV}; T_1 = 20\text{K}; \gamma_{e-h,1} = 0.55 \cdot 10^{12}\text{s}^{-1} \}, \\ & \{ \hbar\omega_2 = 76.5\text{meV}; T_2 = 20\text{K}; \gamma_{e-h,2} = 6.5 \cdot 10^{12}\text{s}^{-1} \}. \end{aligned} \quad (2.1)$$

From the parameters obtained we see that the mode with  $\hbar\omega_1=38\text{meV}$  couples more than ten times weaker than the mode with  $\hbar\omega_2 = 76.5\text{meV}$ . The width of the transition step is assumed to be determined by thermal broadening and in that case the temperature should be around 20K which is much more than the bath temperature of 4.2K. The temperature obtained from the thermal noise measurements at zero bias shows values around 5K, which indicates that the broadening mechanism could be due to some more complicated process, what will be investigated separately in Chapter 6. The shape of the  $dI/dV$  curves is very well reproduced, including the slope following the step. That slope is due to re-absorption of non-equilibrium phonons (in this case molecular vibrations) by conduction electrons.

In Fig.(2.2 (b)) is presented a system with slightly different parameters:

$$\begin{aligned} \{ \hbar\omega_1 = 50\text{meV}; T_1 = 20\text{K}; \gamma_{e-h,1} = 0.75 \cdot 10^{12}\text{s}^{-1} \}, \\ \{ \hbar\omega_2 = 79\text{meV}; T_2 = 20\text{K}; \gamma_{e-h,2} = 2 \cdot 10^{12}\text{s}^{-1} \}. \end{aligned} \quad (2.2)$$

The largest difference is the oscillation at 50meV. Figures (c) and (d) have vibrations close to the ones presented in figure (b) but with obviously different ratios of the step heights for the first and the second oscillation showing that the oscillation appearing as the second one in a curve is not necessarily the one which couples stronger. The curve in figure (c) is one of the few which did not break at a bias as large as 150meV. It shows a rather large noise level at biases above 100meV. The fitting parameters for Fig.(2.2 (c) and (d) are:

$$\begin{aligned} \{ \hbar\omega_1 = 53\text{meV}; T_1 = 22\text{K}; \gamma_{e-h,1} = 0.85 \cdot 10^{12}\text{s}^{-1} \}, \\ \{ \hbar\omega_2 = 100\text{meV}; T_2 = 30\text{K}; \gamma_{e-h,2} = 0.8 \cdot 10^{12}\text{s}^{-1} \}. \end{aligned} \quad (2.3)$$

$$\begin{aligned} \{ \hbar\omega_1 = 50.3\text{meV}; T_1 = 16\text{K}; \gamma_{e-h,1} = 1 \cdot 10^{12}\text{s}^{-1} \}, \\ \{ \hbar\omega_2 = 75\text{meV}; T_2 = 30\text{K}; \gamma_{e-h,2} = 0.2 \cdot 10^{12}\text{s}^{-1} \}. \end{aligned} \quad (2.4)$$

The vibration frequencies obtained from a large number of curves (around 400) from 12 measurement sessions are presented in the form of a histogram in Fig.(2.3) and the origin of multiple peaks will become clear after the next chapter where the measurements obtained on H<sub>2</sub> are presented.

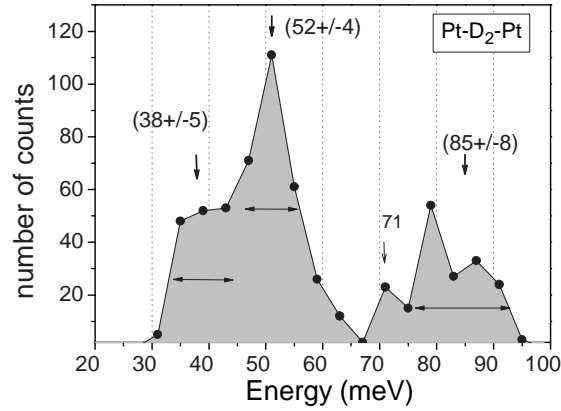


Figure 2.3: Histogram of the vibration frequencies on Pt-D<sub>2</sub>-Pt bridges collected from about 400 individual dI/dV curves obtained in different measurements.

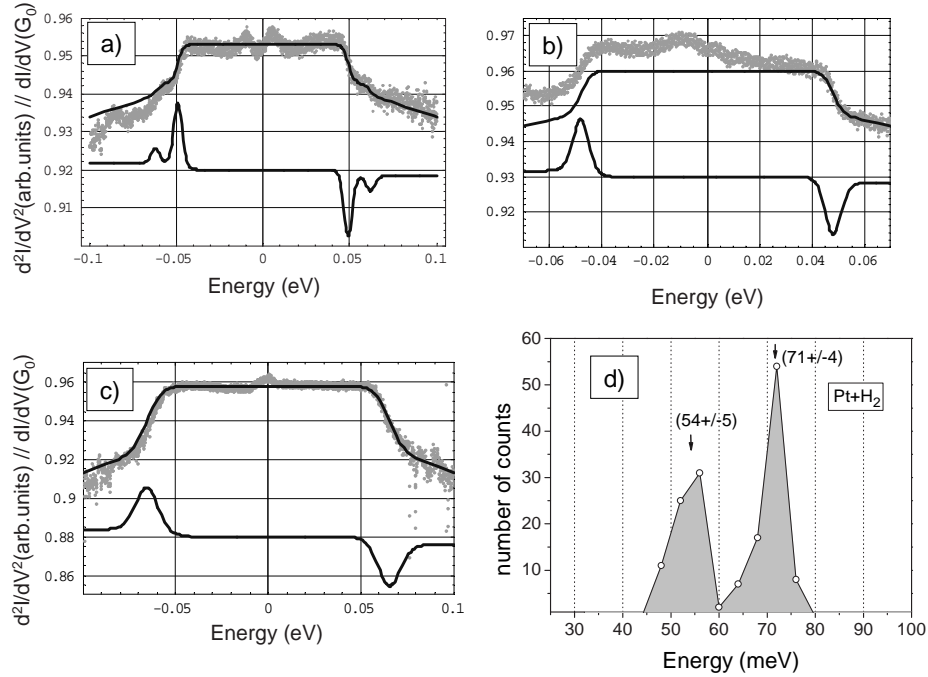


Figure 2.4: Figures a), b) and c): Differential conductance as a function of the applied bias for Pt-H<sub>2</sub>-Pt junctions. Fits through the data are obtained using the OLM optimized for the positive bias side and the derivative of the fitted curves ( $d^2I/dV^2$ ) are shown as the lower curves. The figure a) shows a system with two excitation frequencies, while b) and c) have only one. The figure d) presents the distribution of all measured excitation frequencies for Pt-H<sub>2</sub>-Pt junction.

## 2.2.2 PCS measurements on a Pt-H<sub>2</sub>-Pt bridge

The same procedure as already explained when introducing deuterium gas into the chamber was repeated with hydrogen and the same change in conductance histogram was observed. PCS measurements were performed on junctions with H<sub>2</sub>, using the same procedure as in the case of D<sub>2</sub>. Figure (2.4) shows a selection of typical differential conductance curves of a Pt-H<sub>2</sub>-Pt junction. The measurement data are presented in gray, while the dark curve is the fit obtained by the One Level Model (OLM). The steps in the  $dI/dV$  curves indicate the excitations. While curve a) contains two steps the most commonly observed situation is presented in the curves b) and c) which have only one, close to one of the two values from a double step curve. The peaks in the  $d^2I/dV^2$  curves (lower curves) indicate the center of the oscillation frequencies. Figure d) presents the distribution of all excitation frequencies observed in all measurements, which shows a distribution with two distinct peaks.

The fitting parameters obtained by the OLM for the system presented in

figure a) are:

$$\begin{aligned} &\{\hbar\omega_1 = 49\text{meV}; T_1 = 12\text{K}; \gamma_{e-h,1} = 0.65 \cdot 10^{12}\text{s}^{-1}\}, \\ &\{\hbar\omega_2 = 61.9\text{meV}; T_2 = 12\text{K}; \gamma_{e-h,2} = 0.2 \cdot 10^{12}\text{s}^{-1}\}. \end{aligned} \quad (2.5)$$

The fitting parameters for figures b) and c) respectively are:

$$\{\hbar\omega_1 = 47.9\text{meV}; T_1 = 15\text{K}; \gamma_{e-h,1} = 0.8 \cdot 10^{12}\text{s}^{-1}\}. \quad (2.6)$$

and

$$\{\hbar\omega_2 = 65\text{meV}; T_2 = 30\text{K}; \gamma_{e-h,2} = 2 \cdot 10^{12}\text{s}^{-1}\}. \quad (2.7)$$

As was mentioned earlier, the broadening of the transition step between the conductance level before and after the molecular vibration is excited is in the OLM assigned to the temperature broadening, which is not necessarily the only source of broadening. The problem of the transition width is discussed separately in Chapter 6.

## 2.3 Correlation between the D<sub>2</sub> and H<sub>2</sub> vibration frequencies

This is perhaps a good place to draw some early conclusions, summarizing what we have observed so far. The main attention is focussed on the two distributions of the observed frequencies Fig.(2.3) and Fig.(2.4(d)), which are presented in a different form in Fig.(2.5). In the upper panel is shown the distribution of the frequencies measured on Pt-D<sub>2</sub>-Pt bridges, while the lower one presents the data obtained for H<sub>2</sub>.

Since we suspect that the contact on which the vibration spectra are taken consists of a single molecule (D<sub>2</sub> or H<sub>2</sub>), which is bridging the gap between two atomically sharp Pt electrodes, it is expected that it behaves as a harmonic oscillator. In that case, no matter what the orientation is, the frequencies of the lighter oscillator (H<sub>2</sub>) should be higher by a factor  $\sqrt{2}$  as compared to the corresponding frequencies of the heavier (D<sub>2</sub>), since the frequency is inversely proportional to the square root of the mass ratio

$$\mu = \frac{\omega_{H_2}}{\omega_{D_2}} = \sqrt{\frac{1/m_{H_2}}{1/m_{D_2}}} = \sqrt{\frac{1/2}{1/4}} = \sqrt{2}. \quad (2.8)$$

The hatched distribution curve in the lower panel presents the one for the H<sub>2</sub> frequencies when scaled down by the factor  $\mu$ , providing strong evidence that the PCS measurements are indeed obtained on the molecular junctions. Hydrogen frequencies centered at  $(54 \pm 5)\text{meV}$  and  $(71 \pm 4)\text{meV}$  correspond to deuterium frequencies at  $(38 \pm 5)\text{meV}$  and  $(52 \pm 4)\text{meV}$ . The Deuterium frequency centered around  $85\text{meV}$  does not have a corresponding one in the hydrogen distribution curve because that one would have been centered around  $120\text{meV}$ , which is

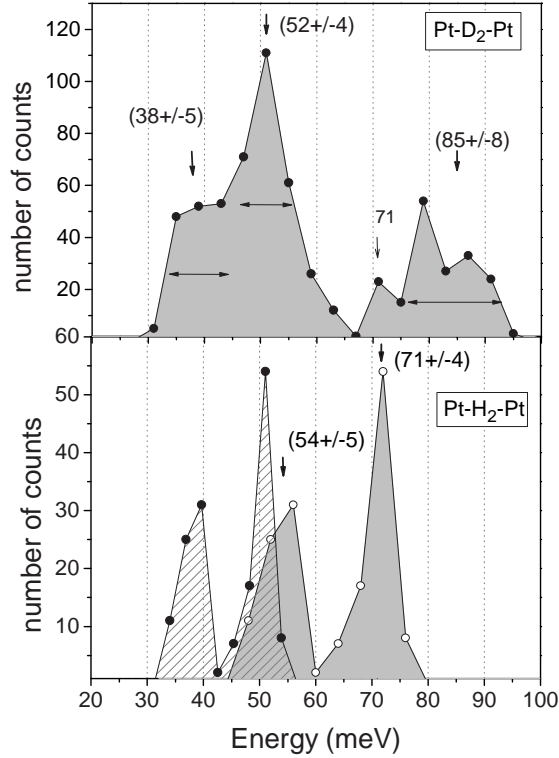


Figure 2.5: Frequency distributions for junctions with  $D_2$  (upper panel) and  $H_2$  (lower panel). The hatched distribution is obtained by scaling down the one of  $H_2$  by the factor  $\sqrt{\frac{1/m_{H_2}}{1/m_{D_2}}} = \sqrt{2}$ .

beyond our experimental range. The isotope shift of the vibration modes makes it possible to observe this mode that is not visible for  $H_2$ .

In the deuterium distribution curve a peak around 71meV is clearly present which we attribute to a small hydrogen contamination. The total weight is less than 1% of the full distribution. This is not unexpected since most of the measurements are performed on a setup where the vacuum conditions are obtained using a turbo pump which is not efficient in pumping hydrogen. The second hydrogen contamination peak, which should be around 54meV is buried in the deuterium data.

The peak around 85meV in the deuterium distribution is rather wide. Based on experience gained by investigating hundreds of  $dI/dV$  curves for the junctions with deuterium, it is most likely that the center of that peak is even higher in energy, since we are limited by the experimental window of about 100meV. Later, when the stretching behavior of the frequencies will be studied, it will become clear why we are actually able to observe this mode.

## 2.4 Conclusions based on the frequency distribution

After this short discussion based only on the distributions of the frequencies of deuterium and hydrogen, it can be concluded that the multiple steps in  $dI/dV$  curves are due to different vibration modes. Since the second peak is often stronger than the first, the possibility that the second peak is due to multiple excitations can be excluded. In the case of deuterium, there is good evidence for three vibration modes in the experimental window of 100meV, while for the case of hydrogen there are only two. There is also a good indication that it is indeed a molecule bridging the gap between Pt electrodes, not an atom of deuterium or hydrogen since in the deuterium case we observed three vibration modes. Hypothetically, in the case of a single atom bridging the contact, there are three vibration modes possible, one longitudinal and two transversal where the latter should be degenerate if the potential landscape in which it oscillates is cylindrically symmetric. It is a delicate question how much asymmetry would be needed to lift the degeneracy of the transversal modes for an atom and whether it would still result in such distinct peaks in the distribution of oscillation frequencies. The question whether we have an atom or a molecule in the junction we determined experimentally by measuring vibration modes of HD.

## 2.5 PCS measurements on a Pt-HD-Pt bridge

HD is a molecule consisting of one H and one D atom. In the case that a molecule would be dissociated on the Pt surface and a single atom would bridge the contact, the oscillation frequencies in the case when HD is injected into the chamber would be either the ones already observed for hydrogen or the ones for deuterium, randomly. If the junction is bridged with one molecule, in the case of HD, the frequencies should be roughly in between the ones observed for deuterium and hydrogen. The scaling with the mass in the case of HD is not as simple as in case of hydrogen since the mass in HD is not symmetrically distributed. Approximately one should expect a scaling  $\omega_{HD}/\omega_{D_2} = \sqrt{4/3}$  and  $\omega_{H_2}/\omega_{HD} = \sqrt{3/2}$ .

Since the aim for now is not to determine the orientation of the molecule in the junction but rather to get clear evidence whether we have a molecule or an atom in the contact, we collect the measured  $dI/dV$  spectra for HD in a histogram and compare it with the histograms obtained for hydrogen and deuterium. In Fig.(2.6), on the left is an example of a differential conductance curve for HD with two excitations present. The fitting parameters for this curve are:

$$\begin{aligned} &\{\hbar\omega_1 = 52meV; T_1 = 12K; \gamma_{e-h,1} = 0.4 \cdot 10^{12}s^{-1}\}, \\ &\{\hbar\omega_2 = 63meV; T_2 = 12K; \gamma_{e-h,2} = 0.2 \cdot 10^{12}s^{-1}\}. \end{aligned} \quad (2.9)$$

In Fig.(2.6) on the right are shown the frequency distributions for  $D_2$ , HD and

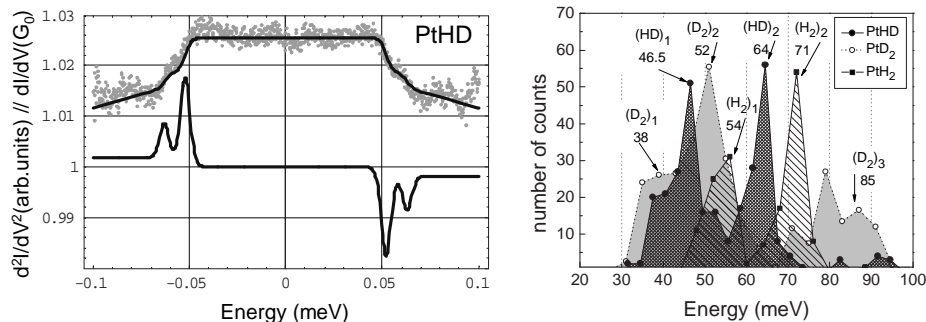


Figure 2.6: *Left: Differential conductance as a function of the energy. In gray are shown the experimental data, the dark curve is the fit obtained by the OLM and the lower curve is the calculated  $d^2I/dV^2$  as a function of the energy where the peaks are indicating the excitation frequencies. Right: Vibration frequencies histograms for  $D_2$  (open circles),  $HD$  (black dots) and  $H_2$  (black squares).*

$H_2$ . The frequency distribution for each molecular junction is obtained by collecting all excitation frequencies obtained in individual measurements on junctions when a certain type of molecule is injected, without any pre-selection based on the position of the excitation frequency. The first peak in the  $HD$  distribution is around 46.5 meV, while the corresponding values for  $D_2$  and  $H_2$  are around 38 meV and 52 meV giving the ratios  $\omega_{HD}/\omega_{D_2} = 1.22$  and  $\omega_{H_2}/\omega_{HD} = 1.16$ . The second peak in the  $HD$  histogram is around 64 meV and the peaks for  $D_2$  and  $H_2$  are around 52 meV and 71 meV which gives the ratios  $\omega_{HD}/\omega_{D_2} = 1.23$  and  $\omega_{H_2}/\omega_{HD} = 1.1$ . These ratios are close to those expected from a straight forward scaling by the masses. So the conclusion is that the observed frequencies for  $HD$  are generally different from the ones for hydrogen and deuterium and are formed in between those, so it is a molecule bridging the gap in between the electrodes and not an atom. The frequency scaling shows the behavior as would be expected in a classical approximation of the  $HD$  molecule acting as a harmonic oscillator. One important detail to notice in Fig.(2.6 (right)) are the additional counts outside the main peaks in the  $D_2$  and  $HD$  histograms. In the case of  $H_2$ , the data points create two peaks and the scatter is rather small with no counts on the higher frequencies where the third mode of deuterium is situated. The histogram for  $D_2$  has some counts on the frequencies which are characteristic for  $H_2$  which is likely due to a small  $H_2$  contamination as already discussed. But in the  $HD$  histogram there is significant number of counts at the frequencies characteristic for both, hydrogen and deuterium. The origin of hydrogen frequencies could partially be the same as explained already, but where does the deuterium come from? It is known from the literature that hydrogen dissociates on flat Pt surfaces at room temperature. That process might be suppressed at low temperatures but it is not known what happens on surfaces with low coordination number. Our observations suggest that  $HD$  is not only being dissociated, but it recombines again since we observe a clear

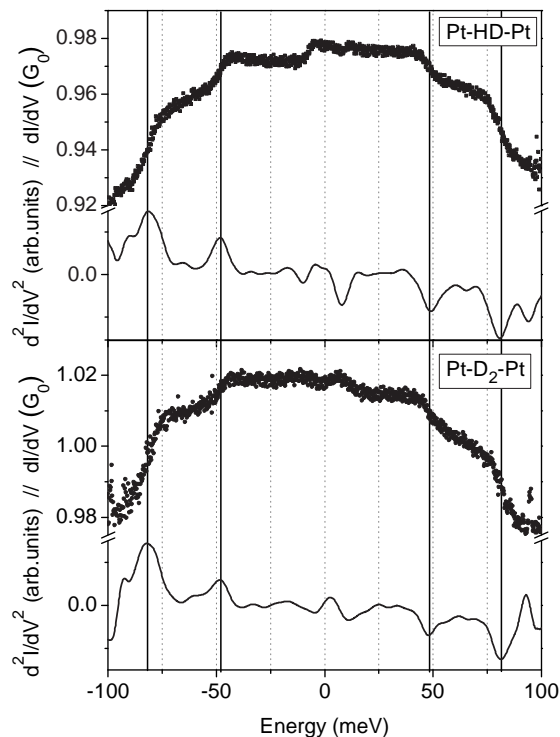


Figure 2.7: both panels:  $dI/dV$  (upper curve) and  $d^2I/dV^2$  (lower curve) as a function of the energy. In the upper panel is shown an atypical measurement obtained when HD was admitted into the sample chamber. In the lower panel is shown a typical  $dI/dV$  curve for  $D_2$  for comparison.

presence of vibrations characteristic for a Pt- $D_2$ -Pt bridge. Fig.(2.7) shows a comparison between an atypical curve obtained in an HD measurement and one typical curve obtained in  $D_2$  measurements. The two are nearly identical, what strongly suggests that  $D_2$  has been somehow created in the junction. Such anomalous HD curves occur in about 5% of the cases. Figure (2.8) shows a sequence of stretched contacts on which the vibration frequencies were measured (by a method discussed later). The contact was not observed to break during the entire sequence, but the series of obtained frequencies changes between the ones characteristic for HD and those for  $D_2$ . This suggests that the molecule in the junction was changing from HD to  $D_2$ . This switching behavior was observed only occasionally, and only for HD. It suggests that either the molecular bridge is dynamically being assembled from atoms present near the junction, or the junction can be formed alternatively by two molecules (one HD and one  $D_2$ ) in close proximity. By mechanical stretching of the contact the preference for one or the other contact arrangement would than be shifted.

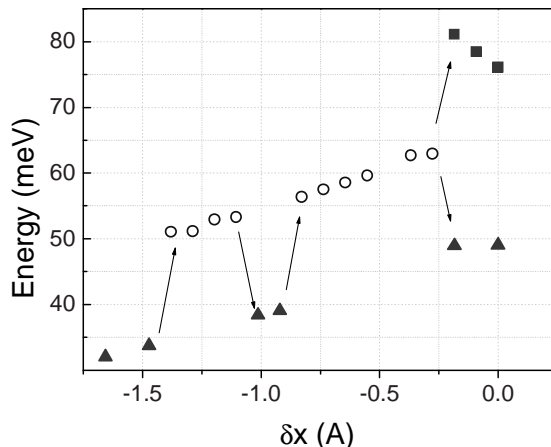


Figure 2.8: Frequency of molecular vibrations as a function of the distance increase between the electrodes for HD admitted to the Pt junction. Open circles correspond to HD frequencies while dark triangles correspond to D<sub>2</sub> frequencies. Eventually the contact was stretched far enough that the third D<sub>2</sub> mode enters in the experimental range.

## 2.6 Comparison with DFT model calculations - transmission

In the last few sections, the experimental data were presented and some conclusions were made on the basis of measurements. The main conclusion is that a single molecule of H<sub>2</sub>, D<sub>2</sub> or HD, under the conditions of cryogenic vacuum, binds to atomically sharp Pt tips formed in MCBJ, creating a suspended molecular bridge with a conductance of 1G<sub>0</sub>. A hydrogen molecule has two electrons which are occupying a 1s orbital, making a closed shell configuration with an energy gap of a 12.6 eV (34) to the next energy level, so it is not obvious how it conducts at all. The analysis of the conduction mechanism in a Pt-H<sub>2</sub>-Pt junction was done by various theoretical groups (33; 20; 32; 34; 36) and a variety of conductance properties was predicted. A comparison between some of the aspects of those theories will be presented in the section devoted to the measurements of shot noise. The model which later turned out to agree the best with our measurements is the one developed by K. S. Thygesen and K. W. Jacobsen presented in Ref.(34; 36). The model for which Thygesen *et al.* performed the calculations consists of three regions: a central region which is the H<sub>2</sub> molecule placed along the axis of symmetry of the contact, attached to the apex atoms of two Pt pyramids made of four atoms each. Such central region is attached to two (left and right) Pt(111) surfaces which represent the contact leads. The conductance is determined by the transmission function at the Fermi level,  $T(\epsilon_F)$  (37) which is obtained using Green's function methods (38; 39). The main transport properties of the contact are summarized in

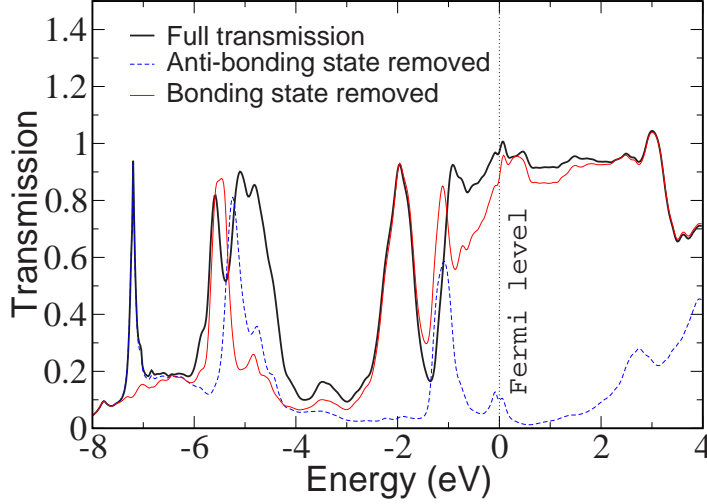


Figure 2.9: *Transmission of the Pt-H<sub>2</sub>-Pt junction as a function of the energy is presented by the black curve. Two dashed curves are the transmissions through the bonding and antibonding states which shows that the transmission around the Fermi energy is through the antibonding state. After ref(34).*

Fig.(2.9). A hydrogen molecule has two  $s$  electrons ( $|1\rangle$  and  $|2\rangle$ ) which form a bonding ( $|b\rangle = \frac{1}{\sqrt{2}}(|1\rangle + |2\rangle)$ ) and antibonding ( $|a\rangle = \frac{1}{\sqrt{2}}(|1\rangle - |2\rangle)$ ) states. Coupled between Pt leads the orbitals are modified, but can still be identified and have energies  $\langle b|H|b\rangle = -6.4\text{eV}$  and  $\langle a|H|a\rangle = 0.1\text{eV}$ . By cutting all coupling matrix elements involving the bonding or antibonding state, the authors could analyze the transmission contribution of the antibonding and bonding state separately. The black curve in Fig.(2.9) presents the total transmission, while the two dashed curves are the transmissions through through the contact when the bonding or antibonding state is removed. From this study it becomes clear that the rather flat transmission plateau around the Fermi energy is due to the transmission of the antibonding state.

A very well established fact is that hydrogen dissociates on flat surfaces of simple and transition metals at room temperature (40; 41). On transition metals this happens because the hydrogen molecular orbitals get broadened and shifted down in energy due to the hybridization with the metal  $s$ -,  $p$ - and  $d$ -states. The antibonding state, which is initially above the Fermi level, crosses the Fermi level and gets partially filled which weakens the hydrogen bond. How far the preference for dissociation goes strongly depends on the coordination number of the metal atom. Surprisingly, for a Pt metal coordination number smaller than seven, bonding to molecular hydrogen is preferential (34). For

lower coordination the Pt-H<sub>2</sub> bond becomes still stronger. As discussed above, we have evidence that H<sub>2</sub> dissociates, even at 4.2K, on the Pt lead surfaces. Still, we find that the last conductance bridge is formed by a molecule. This agrees with the calculations that show a stronger binding for the molecule than for the atom. The molecule may arrive at the contact intact (e.g. from the gas phase, due to the finite vapor pressure) or it may reform from adsorbed atoms. The latter mechanism is suggested from the HD experiments. It is very well possible that atomic Pt-H-Pt contacts are being formed during the experiments, but their conductance is expected to be higher. They do not have a clean signature in the conductance histogram and are therefore less readily accessible for experimental investigation.

## 2.7 Stretching dependence of the vibration modes

In the previous sections we have presented the evidence for the formation of a Pt-H<sub>2</sub>-Pt bridge with a conductance of 1G<sub>0</sub>. By point contact spectroscopy (PCS) two vibration frequencies were identified for H<sub>2</sub> and HD and three for D<sub>2</sub>. In this section we want to determine which oscillation mode belongs to which frequency and the way to do it is by following the behavior of a given oscillation frequency while stretching the contact.

### 2.7.1 Theory

The DFT based calculations for the expected behavior of the vibration modes upon the stretching were done by K. S. Thygesen and K. W. Jacobsen for the model described in the previous section. The molecular contact is described in a supercell containing the hydrogen atoms and two 4-atom Pt pyramids attached to a Pt(111) slab containing four atomic layers. In the total energy calculations both the hydrogen atoms and the Pt pyramids were relaxed while the remaining Pt atoms were held fixed in the bulk structure. The vibration frequencies were obtained by diagonalizing the Hessian matrix for the two hydrogen atoms. The Hessian matrix is defined by  $\partial^2 E_0 / (\partial \tilde{u}_{n\alpha} \partial \tilde{u}_{m\beta})$ , where  $E_0$  is the ground state potential energy surface and  $\tilde{u}_{n\alpha}$  is the displacement of atom  $n$  in direction  $\alpha$  multiplied by the mass factor  $\sqrt{M_n}$ . In calculating the vibration modes all Pt atoms were kept fixed which is justified by the large difference in mass between H and Pt. In order to simulate the stretching process of the experiment, contacts for various lengths of the supercell were calculated. The bridge configuration is stable over a large distance range with the binding energy of the H<sub>2</sub> molecule varying from -0.92 eV to -0.47 eV, relative to gas phase H<sub>2</sub> and a broken Pt contact, over the range of stretching considered here. The H-H bond length stays close to 1.0 Å during the first stages of the stretching upon which it retracts and approaches the value of the free molecule. The hydrogen thus retains its molecular form and the elongation mainly affects the weaker Pt-H bond. For smaller electrode separations a structure with two hydrogen atoms adsorbed on the side of a Pt-Pt atomic contact becomes the preferred geometry, as also found

by García *et al.* (32). However, in the calculations by Thygesen *et al.*, the latter structure has a conductance of  $1.5 G_0$ , well above  $1 G_0$ . Moreover, this structure has at least three conduction channels with significant transmission, which will make a crucial difference between the two proposed structures. Indeed, the number of conduction channels and their individual transmissions strongly affect the shot noise level through the structure, as will be shown in Chapter 3. The calculation identifies six vibration modes whose stretching dependence is

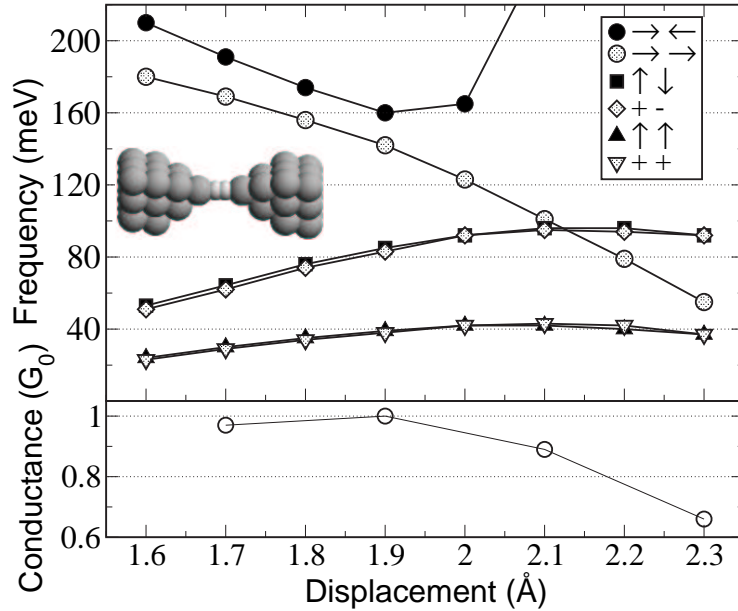


Figure 2.10: *Calculated vibrational frequencies for a hydrogen molecule in a Pt contact as a function of elongation of the supercell. The inset shows the atomic arrangement in the supercell and the legend inset presents the motions of the hydrogen molecule. The lower panel shows the calculated conductance. Figure after: K. S. Thygesen and K. W. Jacobsen, (35)*

presented in Fig.(2.10). The lower four modes are degenerate (two times two) and correspond to a transversal center-of-mass (CM) motion and a hindered rotation mode. The higher two modes are a longitudinal CM (lower) and the internal vibration of the molecule (higher). The presented prediction has a few remarkable characteristics which are qualitatively easy to distinguish in a measurement. The frequencies of two degenerate transversal vibration modes are increasing upon stretching, while the longitudinal two are decreasing at the same time, until the Pt-H bonds begin to break at which point the highest one starts to increase. It will turn out that the highest mode is too high in energy to be observed by PCS because the current through the junction becomes too high already around 100mV and the molecular junction breaks. The difference in behavior between the longitudinal and the transversal modes upon stretching is

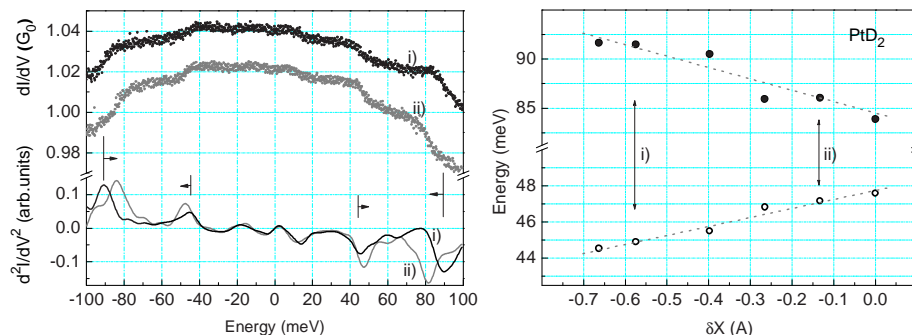


Figure 2.11: *Left:  $dI/dV$  (upper two curves) and corresponding numerical derivatives  $d^2I/dV^2$  (lower two curves) as a function of the energy. Both measurements i) and ii) are obtained on the same junction, except that the junction is stretched for about  $0.5\text{\AA}$  before the measurement ii). The arrows indicate the decreasing and increasing tendency of the higher and lower mode respectively. Right: Oscillation energy as a function of the stretching of the contact. The stretching distance is measured with respect to some arbitrary point when the contact was stretched almost to breaking, so effectively, the tension was relaxed gradually. The curves on the left are a part of the sequence from which the values in the right figure are obtained and the arrows indicate the values taken from the curves i) and ii) on the left.*

something that we will be looking for, more qualitatively than quantitatively. It is important to remember that the measurement which needs to be performed is on a very fragile molecular bridge and we essentially want to stretch the chemical bonds to test their elastic properties without breaking them.

## 2.7.2 Experiment

As already noticed in previous sections, our experimental window is roughly  $\pm 100\text{mV}$ . Increasing the bias further results in breakdown of the molecular bridge. The DFT stretching dependance for  $\text{H}_2$  shown in Fig.(2.10) predicts the lower longitudinal mode to start from  $180\text{meV}$  and only after the contact is stretched for about  $0.5\text{\AA}$  this mode will enter our experimental window. Experimentally, this turns to be impossible with  $\text{H}_2$ , but it is possible with  $\text{D}_2$  since all frequencies are scaled down by  $\sqrt{2}$ . A measurement which clearly shows the stretching behavior which we are looking for is presented in Fig.(2.11).

The triggering of a certain mode probably depends on the exact contact configuration and small asymmetries in the contact, so we have no control over the choice which mode will be excited, and what the signal strength will be. The measurement presented in Fig.(2.11) is one where two excited modes show the characteristic behavior predicted by Thygesen *et al.*, which suddenly clarifies the picture. The higher mode's frequency is decreasing as the contact is stretched, so it is a longitudinal mode, while the lower one with the frequency increasing

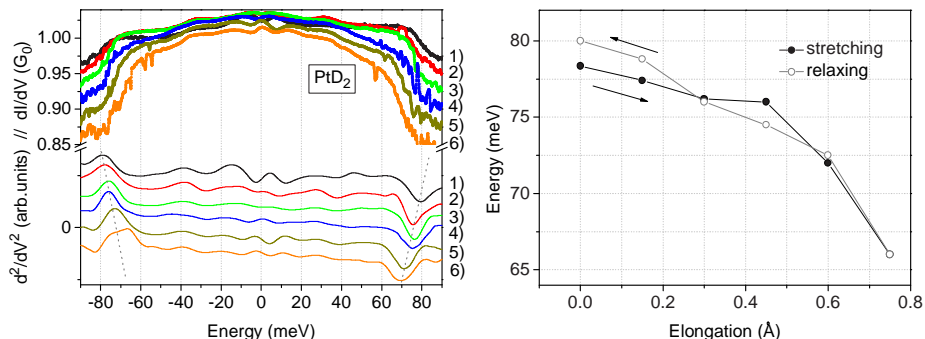


Figure 2.12: *Left: Sequence of  $dI/dV$  curves (upper) and its numerical derivatives  $d^2I/dV^2$  (lower) as a function of the energy. The numbers indicate the corresponding  $dI/dV$  and  $d^2I/dV^2$  curves and the order in which the curves were taken. Each next curve is taken on the same contact stretched for about  $0.15\text{\AA}$  with respect to the previous one. The total conductance also decreases slightly as the contact is stretched. Right: Vibration energy as a function of the elongation for the highest observed mode in the Pt- $D_2$ -Pt molecular junction of the left panel. The black dots correspond to stretching while the gray circles correspond to relaxing the same contact.*

upon stretching is a transversal one. While performing all measurements which are presented in Fig.(2.11 (*left*)) and Fig.(2.11(*right*)), the molecular bridge was not broken, only stretched. The measurement (*ii*) in the left panel is obtained on the same junction as (*i*), except that the junction is stretched for about  $0.5\text{\AA}$  and the shift in the frequencies can clearly be seen in the peaks in  $d^2I/dV^2$  curves. The total elongation of  $0.5\text{\AA}$  is to a large part taken up by the elasticity of the Pt leads. This prevents us from making a quantitative comparison of the slopes of the frequencies as a function of distance. The arrows indicate the decreasing and increasing tendency of the higher and the lower mode respectively. In Fig.(2.12) a measurement is presented where the contact was stable for a very long time (about an hour) without breaking. The presented sequence of recorded  $dI/dV$  curves shows clearly how the frequency decreases upon the stretching and increases as the stretching distance is reduced again. The stretching dependance of the lower modes in this case can not be clearly resolved. It is also interesting to notice that the total conductance decreases slightly as the contact is gradually stretched.

Fig.(2.13) presents the stretching dependance of the lowest two modes, in a Pt- $H_2$ -Pt junction centered around  $54\text{meV}$  and  $71\text{meV}$ . With these two modes we complete the picture of the stretching dependance of the vibration modes which we observe with  $H_2$  and  $D_2$ . As it was predicted by DFT calculations, the frequency of the lower two modes increase upon the stretching while the upper one decreases. In that interpretation it would mean that in the  $D_2$  experiments, the mode around  $38\text{meV}$  ( $54\text{meV}$  with  $H_2$ ) is the transversal CM mode. The

mode around 52meV (71meV with H<sub>2</sub>) is then the hindered rotation mode and the mode at 85meV the longitudinal center-of-mass. The highest mode is too high, and may only be accessible when using tritium.

Beside the model and the calculation done by Thygesen and Jacobsen, which agrees with our measurements very well and partial agreement with the computation of Garcìa - Suárez model (36), there are a few other models which agree less or do not agree at all. The shot noise measurement presented in Chapter 3 where we analyzed the number of conducting channels show clearly that the model developed by Thygesen et al. (and Garcìa - Suárez) remains the only one consistent with all so far measured properties of P-H<sub>2</sub>-Pt junctions.

## 2.8 Conclusions

In this chapter we have shown the evidence that the contact created by breaking a Pt wire in a MCBJ device can be bridged by molecular hydrogen, deuterium or HD. If dc conductance is continuously measured while breaking and making the contact, breaking traces show flat steps in the conductance at around 1G<sub>0</sub> which result in a sharp peak close to 1G<sub>0</sub> in the conductance histogram. Differential conductance measurements show three vibration excitation modes with D<sub>2</sub> and corresponding modes, within the measurement range, in the case of H<sub>2</sub> and HD substitutions which clearly demonstrate that it is a molecule bridging the contact and not an atom, and that different vibration modes were excited, not multiple excitations of the same one. The stretching dependence of vibration modes made it possible to conclude which modes correspond to which oscillation frequency. The theoretical predictions by Thygesen and Jacobsen, based on DFT calculations showed very good matching with the measured data in all

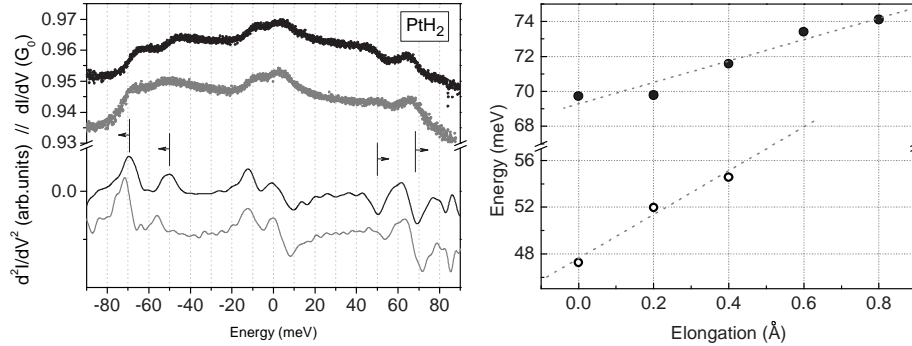


Figure 2.13: *Left:  $dI/dV$  (upper) and  $d^2I/dV^2$  (lower) curves as a function of the energy for a Pt-H<sub>2</sub>-Pt junction. The lower curve is taken on the junction stretched for about 0.2Å with respect to the upper one. Right: Vibration energy as a function of the elongation for the two lowest modes in Pt-H<sub>2</sub>-Pt molecular junction.*

aspects. The predicted conductance, the vibration frequencies of the Pt-H<sub>2</sub>-Pt contact and the stretching dependence of the oscillation frequencies match very well, while the total number of conducting channels will be shown to match well in chapter 3 devoted to shot noise.

At the end, as the final conclusion we can say that this system is well described theoretically and experimentally well understood so that it can serve as a benchmark system for theoretical analysis since it puts strong boundary conditions on calculations. Still, we are aware of one very important question which remains unanswered. It is the apparent broadening which is much bigger than the expected broadening due to finite temperature and the modulation amplitude, so this will be addressed in Chapter 6.

## Chapter 3

# Shot Noise measurements on single atoms and molecules

Published as Nano Lett. 2006, 6(4) 789-793

### 3.1 Motivation

Due to the discreteness of the electric charge, electric current can become very noisy when we get down to the atomic scale. The noise originating from the discreteness of electric charge is called shot noise and was discovered by Schottky 1918 (42) in vacuum tubes. The shot noise also exists in many other solid state systems like p-n junctions (43), metal-insulator-metal tunnel junctions (44) and a wide variety of mesoscopic structures. The basic idea that we want to exploit is that in a contact that has a completely transparent conductance channel at zero temperature, electron states are filled according to the Pauli principle and are coherent across the whole structure, so there is no difference in occupation numbers on the left and right end of contact. That would result in noiseless transport. But if the contact is not completely transparent ( $\tau \neq 1$ ) there will be reduced probability for electrons to get to the other side of the contact. It will split the electron state in two coherent states, transmitted and reflected, which effectively results in a difference in occupation numbers on two sides of the contact. The situation is shown in Fig.(3.1) where the right moving states are fully populated up to  $E_F + eV$  on the left side of the constriction, while on the right they fill only a fraction  $\tau_n$  in the energy range between  $E_F$  and  $E_F + eV$ . If the conductance is carried by a completely transmitting conductance channel, shot noise  $S_I = 0$ . Otherwise, the shot noise has a finite value. In this work we will concentrate on the shot noise experiments done on single molecules and single atom contacts. We used the shot noise as a tool to determine the

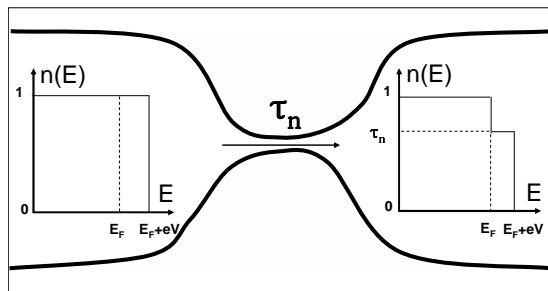


Figure 3.1:  $\tau_n$  is the probability that an electron gets transmitted, meaning that on the other side of contact that state is occupied with a probability  $\tau_n$ . That results in a difference in occupation numbers of right-moving states on the two sides of the contact.

transport characteristics of a Pt-D<sub>2</sub>-Pt junction.

## 3.2 Introduction to shot noise

In systems like vacuum tubes there is no correlation between the electrons on the two electrodes, so the tunnelling events are entirely random. The shot noise spectral density is defined as a Fourier transform  $F$  of the time correlation function of the current  $F(\langle I(t)I(t') \rangle) = S_I(\omega)$ . The formula for shot noise in the tunnelling regime is (45):

$$S_I(\omega) = 2q\langle I(t) \rangle$$

The factor 2 enters because in measurement we take the Fourier transform only in the positive frequency domain. This is the expression for what is called "full shot noise" and it shows three main features of shot noise: it is proportional to the average current, it is proportional to the charge of the carriers  $q$  (in this case it is  $e$ , but it can be  $e/3$  as in the fractional Hall effect, or  $2e$ ,  $3e\dots$  in multiple Andreev reflections (46)) and it is white in the whole frequency domain, up to the frequencies determined by the relaxation time of the electrons.

### 3.2.1 Shot noise in mesoscopic systems

In systems having correlation between the carriers, shot noise is lowered by a certain factor with respect to the full Poissonian value (47). We consider the low temperature limit where  $eV \gg kT$ . There are three different scattering lengths that determine the shot noise with respect to the length ( $L$ ) of the mesoscopic system. These are the elastic mean free path  $l_e$ , the length  $L_{e-e}$  in which electrons thermalize in collisions among themselves and the electron-phonon scattering length  $L_{e-ph}$  in which electrons thermalize to the crystal lattice temperature. For metals at low temperatures, these are usually arranged

in the following order  $l_e \ll L_{e-e} \ll L_{e-ph}$ . If  $L \ll l_e$ , we speak of the ballistic regime where the electron is in a coherent state across the whole structure and there shot noise vanishes, except for single channel effects (48) which is the main interest of this work and will be discussed separately. In the upper, diffusive

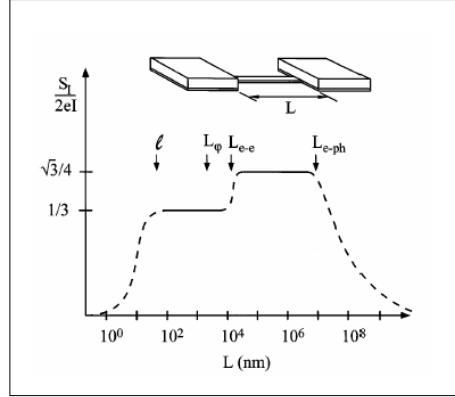


Figure 3.2: Shot noise vs. sample length  $L$ , expected for a diffusive wire in the regime  $eV \gg k_B T$ . The arrows indicate the relative lengths predicted for  $V = 100 \mu V$ . After ref. (47)

limit, when  $L \gg L_{e-ph}$ , the phase coherence is destroyed before the electron leaves the scattering region and shot noise vanishes as well, so the total noise is  $S = 4k_B T/R$  (Johnson-Nyquist noise) (49). The regime where  $L_{e-e} \ll L \ll L_{e-ph}$ , is called interacting hot-electron regime. Electrons thermalize among themselves due to collisions, but do not interact with the phonons, so they are on a higher temperature. Shot noise in this case is  $S_I = (\sqrt{3}/4)2eI$  (47). In the case where  $l_e \ll L \ll L_{e-e}$  we are in the noninteracting hot electron regime, where the distribution function has a double step profile (50) since electrons do not interact inelastically among themselves and the distribution function is just a linear combination for left and right moving states, as a function of length. Shot noise is predicted to be  $S_I = (1/3)2eI$ . The dependance of the reduction factors as a function of the critical length is presented in Fig.(3.2)(47).

### 3.2.2 Shot noise in point contacts

Since noise is a fluctuation around the mean value, the current noise is

$$\Delta \hat{I}(t) = \hat{I}(t) - \langle \hat{I}(t) \rangle. \quad (3.1)$$

By applying a Fourier transform, we switch from time to frequency domain. According to Landau and Lifshitz (51), for the spectral density of such fluctuations we get:

$$2\pi\delta(\omega + \omega')S(\omega) = \langle \Delta \hat{I}(\omega) \hat{I}(\omega') \rangle + \Delta \hat{I}(\omega') \hat{I}(\omega) \quad (3.2)$$

Since we are interested in shot noise in the ballistic regime where the current through the contact can be determined by Landauer's scattering model, here we use the formulas derived in chapter 1.

$$\begin{aligned}\hat{I}(t) &= \frac{e}{\hbar} \int \int dE dE' (\hat{a}_1^\dagger(E) \hat{a}_1(E') - \hat{b}_1^\dagger(E) \hat{b}_1(E')) e^{i(E-E')t/\hbar} = \\ &= \frac{e}{\hbar} \int \int dE dE' (\hat{a}_1^\dagger(E) \hat{a}_1(E') - (s_{1,\alpha}^* a_\alpha^\dagger)(s_{1,\beta} a_\beta)) e^{i(E-E')t/\hbar}. \quad (3.3)\end{aligned}$$

With the operator  $A_{\alpha\beta} = \delta_{\alpha 1} \delta_{\beta 1} - s_{1,\alpha}^* s_{1,\beta}$ , the expression for the current can be written in more compact form:

$$\hat{I}(t) = \frac{e}{\hbar} \int \int dE dE' A_{\alpha\beta} \hat{a}_\alpha^\dagger(E) \hat{a}_\beta(E') e^{i(E-E')t/\hbar} \quad (3.4)$$

Now formula (3.1) can be written in more explicit form:

$$\Delta \hat{I}(t) = \frac{e}{\hbar} \int \int dE dE' \sum_{\alpha,\beta=1,2} A_{\alpha,\beta} [\hat{a}_\alpha^\dagger(E) \hat{a}_\beta(E') - \langle \hat{a}_\alpha^\dagger(E) \hat{a}_\beta(E') \rangle] e^{i(E-E')t/\hbar} \quad (3.5)$$

Taking a Fourier transform, we get:

$$\begin{aligned}\Delta \hat{I}(\omega) &= \frac{e}{\hbar} \int \int dE dE' dt \sum_{\alpha,\beta=1,2} A_{\alpha,\beta} [\hat{a}_\alpha^\dagger(E) \hat{a}_\beta(E') \\ &\quad - \langle \hat{a}_\alpha^\dagger(E) \hat{a}_\beta(E') \rangle] e^{i(E-E'+\hbar\omega)t/\hbar} \\ &= e \int dE \sum_{\alpha,\beta=1,2} A_{\alpha,\beta} [\hat{a}_\alpha^\dagger(E) \hat{a}_\beta(E + \hbar\omega) \\ &\quad - \langle \hat{a}_\alpha^\dagger(E) \hat{a}_\beta(E + \hbar\omega) \rangle]. \quad (3.6)\end{aligned}$$

So the spectral density is:

$$\begin{aligned}\langle \Delta \hat{I}(\omega) \Delta \hat{I}(\omega') \rangle &= e^2 \int \int dE dE' \sum_{\alpha,\beta,\gamma,\delta=1,2} A_{\alpha\beta} A_{\gamma\delta} \times \\ &\quad \times [ \langle \hat{a}_\alpha^\dagger(E) \hat{a}_\beta(E + \hbar\omega) \hat{a}_\gamma^\dagger(E') \hat{a}_\delta(E' + \hbar\omega') \rangle \\ &\quad - \langle \hat{a}_\alpha^\dagger(E) \hat{a}_\beta(E + \hbar\omega) \rangle \langle \hat{a}_\gamma^\dagger(E') \hat{a}_\delta(E' + \hbar\omega') \rangle ] \quad (3.7)\end{aligned}$$

To calculate the mean value of the product of creation and annihilation operators, we can use Wick's theorem. This theorem breaks the problem in calculating the contractions of the pairs of operators using anticommutation relations. In this particular case (52):

$$\begin{aligned}&\langle \hat{a}_\alpha^\dagger(E) \hat{a}_\beta(E + \hbar\omega) \hat{a}_\gamma^\dagger(E') \hat{a}_\delta(E' + \hbar\omega') \rangle - \\ &\quad - \langle \hat{a}_\alpha^\dagger(E) \hat{a}_\beta(E + \hbar\omega) \rangle \langle \hat{a}_\gamma^\dagger(E') \hat{a}_\delta(E' + \hbar\omega') \rangle = \\ &= \delta_{\alpha\delta} \delta_{\beta\gamma} \delta(E - E' - \hbar\omega') \delta(E + \hbar\omega - E') f_\alpha(E) [1 - f_\beta(E + \hbar\omega)] \quad (3.8)\end{aligned}$$

So the expression for the spectrum density gets a simpler form:

$$\langle \Delta \hat{I}(\omega) \Delta \hat{I}(\omega') \rangle = \frac{e^2}{\hbar} \delta(\omega + \omega') \int dE \sum_{\alpha, \beta=1,2} A_{\alpha\beta}^2 f_{\alpha}(E) [1 - f_{\beta}(E + \hbar\omega)] \quad (3.9)$$

The frequency range that we are interested in is much below 1GHz, so  $\hbar\omega$  is much smaller than the typical energy scale on which the transmission coefficients can have any significant variation with respect to the value at  $E_F$  and we can safely assume  $\omega = 0$ . So far, spin degeneracy was not included. From the expressions (3.2) and (3.9) follows:

$$S_I = \frac{4e^2}{h} \int dE \sum_{\alpha, \beta=1,2} A_{\alpha\beta}^2 f_{\alpha}(E) [1 - f_{\beta}(E)] \quad (3.10)$$

where the factor 2 for spin is now taken into account. Assuming a single relevant conductance channel with transmission  $\tau$  we can write the operator  $A_{\alpha\beta} = \delta_{\alpha 1} \delta_{\beta 1} - s_{1\alpha}^* s_{1\beta}$  in terms of  $\tau$  and we get:

$$S_I = \frac{4e^2}{h} \int dE \{ \tau^2 (f_1(E)(1 - f_1(E)) + f_2(E)(1 - f_2(E))) + \tau(1 - \tau) \times \\ \times (f_1(E) - f_2(E))^2 \} = \frac{4e^2}{h} \{ 2k_B T \tau^2 + eV \coth[\frac{eV}{2k_B T}] \tau(1 - \tau) \} \quad (3.11)$$

what finally, in the low temperature limit ( $eV \gg 2k_B T$ ) gives:

$$S_I = 2eVG_0\tau(1 - \tau) \quad (3.12)$$

The derived relations are valid for the conductance trough a single channel, but generalization to a multichannel system is straight forward since the decomposition in conductance channels is linearly independent. If  $(\tau_1, \dots, \tau_N)$  is a set of transmission coefficients for a given contact, than the relation (3.11) becomes:

$$S_I = 2G_0 eV \coth[\frac{eV}{2k_B T}] \sum_i \tau_i (1 - \tau_i) + 4k_B T G_0 \sum_i \tau_i^2, \quad (3.13)$$

which is known as Lesoviks expression (53), and in the zero temperature limit it gives:

$$S_I = 2eVG_0 \sum_i \tau_i (1 - \tau_i) = 2eI \frac{\sum_i \tau_i (1 - \tau_i)}{\sum_i \tau_i} \quad (3.14)$$

where

$$F(\tau_1, \dots, \tau_N) = \frac{\sum_i \tau_i (1 - \tau_i)}{\sum_i \tau_i}, \quad (3.15)$$

is the so-called Fano factor. This factor is always smaller than 1 and it shows how much the shot noise is lowered from its full, poissonian value, due to correlations among the electrons. The set of transmission coefficients  $(\tau_1, \dots, \tau_N)$  for a certain contact is also called the mesoscopic PIN code of the contact. When given for a single atom contact, it completely represents the conductance properties of this contact.

### Shot noise in 2D electron gas

It is obvious from the expression (3.15) that the Fano factor is zero for the two extreme values of transmission coefficients; if all transmission channels are completely opened or if all of them are closed, so  $\tau = 1$  or  $\tau = 0$ . The first experiment to probe this was done by Reznikov *et al.*(54), who measured in the high frequency range 8-18GHz, in order not to suffer from  $1/f$  noise. Inspired by the experiment done by van Wees *et al.* (2) in which they used a gate electrode to confine the electron gas, so they could change the conductance of the constriction continuously, Reznikov *et al.* monitored how the shot noise power spectrum changed with the conductance. The conductance in this experiment is changing continuously such that only one conductance channel can be partially opened, while all others are fully opened or completely closed, so one can follow how the shot noise oscillates with the conductance. Reznikov *et al.* also measured the linear dependence of the shot noise as a function of the current through the contact. The experiments were soon continued in the low frequency range by Kumar *et al.* (55).

### 3.3 Shot noise experiments on gold with MCBJ

Since the conductance measurements done with the use of Mechanically Controllable Break Junctions (MCBJ) (56) on gold showed quantized conductance steps, van den Brom *et al.* had the idea to use the shot noise as a tool to investigate how many conductance channels are actually contributing to transport in a single atom contact of gold (57). The most important results are presented in the Fig.(3.3). The experiment where the conductance was kept fixed and the current through the contact was varied, showed linear dependence of the shot noise as a function of the bias current, with the noise strongly suppressed for the contacts with the conductance close to  $1G_0$ . The other type of experiment was the shot noise as a function of the conductance, where they measured the shot noise while changing the conductance of the contact by breaking it, and the current through the contact was kept constant. The most remarkable result was obtained in the experiment done for 27 contacts with different conductances from tunnelling to  $4G_0$  with constant biasing current of  $0.9\mu\text{A}$  (right graph in Fig.(3.3)). They observed very strong shot noise suppression as they approached integer values of conductance. The effect is especially pronounced for the  $1G_0$  value which proved that the conductance of  $1G_0$  is due to one channel very close to  $\tau = 1$  (57).

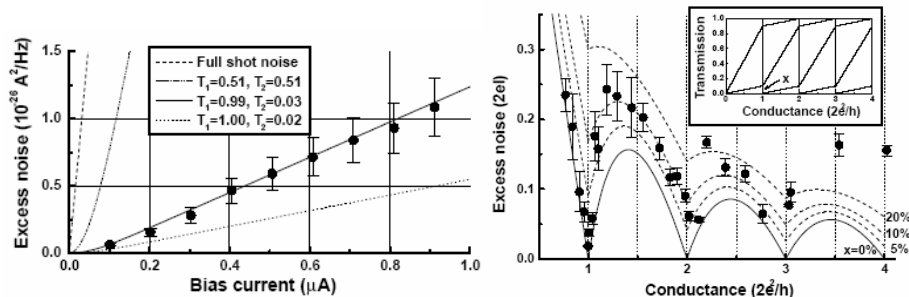


Figure 3.3: The right graph shows the shot noise measured on 27 different contacts, at 4.2K and bias current of  $0.9\mu A$ . In the tunnelling limit, shot noise approaches the full poissonian value, while for  $G = nG_0$  it is strongly suppressed. The left graph shows the shot noise measured for a fixed contact with  $G = 1.02G_0$  with different bias currents and theoretical fits for a different partial transmissions of the channels contributing to the conductance. After ref. (7).

## 3.4 Shot noise in the current through a Pt-H<sub>2</sub>-Pt junction

### 3.4.1 Motivation

After the discovery of the Pt-H<sub>2</sub>-Pt bridge (20), several theoretical analyses were done trying to understand what is the mechanism of conductance through the bridge (20; 34; 32; 33; 36). But different groups had different ideas and also arrived at different conclusions, which were often in contradiction. Garcia *et al.* (32) proposed a configuration in which the molecule would have three conductance channels contributing to the conductance of the junction with  $G \simeq 1G_0$ , while the others proposed one conduction channel responsible for the transport (34; 33). The stretching dependence of the vibration excitations already speaks in favor of the longitudinal orientation of the molecule, rather than perpendicular, but to determine the number of conductance channels, which will make a direct distinction, we decided to measure shot noise through the contact. The big difference in number of conducting channels (the longitudinal orientation has one completely opened and the transversal orientation has 3 partially opened conductance channels) between the models makes a large difference in the level of shot noise. Inspired by the measurements on gold done by van den Brom *et al.*, we designed an experiment in which we used shot noise as a tool to investigate the number of conductance channels responsible for the conductance through the D<sub>2</sub> molecule bridging the gap between two atomically sharp Pt tips <sup>1</sup>. Previous measurements (20) showed that voltage-dependent conductance

<sup>1</sup>The electronic structure of H<sub>2</sub> and D<sub>2</sub> are identical and for the shot noise measurements we used D<sub>2</sub> because it is heavier and has lower phonon energies which has some technical advantages already discussed in chapter 2.

fluctuations are strongly suppressed for the Pt/H<sub>2</sub> junction with a conductance close to 1G<sub>0</sub>, suggesting that only one channel is conducting. However, this is a statistical method and it is not possible to relate it directly with any particular geometrical orientation of the molecule. Our shot noise measurements are done on one particular Pt-D<sub>2</sub>-Pt contact, carefully characterized by spectroscopical methods and controlled during the measurement to make sure that it does not change the geometrical arrangement. For such controlled structures we show below that the number of conductance channels is very close to 1.

### 3.4.2 Experimental setup

The setup is designed to measure a noise signal of the order of 10<sup>-18</sup>V<sup>2</sup>/Hz (see Fig.3.4). The resistance of the junction where the noise is measured is around 13kΩ which makes current noise of the order of 10<sup>-26</sup>A<sup>2</sup>/Hz so we are extremely sensitive on any external electromagnetic, mechanical or acoustic noise. Therefore, the whole setup is placed in a home made Faraday cage with acoustic and mechanical isolation. As a cryostat we used a transport Dewar placed in the Faraday cage. Very important is that all parts of the setup, the Faraday cage, the Dewar and the dipstick are decoupled from any ground. They will be connected at the end to one star point and wired to the ground. The grounding problem is very important in this experiment.

The electronic part of the setup consists of the part used for spectroscopy which was discussed earlier, and the noise measurement part. The switching box, used to change between these two measurements is also placed in the Faraday cage. The measured noise is picked up by two parallel two-stage amplifier sets. The first stages are NF Electronic Instruments (model *LI - 75A*) Low Noise Preamplifiers with a fixed amplification  $A = 100$ . The second stage are EG&G Instruments (model 5184) Low Noise Preamplifier with  $A = 1000$ .

After the two-stage amplification, the signal goes to the Stanford Research SR780 Network Signal Analyzer which takes a Fast Fourier Transform (FFT) of both signals. The intrinsic noise of our amplifiers already exceeds the expected shot noise level we are interested in, but the random and uncorrelated noise produced by the amplifiers can be rejected by calculating the cross spectrum of the Fourier transforms of the two independent amplification channels. The cross spectrum is a vector average of the product of two FFT signals and is obtained in the following way: FFT of the signal is a complex number, so beside the amplitude contains the phase information. Vector average averages the real and imaginary part separately. If two signals are correlated, they have the same phase and by multiplying them, they always enter the total sum with a positive sign. The uncorrelated signals will be averaged out since they enter the sum with positive and negative signs randomly.

### 3.4.3 Testing of the setup on gold

To verify that our setup works properly, we tried to reproduce some of the results obtained by van den Brom *et al.*. Figure (3.5) shows some measurements done on

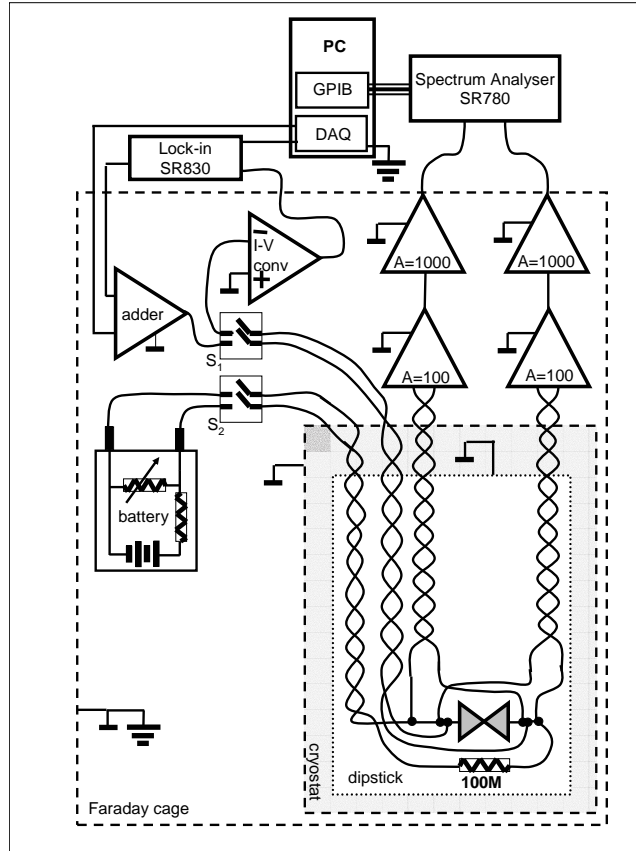


Figure 3.4: Schematic drawing of experimental setup used for simultaneous PCS and shot noise measurements at 4.2K. The dipstick with the sample chamber is under vacuum and inserted in the cryostat which is filled with liquid He. The cryostat (metal transport vessel) is put inside the Faraday cage. All amplifiers are also kept in the Faraday cage. Common ground nodes are connected together on one point and grounded to the safety ground. A set of switches,  $S_1$  and  $S_2$ , is used to change between the PCS and shot noise measurements. In current biased shot noise measurement ( $S_1$  open,  $S_2$  closed), the current through the contact is controlled by a divider on a battery. The signal is picked up by two separated Cu wire twisted pairs, then is amplified 100000 times by two stages of low noise amplifiers (NF Electronic Instruments (model LI-75A) and EG&G Instruments (model 5184)) and sent to a Stanford Research SR780 Network Signal Analyzer which takes a Fast Fourier Transform (FFT) of both signals and calculates the cross spectrum of left and right signals. The cross spectrum from the SR780 is finally through the GPIB sent to the PC. The setup is converted for PCS measurements by closing  $S_1$  and opening  $S_2$ .

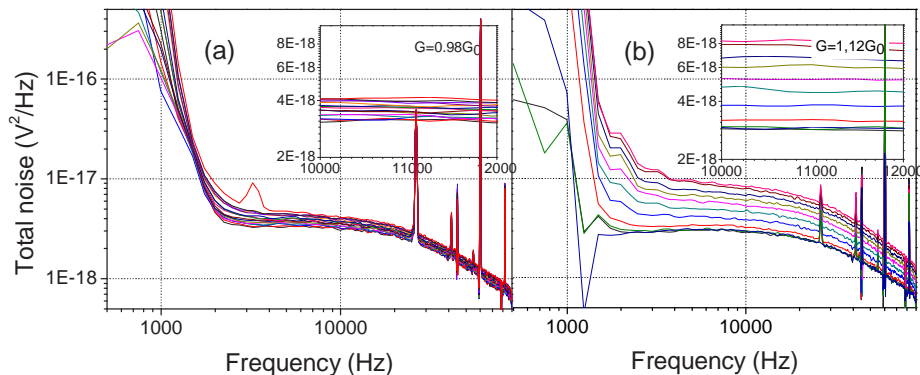


Figure 3.5: *Raw data obtained for two gold contacts with different conductances. (a)  $G=0.98G_0$  and the current through the contact is gradually changed from 0 to  $0.8\mu A$  in steps of  $0.1\mu A$ . In panel (b)  $G=1.12G_0$  and the current is changed in steps of  $0.05\mu A$ . The lowest curve in both figures is the thermal noise curve ( $I = 0A$ ). The two insets show the same data for the limited frequency range from 10 to 12kHz on an expanded scale.*

Au contacts with different conductances. The noise measurements we performed consist of the following steps. After we set up the contact to the desired value by measuring the conductance in a voltage biased measurement, we read a thermal noise spectrum of the contact (the lowest curves in Fig.(3.5)). A single noise curve is 1000 times averaged, which takes about one minute. There are a few remarkable features in the thermal noise curve. The thermal noise should be white, but in our case it has a high value at the low frequency part and a strongly pronounced roll-off at high frequencies. The lower frequency part is dominated by the noise which could be the acoustic noise from the environment. The roll-off is due to the fact that our circuit actually behaves as a low pass filter with four capacitances (two amplifier sets, the contact itself and the current source) and the resistances formed by wire resistances and the resistance of the contact itself and the leads. The sharp glitches are due to pick up from the power supplies, electromagnetic fields and, at lower frequencies, the acoustic noise, despite the precautions and careful shielding. Since the thermal noise is white in its nature and depends only on the previously determined resistance of the contact, we can use the zero bias curve to obtain the transfer characteristic of our setup. Fitting the thermal noise curve with a low pass filter transfer function in the higher frequency domain where the  $1/f$  noise is negligibly small, we obtain the parameters for the correction due to roll-off.

After recording the thermal noise curve, we start with the current biased measurements and the curves obtained can be seen in Fig.(3.5). The conductance of the contact is verified after each current increase and found to remain unchanged, although we are aware that the same conductance does not necessarily mean that the contact is kept unchanged. The excess noise is obtained

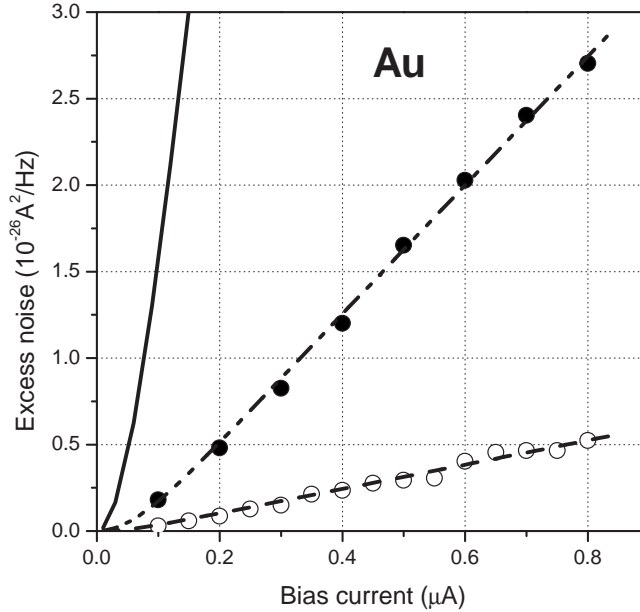


Figure 3.6: *Excess noise as a function of the bias current. The filled dots present excess noise measured on the contact with  $G=1.12G_0$  and the open dots for a contact with  $G=0.98G_0$ . Fitting the data with the expression for excess noise (3.16) gives the decomposition of the total conductance in terms of the conduction channels  $\{\tau_1 = 0.985, \tau_2 = 0.133\}$  for  $G=1.12G_0$  and  $\{\tau_1 = 0.978\}$  for  $G=0.98G_0$ .*

by subtracting the thermal noise from each of the current biased curves. The roll-off is corrected using the parameters obtained from the thermal noise curve for each given contact. The sharp spikes are mainly removed by subtracting the thermal noise. By plotting the excess noise as a function of the applied current we can extract the Fano factor. In the zero temperature limit a linear fit would give the Fano factor, and knowing the total conductance we could determine the transmission coefficients  $\tau_i$ , if only two channels are contributing. But it is more accurate to include the temperature using the Lesovik expression (3.13) for the noise from which the thermal part, so the Johnson-Nyquist noise, is subtracted. The formula for the excess noise is:

$$S_{ex}(I) = 4k_B T G \left[ \frac{2eI}{4k_B T G} \left( 1 - \frac{\sum_i \tau_i^2}{\sum_i \tau_i} \right) \coth\left(\frac{2eI}{4k_B T G}\right) + \frac{\sum_i \tau_i^2}{\sum_i \tau_i} - 1 \right] \quad (3.16)$$

Fitting the data obtained for the two Au contacts presented in Fig.(3.5) with  $S_{ex}(I, T=4.2K)$  is shown in Fig.(3.6). The black curve represents the full shot noise. Filled and open circles are the measured data, while the excess noise fit is presented by the dashed lines. For the contact with  $G=0.98G_0$  we get a Fano factor  $F=0.022$ . As it is expected, the total conductance is due to a

single conductance channel with transmission  $\tau = 0.98$ . For the contact with  $G=1.12G_0$  the best fit presented in Fig.(3.6) gives a Fano factor  $F=0.116$ . This can not be described by a single partially open channel. If we assume that the conductance of  $G=1.12G_0$  is made up of two channels with  $\tau_1=1$  and  $\tau_2=0.12$  we obtain a Fano factor  $F=0.106$ . There may be a small admixture of a third channel, or the first channel transmission can be somewhat suppressed. The experimental value of  $F=0.116$  is consistent with  $\tau_1=0.985$  and  $\tau_2=0.133$ . In this case as well, the conductance is mainly due to one highly transparent channel and the second channel can be a contribution from tunnelling between the closest orbitals on two sides which are still too far apart to form a good contact. So, our results are in good agreement with the experiments on gold performed by van den Brom *et al.*

#### 3.4.4 Measurements on a Pt-D<sub>2</sub>-Pt bridge

Concluding that the test on gold contacts was successful, we are ready to use the shot noise as a tool to investigate the transmission coefficients of Pt-D<sub>2</sub>-Pt bridges. This measurement is somewhat different from the previous measurements since it combines two very sensitive measurement techniques, point contact spectroscopy and shot noise, both on a very fragile object, a single molecule bridge. To complete a measurement successfully one has to obtain a reasonably long series of shot noise measurements, for at least 4 or 5 different bias currents, where after each current change a  $dI/dV$  spectra is taken to verify that a contact did not change. This requirement means that the particular junction has to stay stable, without breaking, during the whole measurement which typically takes about 30 minutes. The calibration of the measurement accuracy for the conductance is done on a fixed resistor which is measured with three separate high precision dc ohmmeters. The obtained value ( $R=9.9748k\Omega$ ) is compared with the resistance measured on the same resistor placed in the measurement circuit instead of sample. The resistance measured by lock-in at 7.7kHz was around 1% higher than the resistance measured by dc method. Therefore we conclude that we correct for this systematic error of 1% and we estimate the random accuracy of the conductance measurement to 0.5%. This accuracy is the limiting factor in determining the transmission coefficients.

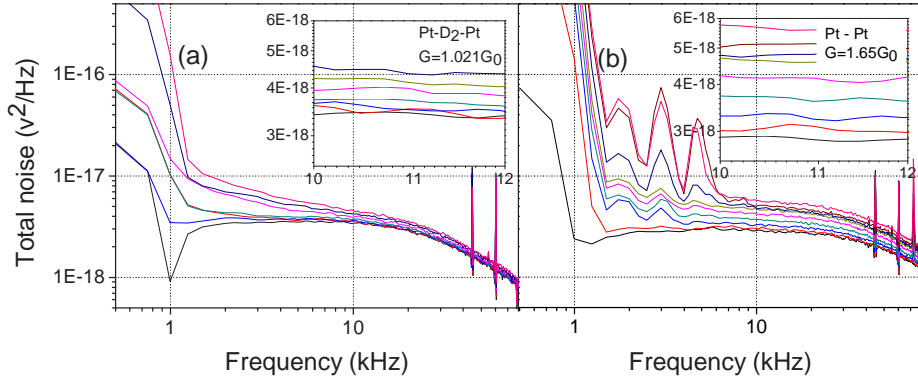


Figure 3.7: Noise as a function of the bias current for: a)  $Pt-D_2-Pt$  bridge and b) pure  $Pt$  single atom contact. The insets show the reduced range 10-12 kHz on an expanded scale. The bias current is increasing from 0 (thermal noise spectra) to  $0.8\mu A$ . After each current adjustment, the contact is verified to remain unchanged by a  $dI/dV$  measurement.

After a routine procedure of characterizing the sample by taking a conductance histogram of clean  $Pt$  to verify that the sample and the environment are not contaminated, we start the noise measurements on the  $Pt$  contact without  $D_2$ . The contact was set to  $G=1.65G_0$ , which is a typical conductance for a chain of few  $Pt$  atoms. Like in the experiment on  $Au$ , we make a series of noise measurements with different bias currents. The raw noise spectra are presented in Fig.(3.7(b)) and the excess noise as a function of the current in Fig.(3.8) by open circles. By fitting the expression for excess noise, we get the Fano factor  $F=0.14$  which can be obtained from two channels  $\{\tau_1 = 1, \tau_2 = 0.65\}$ . One should notice that this observation does not agree with the theoretical prediction for the conductance trough the  $Pt$  chain of atoms or the point contact. Different groups predict slightly different decompositions in conductance channels which makes Fano factors slightly different, but around the value  $F=0.35$  (33), while our experimentally measured value is much smaller. This deserves to be studied further.

After injecting the molecular  $D_2$  in the sample chamber and observing the required change in conductance histogram, we start with a careful characterization of the junction using point contact spectroscopy. To justify that we have a  $D_2$  molecule in the contact, we make a series of  $dI/dV$  measurements where in every next measurement, the bridge is stretched for  $\delta d (\sim 0.3\text{\AA})$ , as was already described in Chapter 2. Figure (3.9) shows one of such measured sequences. It can be seen very clearly that the high frequency mode ( 80meV) decreases as the contact is stretched, which is the expected energy and the expected behavior for the longitudinal mode in  $Pt-D_2-Pt$  bridge. A little bit less pronounced because of the smaller  $\delta G$  is the increasing behavior of the hindered rotation mode positioned at 40meV, again as expected, so we can conclude that we are

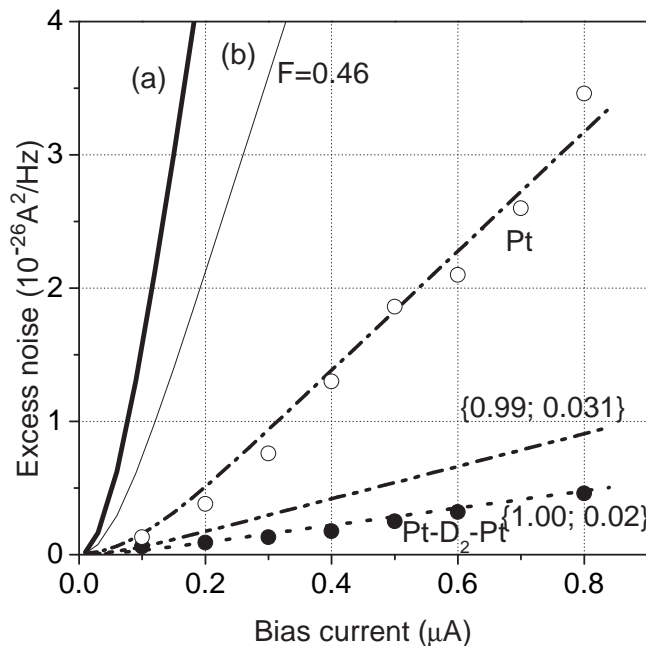


Figure 3.8: *Excess noise as a function of the bias current. Open and filled dots represent the measurements for Pt and Pt-D<sub>2</sub>-Pt respectively. The contact containing D<sub>2</sub> with  $G=1.02G_0$  gives the decomposition  $\{\tau_1 = 1.00; \tau_2 = 0.02\}$  and Fano factor  $F=0.020$ . For comparison, the model proposed by Garcia gives Fano factor  $F=0.46$  represented by the curve (b) in the same graph. The sensitivity of the method is demonstrated by the curve on the same graph with  $\{\tau_1 = 0.99, \tau_2 = 0.031\}$  and Fano factor  $F=0.032$ . The best fit for a clean Pt contact with  $G=1.65G_0$  gives a Fano factor  $F=0.14$ . Curve (a) indicates the full shot noise.*

measuring on an Pt-D<sub>2</sub>-Pt bridge.

Without breaking the bridge characterized in Fig.(3.9), we start the series of shot noise measurements in the configuration characterized by the thick black curve in Fig.(3.9). After each change of bias current, a  $dI/dV$  spectrum is taken to verify that the contact configuration did not change. Raw measurement data are shown in figure 3.7a. In Fig.(3.8) is represented the excess noise as a function of applied current. Using the fitting function (3.6) in the same way as in the case of gold, we calculate the decomposition in conductance channels.

In the expression (3.16), the fitting parameters are the temperature  $T$  and the  $\tau_i$  coefficients. The temperature is known from the experiment, so the transmission coefficients  $\tau_i$  are the fitting parameters to be determined. Knowing that total conductance of our contact is  $G = 1.02G_0$ , we decompose the conductance into two channels. The results for two different decompositions are shown on the Fig.(3.8), which clearly demonstrates the sensitivity of the fitting function.

The best fit is obtained for  $\{\tau_1 = 1.000; \tau_2 = 0.021\}$ . The Fano factor for this particular decomposition is  $F=0.02$ , while the choice of slightly different parameters  $\{\tau_1 = 0.99; \tau_2 = 0.031\}$  gives too high noise level, as can be seen from the curve in the same figure. The set of transmission coefficients for a Pt-H<sub>2</sub>-Pt junction proposed by Garcia (32) is  $\{\tau_1 = 0.7; \tau_2 = 0.2; \tau_3 = 0.1\}$  and it gives obviously too high shot noise level presented by the curve (b) in the same figure, which clearly disqualifies the proposed channel decomposition. Moreover, this entirely disqualifies the proposed model, already discussed in Chapter 2, where Garcia and coauthors claim that the H<sub>2</sub> molecule forms a sort of Pt<sub>2</sub>H<sub>2</sub> complex with the top Pt atoms.

### 3.5 Conclusions

In the world of single molecule transport properties, many experiments are designed and many behaviors of certain molecules under variety of physical conditions are reported, but the investigated molecules usually tend to be quite complex, which makes them very complicated for clear analysis and quantitative representation in terms of fundamental values like the number of conductance channels, transmission coefficients as well as the total number, excitation en-

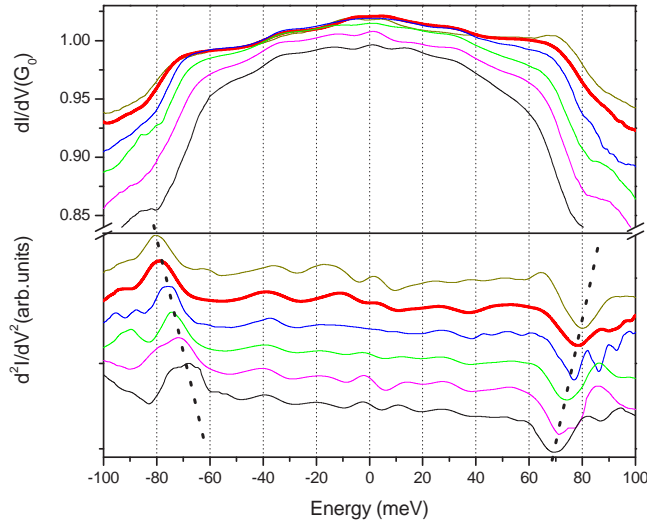


Figure 3.9: *The series of differential conductance measurements (upper figure) recorded for one particular Pt-D<sub>2</sub>-Pt contact as a function of contact stretching. Estimated elongation of the contact for each next curve is about 0.3Å, starting from the top one. The lower figure is a numeric derivative of the curves in the upper graph and the dotted lines follow the motion of the central frequency of the particular excitation. The thick curve indicates the configuration on which the shot noise measurements are performed.*

ergies and spatial motion of the vibration modes. Although the progress in a number of reported measurements and theoretical state-of-the art calculations is evident, comparing such measurements with the theoretical predictions is very difficult and the disagreements between the two is often huge, even for the simplest systems. In this chapter we tried to clarify the disagreements arising from the transmission. The main motivation of the shot noise measurement on a Pt-H<sub>2</sub>-Pt bridge was to clarify how many conductance channels are contributing to conductance of  $1G_0$ , which is the experimentally determined conductance of this junction. Beside the dc conductance of  $1G_0$  obtained in the form of conductance histograms in voltage biased experiments, we are able to measure the differential conductance, and by that method, identify and characterize the vibration modes, as is discussed in Chapter 2. The shot noise was already successfully used as a tool in point contact measurements by van den Brom, to determine the number of conducting channels for a single atom contact of gold so we introduced it as a tool in measurements on single molecules. The analysis presented in Fig.(3.8) unambiguously shows that the conductance through the Pt-D<sub>2</sub>-Pt junction is carried by mainly one, nearly perfectly transparent channel, which agrees beautifully with the results by Thygesen and Jacobsen, Cuevas, but does not agree with the findings of the calculations done by Garcia *et al.*(32). The measurements thus provide a means to discriminate between several theoretical approaches and may provide a means to tune the computations for molecular electronics problems.

## Chapter 4

# The width of vibration signals in experiments with molecules

This work is performed in collaboration with Magnus Paulsson.

### 4.1 Introduction

The analysis of molecular bridges studied in this thesis is strongly based on Point Contact Spectroscopy (PCS). The aim of this chapter is to discuss the origin of the width of the vibration-caused steps in  $dI/dV$  curves. The fits are obtained by the One Level Model (OLM) by Magnus Paulsson *et al.* (16) where the temperature of electron gas is a fitting parameter. That temperature is usually significantly higher than the bath temperature (4.2K), usually between 10K and 30K. As it is shown below, the thermal noise measurements on the same system show the temperature at zero bias to be very close to the bath temperature, so it is very likely that the increase in temperature is due to the non-equilibrium dynamics of electrons in the vicinity of the molecular bridge or some other vibration activity in the vicinity of the contact. Although the problem concerns all vibration modes of all molecular bridges we measured, this discussion will be focused on Pt-D<sub>2</sub>-Pt and Pt-H<sub>2</sub>-Pt bridges. To analyze the width of the transition, beside the already mentioned OLM, we will use the formula developed by P. Hansma (58) for vibration steps in IETS spectra, which enables the separation of the total width into the terms originating from the temperature, the ac modulation and the rest collected in the term called "natural width".

The step downwards in a  $dI/dV$  curve measured on a molecular bridge happens at a certain voltage applied across the contact because the energy difference between the left and the right moving electrons becomes large enough that elec-

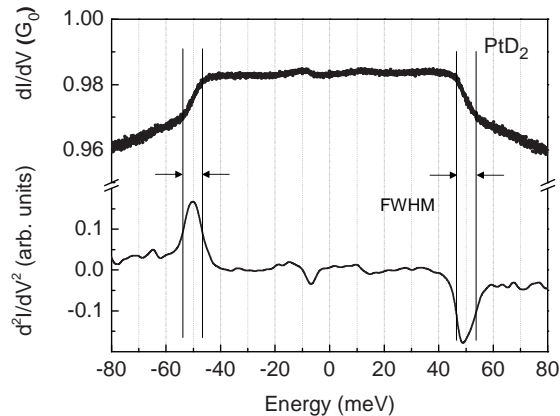


Figure 4.1: Upper and lower curves are  $dI/dV$  (measured) and  $d^2I/dV^2$  (numerical derivative of the  $dI/dV$  curve) as a function of the energy. The peak position in the  $d^2I/dV^2$  curve determines the frequency of vibration excitation and the full width at half maximum (FWHM) of the peak determines the width of the step in the conductance produced by the vibration.

trons from higher energy side (suppose  $+\mathbf{k}$ ) can excite vibrations, loose  $\hbar\omega$  and find unoccupied states on the other side of electron distribution ( $-\mathbf{k}$ ) to relax to. Effectively, this means that electrons are being scattered back and it is seen as a decrease in the conductance as presented in the upper curve in Fig.(4.1).

The lower curve is the numerical derivative of the upper one and it is used to determine the center of the vibration excitation and the width of the vibrationally induced step in the  $dI/dV$  curve. The width is measured at the half maximum of the peak in the  $d^2I/dV^2$  curve and is called FWHM (Full Width at the Half Maximum). In the following paragraphs we would like to answer the question why this width is larger than expected from the thermal broadening and to analyze possible reasons for the widths of transitions measured in our experiments.

## 4.2 Degeneracy of transversal modes

Here we want to give some arguments why we focus our analysis on the longitudinal mode and not on degenerate transversal modes. As shown in the Chapter 2, in the range between -100mV and 100mV  $D_2$  shows five vibration modes (38meV-transversal, 52meV-transversal, 85meV-longitudinal) and  $H_2$  four transversal modes (54meV, 71meV). In both cases transversal modes are theoretically predicted to be degenerate because of the symmetry of the contact. The OLM fits to  $H_2$  data presented in Chapter 2 show the temperature obtained from the transversal modes which is between 12K and 30K. In case of  $D_2$ , the temperature obtained from the fits to the longitudinal mode,

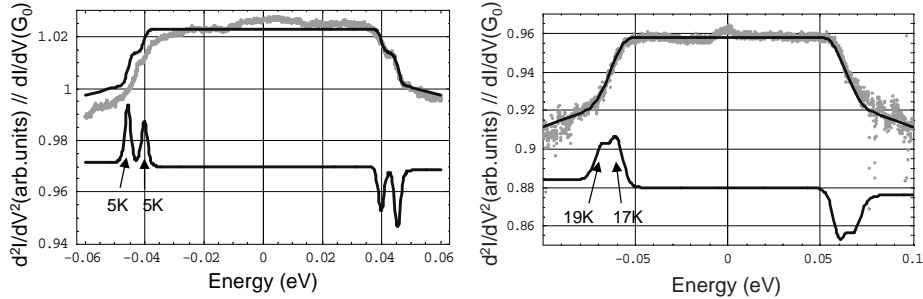


Figure 4.2: *left:  $dI/dV$  curve measured on a  $D_2$  bridge where the two steps correspond to a mode with lifted degeneracy. The temperature obtained here is around 5K for both steps at energies 40meV and 45.6meV. right: An example of a  $dI/dV$  measurement on  $H_2$  where the large width may be partially explained by the overlap of different excitations. The temperatures obtained from the fit are 17K and 19K for vibrations centered at around 60meV and 68meV respectively. The fits have been optimized for the positive bias side.*

as well as for the transversal modes is between 20K and 30K with exception of a few curves where two separate steps could be resolved with temperature of 5K. Fig.(4.2) in the left panel presents a measurement on  $D_2$  with the width of transition steps corresponding to 5K and the right panel is an example of fit to  $H_2$  data with the width of transition step of 30K. If interpreted as a convolution of two vibration signals, the fit gives the temperatures of 17K and 19K. Before proceeding further let us clarify what could be the reason for such large apparent width of the transversal modes and the differences in broadening temperatures of the same vibration mode in different measurements.

We first consider the fact that the transversal modes of  $H_2$  and  $D_2$  are degenerate. They form two branches, the transverse CM mode and hindered rotation mode and each of them is two-dimensional (degenerate in  $xy$  plain) in a contact which is symmetric. In an asymmetric contact the degeneracy will be lifted which leads to a splitting in energy of the modes within the branches and the size of the splitting will depend on the extent of asymmetry of the harmonic potential induced by the asymmetry of the contact. The splitting is expected to be rather small. An example of such a situation is presented in left panel in Fig.(4.2). Only very few measurements gave the temperature of 5K for transversal modes like one presented in the left panel in Fig.(4.2). This is likely due to one degenerate mode with lifted degeneracy such that the energies are separated enough that they can be resolved separately. The fact that we observe a width consistent with the bath temperature in this case is also a good indication that the width of the other steps which gave higher temperatures is not due to some instrumental smearing. The same curve as the one in the right panel of Fig.(4.2) is shown in Chapter 2, where in Fig.(2.5 (c)) only one mode is assumed with the corresponding temperature of 30K. The temperatures obtained from the fit shown in Fig.(4.2(b)) are 17K and 19K if we assume two

vibration excitations centered at around 60meV and 68meV respectively which is attributed to a lifting of the degeneracy of the hindered rotation mode.

Another example of such a  $dI/dV$  curve is shown in Fig.(4.3). Again, the transversal mode is extremely broadened and the temperature obtained from the fit is 40K. This does not look reasonable if compared with the temperature obtained from the fit of the longitudinal mode on the same curve which is higher in energy but still gives lower temperature, 20K. So obviously, one of the reasons for a large width of the transition step can be the uncertainty about the degeneracy of the modes and the mode overlaps. To avoid this our analysis will mainly be based on the longitudinal mode of  $D_2$ . That mode is not degenerate and is far enough from all other modes so the possibility of overlapping can be excluded.

### 4.3 Addition of independent broadening factors

The width of vibrationally induced transitions in  $dI/dV$  curves in IETS was studied in Ref.(58) by P. Hansma. This should also apply to PCS. Here the total measured width (FWHM) of the peak in the second derivative is written as the sum of different terms with different weights:

$$W_{\text{FWHM}} = \sqrt{1.7 \cdot V_m^2 + 5.4 \cdot \left(\frac{kT}{e}\right)^2 + W_{\text{natural}}^2}, \quad (4.1)$$

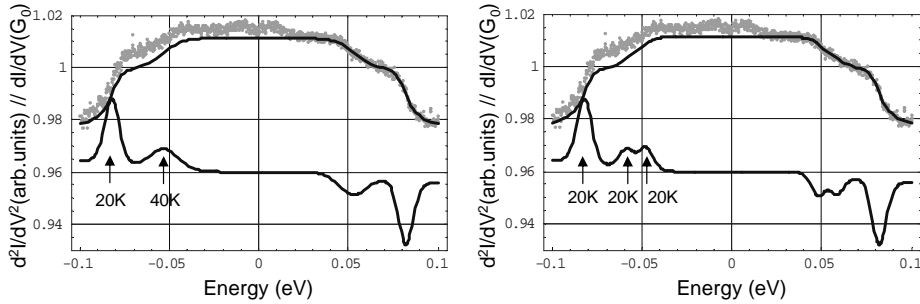


Figure 4.3: An example of a  $dI/dV$  measurement on  $D_2$  where the large width may be partially explained by the overlap of different vibrations. The left panel shows a fit where only one transversal and one longitudinal mode are assumed. The temperature obtained from the fit is 40K for the transversal mode, which is lower in energy and 20K for the longitudinal mode. The right panel shows the fit obtained if two transversal frequencies are assumed. In that case, the temperatures obtained are around 20K for all three vibrations. The frequency in this case lie at 48meV, 55meV and 85meV which would be two nearly degenerate hindered rotation modes and a longitudinal mode. The fits have been optimized to the positive bias side.

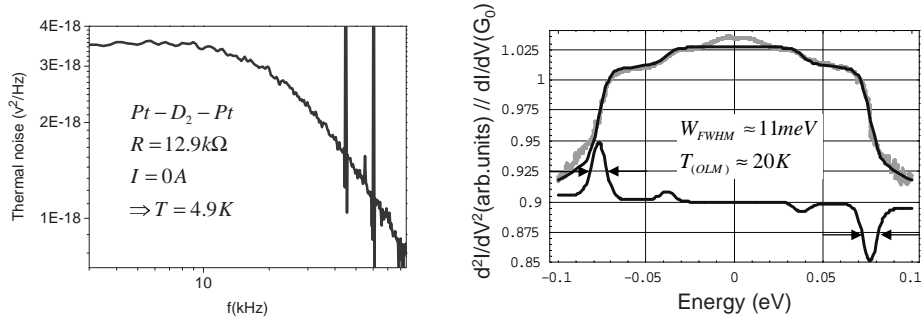


Figure 4.4: *left: Thermal noise power measured on a Pt-D<sub>2</sub>-Pt junction gives the temperature of the electron gas when no bias is applied. The temperature extracted is 4.9K. right: dI/dV curve obtained on the same junction on which the thermal noise presented in the left panel is measured. According to the OLM fit, the temperature of electron gas (when  $V \approx 75\text{mV}$  is applied) is around 20K.*

where  $T$  is the temperature of the electron distribution,  $V_m$  is the rms modulation amplitude and  $W_{\text{natural}}$  is so called "natural width". The FWHM for the curve presented in the right panel in Fig.(4.4) is around 11meV. The modulation amplitude  $V_m=1\text{mV}$  and  $T=4.2\text{K}$  which according to formula (4.1), leads to  $W_{\text{natural}}=10.7\text{meV}$ . From this it is clear that the large width of the transition step is not due to modulation broadening, nor the bath temperature of 4.2K but due to something else hidden in the term  $W_{\text{natural}}$ . Formula (4.1) shows that the temperature of the electron gas plays an important part because of the large weight factor 5.4. An increased temperature of our sample could be due to poor thermal coupling to the helium bath and heat input through the copper leads which are going from the sample to room temperature. This would lead to a broadening in the Fermi-Dirac distribution of electron gas in left and right lead so the broadening in the non-equilibrium distribution function of electrons through the contact. However, this reason for broadening can be entirely excluded as is shown in the left panel in Fig.(4.4) which shows the thermal noise power measured on the same junction on which the dI/dV curve presented in the right panel is taken. The thermal noise curve, taken with no bias across the contact, is consistent with a temperature close to 4.9K which is slightly higher than the expected 4.2K, but still close enough to conclude that it cannot explain the large width of the phonon signal. According to OLM fit, the broadening temperature of electron gas at the conductance step near 75meV is around 20K. About 90% of the curves show a temperature between 20K and 30K.

## 4.4 Discussion

What could be the reason for such a high temperature of the electron gas in our junction? First to consider is a possibility of experimental artifacts. That possi-

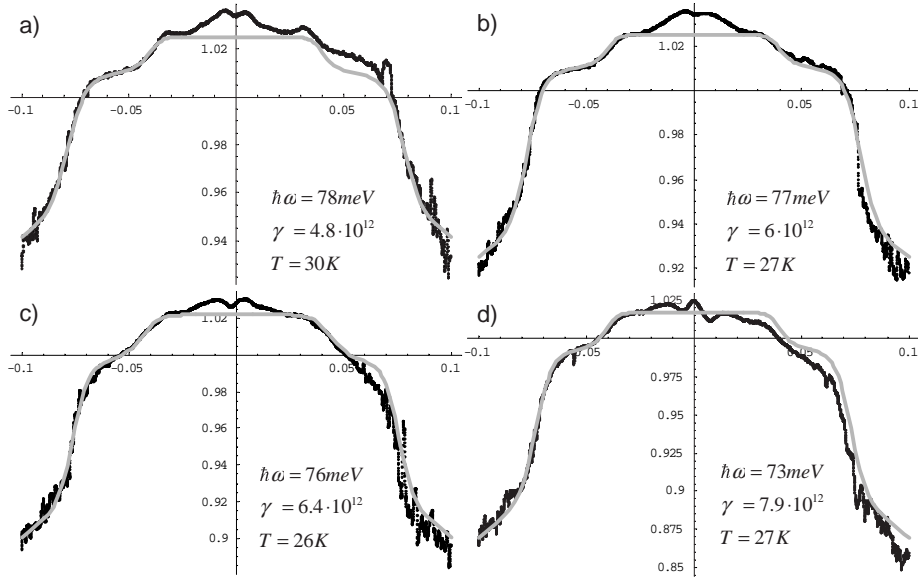


Figure 4.5: *Differential conductance as a function of the voltage for a sequence of four contacts. Starting from the junction on which curve (a) is obtained, every junction is stretched for roughly  $0.1\text{\AA}$ . The fits obtained by OLM model are optimized for the negative bias. A decreasing tendency in frequency is observed as expected for the  $D_2$  longitudinal mode. The electron-vibration coupling  $\gamma$  shows increasing tendency upon stretching while the temperature remains nearly unchanged.*

bility can be excluded since we have some curves which gave the correct temperature and experiments are performed on the same setup, under the same experimental conditions so the broadening is very likely to be due to some physical phenomena. An attempt to correlate the temperature extracted from the OLM fits is presented in Fig.(4.5). The fits are obtained for the contact which was kept unbroken but stretched for fixed amounts before the next curve is taken. From the fitting parameters obtained by the OLM, the decreasing tendency of vibration frequency and increasing tendency of electron-vibration coupling is evident while the temperature remains mainly unaffected. Table(4.1) presents the vibration frequency, electron-vibration coupling  $\gamma$  and temperature for a set of randomly chosen contacts where a large part of the longitudinal frequency domain is covered. The different junctions also show different electron-vibration coupling strengths but no systematic correlation between the temperature and either of the other two parameters.

So what could be the reason for the observed temperature broadening? If we take the energy of the electrons at 50meV and redistribute the energy over other electrons, in order to arrive at 20K we need only  $\sim 25$  other electrons. This estimate suggests that, if the broadening is due to a genuine heating of the electron

$\hbar\omega(meV)$	$\gamma \cdot 10^{12}(meV)$	T(K)
71	5	30
76	5	23
76.5	6.5	20
80	3	40
82	1.58	20
77	2.5	27
79	2	20
83	2.5	40
100	0.8	30

Table 4.1: Vibration frequency  $\hbar\omega$ , vibration-electron coupling  $\gamma$  and temperature T obtained from fitting by the OLM on the longitudinal mode in a selection of dI/dV curves for Pt-D<sub>2</sub>-Pt junctions.

gas, the mean free path would have to be as short as  $\sim 1$ nm. Experiments and theory point out much larger values ( $>200$ nm) for our system (59).

An interesting observation which suggests that the large width of vibration steps could be due to an increased electron temperature in the junction was reported by Downes *et al.* (60). In an STM experiment, they form atomic-size metal junctions and measured electron temperatures up to 9000K at 2V bias which they obtain from the spectrum of photon-emission from the contact. Although the applied bias in our experiment is much smaller (typically less than 100mV) and the contact is quasi-ballistic with a single almost entirely transparent channel, the possibility of anomalously high electron temperatures needs to be studied further.

A possible reason for the apparent broadening could be in the other hydrogen molecules adsorbed in the vicinity of the contact. It is expected that many hydrogen molecules are adsorbed on Pt leads. By exciting a mode of the molecule which is in the junction, the other molecules bound to the surfaces might get excited as well since they have the same mass and depending on binding to the surface, possibly similar vibration frequencies. This would effectively lead to the broadening of the vibration signal since it will provide a means for vibration mode relaxation. Evidence against this scenario is coming from the OLM which gives good fits only when we assume that external damping is zero, which means that vibrations relax only through the vibration-electron interaction and not through the other oscillations of the lattice atoms or molecules on the surface. A possibility which is not excluded is that some Two Level Fluctuations (TLF) in the vicinity of the contact are excited by electrons. The heating of the lattice is observed indirectly through the fact that most of the contacts become unstable (very noisy but without breaking) at voltages above 100mV. The fact that the contact is unstable but does not break suggests that the heating occurs in the leads. Hydrogen can be cleaned from the contact at biases around 300mV which is due to heating of the molecule. In the spectroscopy window

the excitation of TLF's may then give rise to an effective broadening of the vibration mode signal due to a modulation they induce in the vibration mode energy. This can be viewed as inhomogeneous broadening of a single molecule<sup>1</sup>.

An interesting approach has been proposed by Di Ventra and coworkers (61; 62; 63). They predict the heating of conduction electrons due to friction with the rest of the Fermi gas. They assume that the electron liquid has a viscous nature and the electrons shooting through the junction will dissipate the energy in the vicinity of the contact and heat it in that way. This model is still under discussion but when we use the parameters of the experiment the effective temperature this model predicts comes very close to the observed temperatures.

## 4.5 Conclusions

The width of the conductance step induced by electron-vibration scattering in differential conductance measurements on H<sub>2</sub> (but also the other molecules not presented here) shows a width larger than expected at liquid He temperature. In our experiments we did not find any systematic dependence of the broadening as a function of stretching of the contact or electron-vibration coupling. The various possible mechanisms which could lead to the broadening are discussed. Most possibilities presented above can be probably excluded based on the fact that the temperatures observed vary and sometimes are very close to the actual bath temperature. The mechanism that is the most likely candidate to explain these observations is the inhomogeneous broadening mechanism due to excitation of TLF's. The actual broadening observed would then indeed strongly depend on the coverage of the Pt leads by H<sub>2</sub> molecules near the junctions.

---

<sup>1</sup>We thank Prof. A. Nitzan for this suggestion.

## Chapter 5

# Single-molecule junctions for CO

This work is performed in collaboration with M. Suty, M. Strange and K. Jacobsen.

### 5.1 Motivation

Since our approach to the problem of conductance through the molecules is from the simple to more complicated ones, after successful interpretation of the measurements for  $\text{H}_2$ , we moved to a slightly more complicated junction, a Pt-CO-Pt bridge. A hydrogen molecule has only two  $s$  electrons which combine into one bonding ( $\sigma$ ) and one antibonding ( $\sigma^*$ ) state. With CO, the configuration of molecular orbitals is more complicated. Oxygen, with electronic configuration ( $1s^2, 2s^2 2p^4$ ) and carbon ( $1s^2, 2s^2 2p^2$ ) make CO with ten valence electrons which occupy five molecular orbitals. The lowest in energy is the bonding  $\sigma_s$ , then the antibonding  $\sigma_s^*$  followed by a pair of  $\pi$  bonding orbitals constructed from C and O  $p_x$  and  $p_y$  orbitals. The HOMO is  $\sigma_p$  constructed from the atomic  $p_z$  orbitals. Two antibonding  $\pi^*$  orbitals made from the atomic  $p_x$  and  $p_y$  orbitals create the LUMO. Since the oxygen electron orbitals are slightly lower in energy than C (O is more electronegative), there is a small charge transfer towards the O atom. From surface chemistry it is known that CO binds to flat surfaces of transition metals, so we expect that it will bind to our Pt point contact, although it is an arrangement with a lower coordination number. We will explore the vibration modes of this structure, their dependance on stretching and eventually try to give a possible interpretation of the measured properties. Unlike the experiments with hydrogen, in this experiment we can not easily use isotope substitution because the introduced mass difference will be small.

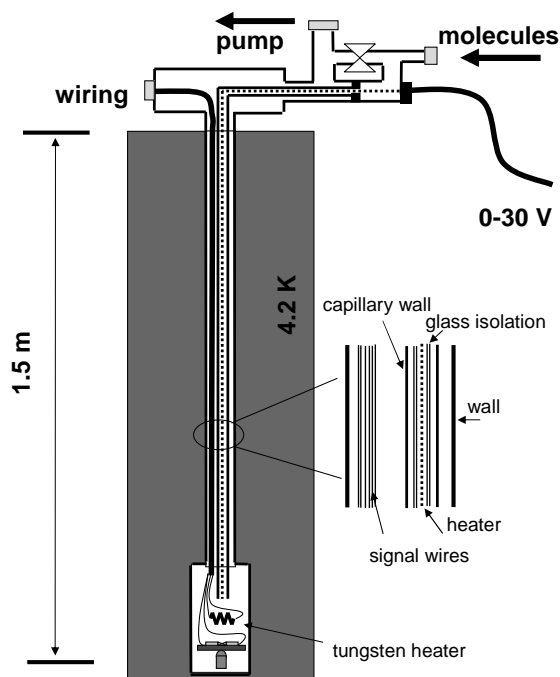


Figure 5.1: The schematic drawing of the dipstick and the tubing system used to inject the CO gas. The dashed line is the heater (Kanthal wire) isolated by a glass tube and placed inside a stainless steel capillary which runs down to the sample. Close to the sample is a small tungsten heater.

## 5.2 Technical aspects

A junction of a single CO molecule is more complicated from chemical point of view, but also from the technical aspects. Namely, CO gas freezes at 84K and to reach the sample chamber it has to travel through a meter and a half long tiny capillary, cooled down to 4.2K. To prevent freezing, the capillary is equipped with a heater placed in a tiny glass tube which serves as electrical isolation between the heater and the metal capillary walls since the heater wire is not covered with any electrical isolation to prevent outgassing of the organic isolation material. A schematic drawing is presented in Fig.(5.1).

A glass tube is also used as the electrical isolation in order to be able to bake out the capillary to remove possible contaminations unavoidably present on it. Ideally, one would like to use a double wall capillary with the heater in the vacuum in between two walls, which we developed and applied in later experiments. In the present experiments we used a Kanthal wire heater with a resistance of about  $200\Omega$ . The whole system, including the capillary with the hot heater (current through the heater was around  $I=100\text{mA}$ ) is pumped to around  $2 * 10^{-5}\text{mBar}$  at room temperature for about 10 hours or more. After

that, the chamber is flushed a few times with CO through the capillary from the bottle which will be used in the experiment. The system is pumped again before cooling to 4.2K. After a few hours in liquid He, the capillary is heated again and shortly flushed with CO before the heater is switched off. All this is done before the wire is broken. The idea is that the capillary will quickly cool down below 84K and CO will condense on the walls. By heating the walls again, the CO will start degassing and move along the capillary down to the sample. The other way to deposit CO molecules in the junction is to deposit them first on a small cold tungsten heater placed close to the junction (Fig.(5.1)), before the junction is broken for the first time. The heater is cleaned by heating and cooling cycles when everything is cold and the wire intact. The molecules are evaporated from the tungsten heater into the junction by applying short high-current pulses. The usual waiting time before the conductance histogram starts showing the presence of CO is a few minutes if the first approach is used. If the molecules are deposited using the tungsten heater, they appear in the contact immediately. The whole described procedure is made carefully and repeated strictly each time the experiment is performed in order to minimize the possibility of contamination. The metal used in the MCBJ device to contact a single CO molecule was platinum.

## 5.3 DC measurements on Pt-CO-Pt junctions

### 5.3.1 Conductance histograms

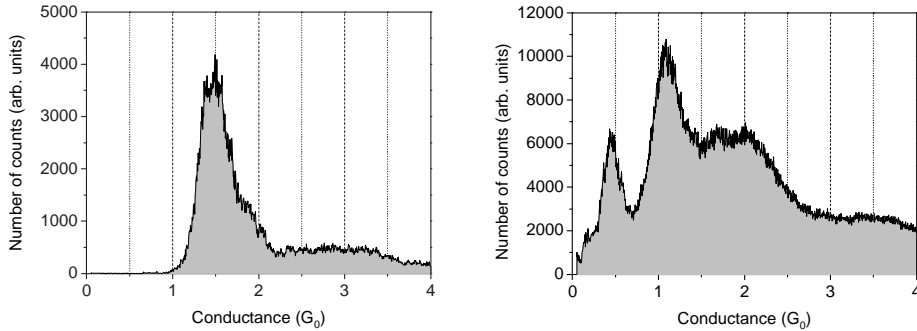


Figure 5.2: *Left: Conductance histogram for a clean Pt contact at 4.2K shows that there is no contamination present in the junction. Right: Conductance histogram after the CO was added in the sample chamber through the heated capillary. Both measurements are taken at a dc bias of 100mV.*

The dc measurements involve breaking traces and conductance histograms constructed from the breaking traces. Each measurement session starts with measurements on clean Pt to be sure that there is no contamination due to some residual gas condensate on it. After we obtain a clean Pt histogram,

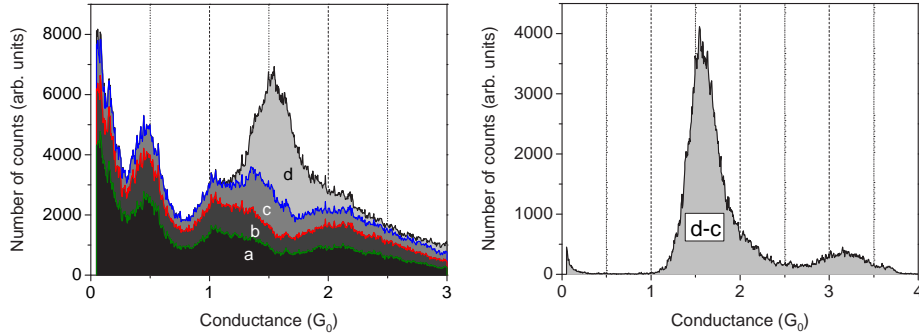


Figure 5.3: In the left figure are shown consecutive conductance histograms marked with (a,b,c,d) where b) contains about two hundred breaking traces more than a) and so on. The figure on the right shows a clean Pt histogram which is obtained when counts from histogram c are subtracted from the histogram d.

presented in Fig.(5.2(left)), we slowly increase the current through the capillary heater while continuously breaking and making the contact. The maximum heater current to clean the heater at room temperature while pumping the insert down is about 100mA. When introducing the molecules into the chamber the heater current was slowly increased and the presence of the molecules in the sample is usually registered for heater currents between 50mA and 70mA. The conductance of the sample is monitored in the form of a conductance histogram and the presence of CO in the contact is registered by the changing of the Pt conductance histogram with a peak at  $1.5G_0$  into one with peaks close to  $0.5$  and  $1G_0$ . The final histogram in presence of CO is presented in Fig.(5.2 (right)).

The clear difference from the  $H_2$  experiment can already be seen in the behavior of the histogram as the bias is increased. At a bias around 300mV the histogram changes into a histogram of clean Pt which means that the heating became large enough that the thermal excitations overruled the bonding energy, resulting in evaporation of CO molecules from the junction. But while in the case of  $H_2$  a molecule will jump in the contact as soon as the bias is lowered CO does not necessarily do the same. Usually the histogram changes to a clean Pt histogram and the procedure of introducing the molecules has to be repeated to restore the CO presence. We assume that this is due to the limited mobility of the molecules at the surface at 4.2K. Sometimes we observe a transition between building up of the peaks characteristic for Pt with CO ( $0.5G_0$  and  $1G_0$ ) and the peak characteristic for the clean Pt ( $1.5G_0$ ). Fig.(5.3) presents such a situation where after a few hundred of breaking and making events which showed CO presence in the junction the peaks at  $0.5$  and  $1G_0$  stopped building up and the Pt peak emerged, as shown in Fig.(5.3(right)). This suggests that the number of molecules close to the junction is very small and very likely only one particular molecule is contributing in the action for quite a long time, a few hundreds of breaking cycles. Once this molecule gets trapped at a site away from the

atomic contact during the breaking and indentation cycles we recover a clean Pt histogram.

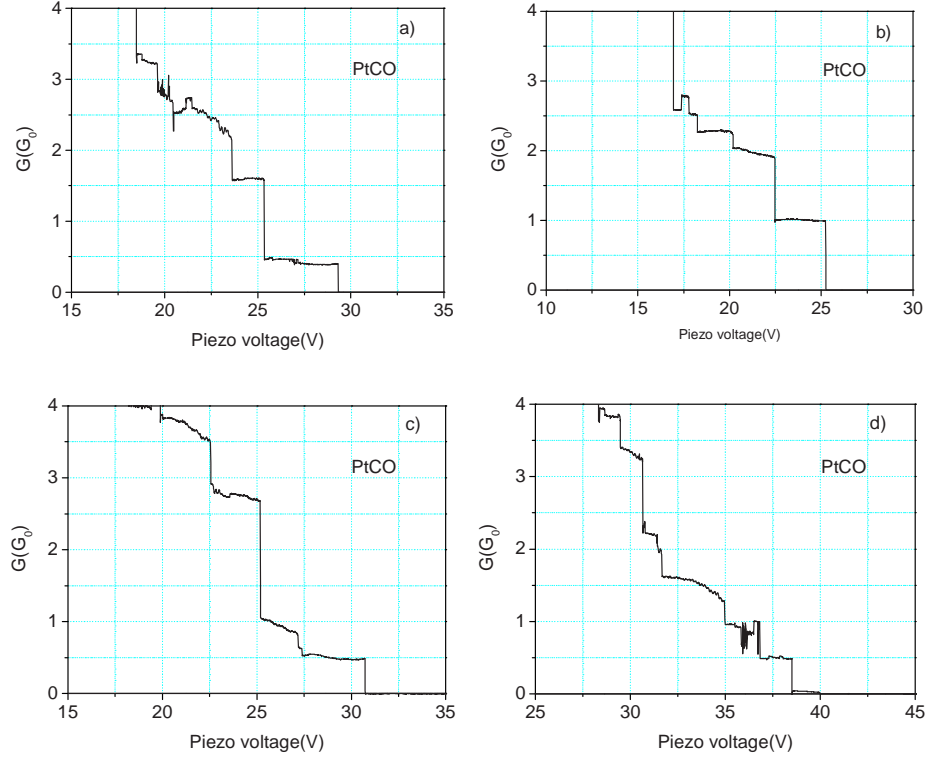


Figure 5.4: *Conductance as a function of the piezo voltage. A remarkable difference between the traces presented in the figures a, b, c and d is in the combination and order in which the plateaux appear. Conductance can skip one of the plateaux, like in a and b, but it never jumps from the lower to the higher conductance value.*

### 5.3.2 Breaking traces

Looking at the conductance traces from which the conductance histograms are made, one can make a general selection depending on the plateaux present on them. Typical representatives of each category are shown in Fig.(5.4). Comparing the histograms for clean Pt and Pt with CO, the striking difference is in the region where the clean Pt histogram does not have any pronounced features, below about  $1.5G_0$ . That is also justified by breaking trace analysis. Looking at the breaking traces presented in Fig.(5.4), before reaching a stable value at  $1G_0$  or  $0.5G_0$ , the conductance has values between  $1.5G_0$  and  $2G_0$ . This can be due to a Pt-Pt contact which still can be affected by the presence of CO. Those con-

ductance values and possible configurations responsible for the values above  $1G_0$  will not be considered here. From those higher values the conductance jumps to a plateau close to  $1G_0$  or  $0.5G_0$  and then it breaks. A remarkable difference between the different breaking traces is that a conductance trace can take either a  $1G_0$  or  $0.5G_0$  value, or  $1G_0$  and then  $0.5G_0$ . Looking at the relative length of the plateaux presented at in Fig.(5.4), one notices that they are either equal in length or the one at  $0.5G_0$  is longer than one at  $1G_0$ . Another characteristic of the conductance evolution upon breaking is that the conductance never jumps from the lower to the higher value.

## 5.4 Model calculations

Extensive first-principles calculations investigating the contact geometries, corresponding conductances and vibration properties were done by Strange, Thygesen and Jacobsen (64; 65). By diagonalizing the local electronic structure Hamiltonian within a Wannier functions (WF) basis set localized at the CO molecule, they obtained seven renormalized energy levels of CO including the influence of the Pt leads for any orientation considered. In their calculations, Strange *et al.* focus on the perpendicular and the tilted bridge configuration and they find that ten CO valence electrons occupy five low lying renormalized energy levels, leaving two unoccupied. Five occupied renormalized levels represent the five lowest molecular orbitals with  $2\sigma$  (bonding) being the HOMO. Two empty ones are two  $2\pi^*$  orbitals (antibonding). According to the calculation, these two  $2\pi^*$  orbitals ( $|a\rangle$  and  $|b\rangle$ ) are actually the only molecular orbitals which significantly contribute to the conductance. Each of them forms one transmission channel and the transport is analyzed through each of them separately by introducing the group orbitals  $|g_\alpha^a\rangle$ . This represents the group of states  $|g_\alpha^a\rangle$  in lead  $\alpha$  to which  $|a\rangle$  is coupled, so any state in the lead orthogonal to  $|g_\alpha^a\rangle$  does not couple to  $|a\rangle$ . The coupling between the molecular orbital  $|a\rangle$  and the group orbital  $|g_\alpha^a\rangle$  is  $V_{\alpha,a} = \langle a|H|g_\alpha^a\rangle$  where  $H$  is the Hamiltonian. Thus, in the case of asymmetric coupling to the left and right, the transmission will be mostly determined by the weaker coupling side. Strange *et al.* obtain the transmission  $T$  for two molecule positions as function of the energy, presented in Fig.(5.5(right)). Curve A applies to a Pt-CO-Pt junction where the CO molecule is oriented perpendicular to the Pt-Pt axis with the carbon end bonded symmetrically to both Pt atoms. Configuration B is obtained by stretching A which results in a tilting of the molecule towards a more aligned configuration. Both orientations have a peak in the transmission at the Fermi energy. Assuming that, in the case of the tilted bridge configuration, the CO molecule binds to the left with the C and to the right with the O side, they get the couplings  $V_{R,a}^2 \ll V_{L,a}^2$  meaning that C binds much stronger. The analytical expression for the transmission function in that case is

$$T(\epsilon) = 4\pi^2 V_{R,a}^2 \rho_{R,a}^0(\epsilon) \rho_a(\epsilon). \quad (5.1)$$

where  $\rho_a(\epsilon)$  is the projected density of states (PDOS) of  $|a\rangle$  and  $\rho_{R,a}^0(\epsilon)$  is PDOS of the right lead group orbital in the absence of coupling to  $|a\rangle$ . In the left panel

of Fig.(5.5) is presented the PDOS for both molecular orbitals ( $|a\rangle$  and  $|b\rangle$ ) and for the group orbitals in right lead which makes the contact with oxygen. From the picture it can be concluded that the PDOS of the group orbital in the right lead is the one which gives rise to the peak in the conductance near the Fermi energy, so the conductance is due to the high PDOS of the  $d$ -states of the Pt contact. Fig.(5.6) presents the evolution of the contact during breaking according to the calculations. Starting from the upright positioned molecule on the Pt point contact, with the C side to the Pt, it slides into the contact upon pulling. The conductance is constantly decreasing until the moment when the molecule jumps in the tilted bridge configuration. This jump is also followed by a jump in the conductance. The energy of the tilted bridge configuration, according to this calculation, has a local minimum which makes it stable and results in a conductance plateau.

## 5.5 Discussion of the conductance for CO

In this section we will try to find a possible interpretation for the measurements and compare it with the theoretical predictions. The conductance histograms show two peaks corresponding to frequently occurring plateaux in the breaking traces. Plateaux above  $1G_0$  in Fig.(5.4) are believed to be due to the last Pt-Pt contact which also can be influenced by the presence of CO, or CO bridging the Pt-Pt contact in a certain orientation but we will focus of our attention on the peaks at 1 and  $0.5G_0$  since they are genuinely new features which were not present in the contact before injecting the molecules and because higher conductance plateaux can be attributed to many possible configurations. Plateaux at 1 and  $0.5G_0$  suggest that during the breaking process, due to the presence

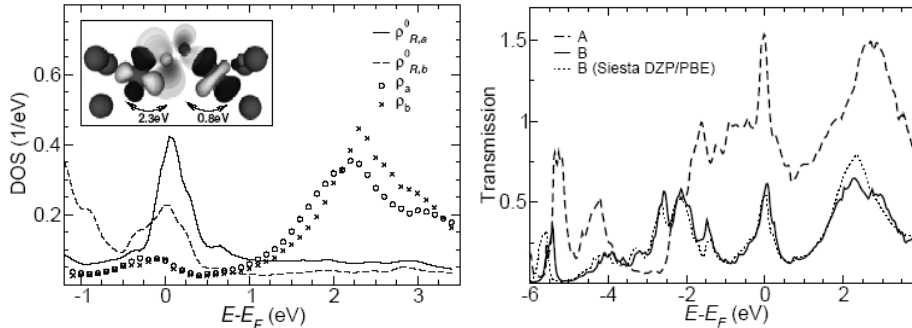


Figure 5.5: *left: The PDOS of the molecular orbitals  $|a\rangle$  and  $|b\rangle$  and the PDOS of the group orbitals in the weakly coupled lead. The inset presents the molecular orbital  $|a\rangle$  and its corresponding group orbitals in the left and the right lead. right: Transmission function for the upright bridge (A) and the tilted bridge (B). The dotted line is the result obtained with different code (Siesta-DZP/PBE) for the tilted bridge configuration. After Ref. (64).*

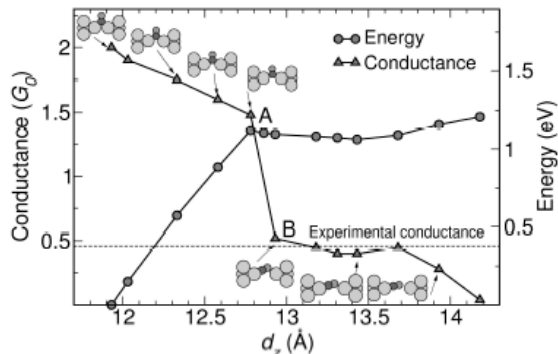


Figure 5.6: *Conductance and total energy as a function of electrode displacement  $d_z$ . The upright bridge configuration is the one with higher conductance while for the tilted bridge configuration it is lower. The change from one configuration to another is accompanied by an abrupt change in conductance. After Ref. (64).*

of the molecule, two new configurations with specific conductance appear. At this point, based on the experience with hydrogen where the presence of the molecule in the junction has been extensively verified, we can conclude that  $1G_0$  and  $0.5G_0$  steps are due to a molecule. The fact that the  $1G_0$  and  $0.5G_0$  plateaux disappear at higher biases and very seldom reappear unless the deposition procedure is repeated, suggests that the molecule is much less mobile on the surface than the hydrogen molecule, as one would expect for CO. Below we will show further evidence that it is indeed a molecule by measuring vibration spectra on the plateau at  $1G_0$  with energies much different from the ones for metals.

Investigating the breaking traces like the ones shown in Fig.(5.4), we conclude that the plateaux occur entirely uncorrelated to each other. Both plateaux can appear in the same breaking trace, but it also very often happens that only one of them occurs. The only observed correlation is that if both plateaux are present in a same breaking trace the one at  $0.5G_0$  always occurs after the one at  $1G_0$ . Since the contact is being pulled apart the distance between two electrodes is increasing and if the molecule is responding to that distance increase by changing its orientation, the later orientation is likely to be the longer one. In that case  $1G_0$  will be due to the first position and  $0.5G_0$  due to the second. A possible scenario where the molecular motion between the tips evolves from a short orientation to a more elongated one is presented by the breaking trace in Fig.(5.6) obtained in numerical calculations (64). In the calculation, the tilted bridge configuration produces a plateau with a conductance of  $0.5G_0$  which could correspond to the plateau at  $0.5G_0$  which we measured. A clear mismatch between the calculated and measured breaking traces is in the region close to  $1G_0$ . In the conductance histograms the height of the peak at  $1G_0$  is even higher than the one at  $0.5G_0$ , which means that the structure producing the  $1G_0$  peak should be, at least, equally frequently happening as the  $0.5G_0$  one. This is

also clear from the measured breaking traces. In the calculated curve a plateau at  $1G_0$  is entirely missing and closest to it is the structure produced by the molecule positioned upright with the conductance decreasing from  $2G_0$  to  $1.5G_0$  upon stretching. Even that orientation does not produce a flat plateau, but rather a steep slope. Also the rupture of the  $0.5G_0$  configuration in experiment is usually followed by a sharp step down to a value below  $0.1G_0$ , while the calculated conductance decreases slowly<sup>1</sup>. The starting upright position of the molecule in the point contact, with the C atom bridging to Pt, is supported by observations of CO behavior on flat surfaces.

Figure (5.5(right)) presents the calculated transmission of the Pt-CO-Pt bridge for the molecule positioned in upright (A) and the tilted bridge (B) configuration. In both cases, the transmission around the Fermi level has a strong, very narrow peak which results in very strong energy dependence of the transmission of the contact. From the experimental point of view, having only the dc conductance measurements in mind, that would result in a strong dependence of the peaks in conductance histograms upon the applied bias which is not observed.

## 5.6 Point contact spectroscopy on Pt-CO-Pt junctions

Having the the hydrogen experiments in mind we would like to use Point Contact Spectroscopy (PCS) to investigate the configuration which gives rise to the  $1G_0$  peak. To be able to use the PCS method it is a great advantage to have an entirely transparent contact<sup>2</sup>, so for that reason it can be successfully performed mainly for contacts with  $G \simeq 1G_0$ , arising from one dominant transmission channel with the transmission coefficient close to one ( $\tau \simeq 1$ ). If the conductance has a value of  $1G_0$  and this is due to more than one partially transmitting channels PCS is not likely to be observable since a small decrease in conductance ( $1 - 3\%$ ) due to electron-vibration interaction would be lost in the large conductance fluctuations arising from the interference between coherent, partially transmitted and partially multiply reflected electron wave functions.

In the case that a conductance of  $1G_0$  originates from one channel with  $\tau \simeq 1$ , we should be able to excite the vibrations of the structure and observe the resulting drop in conductance. The Pt bulk phonons are peaked at the Debye energy of around  $12.8\text{meV}$  (66), so any vibrational feature above that value should be due to molecular vibration excitations. Features below  $15\text{meV}$  which often appear in our  $dI/dV$  curves we will disregard assigning them to phonons originating from the Pt leads.

Concerning the plateau close to  $0.5G_0$  we have investigated the possibility that it is due to one completely opened channel, but with lifted spin degeneracy. In that case the conductance fluctuations will still be suppressed since

<sup>1</sup>This could also be an artifact due to a small number of atoms which are allowed to relax.

<sup>2</sup>see chapter 1

the channel is still entirely transparent for one spin orientation while completely closed for the other. However, all our attempts gave just large conductance fluctuations as one should expect in the case of contact with partially transparent channels.

## 5.7 Experimental results

The setup used for these measurements is the same one as described in Chapters 1 and 2. A selection of the measured differential conductance curves is presented in Fig.(5.7). The fits through the experimental data are obtained by the OLM introduced earlier in Chapter 1. The fitting parameters in this model are the zero bias conductance, the electron-hole damping rate  $\gamma_{e-h}$  which can also be seen as the electron-phonon coupling coefficient, the temperature and the excitation frequency. The zero bias conductance is very precisely measured in the experiment and the vibration frequency is also obtained from the second derivative curve, where the temperature of the electron gas in the contact does not need to be the same as the temperature of the thermal bath and the electron hole damping rate  $\gamma_{e-h}$  describes the height of the conductance step and the slope that follows it.

The width of the peaks in the second derivative curves presents the width of the phonon step in  $dI/dV$  and in this model is associated with the temperature. Fig.(5.7(i)) presents a measurement with two clearly pronounced steps around 31meV and 55meV. The curve (a) is a fit to the positive bias side where it is assumed that only one vibration mode is excited. Obviously, it does not fit the data in the higher energies where another step appears, but fit (b) is satisfactory. The fitting parameters are:

$$\begin{aligned} \{\hbar\omega_1 = 33meV; T_1 = 12K; \gamma_{e-h,1} = 0.35 \cdot 10^{12}s^{-1}\}, \\ \{\hbar\omega_2 = 54.5meV; T_2 = 32K; \gamma_{e-h,2} = 1 \cdot 10^{12}s^{-1}\}. \end{aligned} \quad (5.2)$$

The sharp edge of the first vibration step which results also in a small peak in the first derivative near  $\omega_1$  is attributed to vTLF and will be discussed in Chapter 7. The data curves presented in all figures are not completely symmetric. The reason for this can be a deviation from symmetric coupling to the left and right lead or a residual conductance fluctuation background. Since there is also a small asymmetry due to known instrumental reasons we fit only one side of the curve<sup>3</sup>.

Figure (5.7(ii)) has a signature of three vibration modes. The fit is obtained on the negative voltage side and curves (a) and (b) are the fits assuming one and two vibration excitations, clearly showing that the third vibration mode

---

<sup>3</sup>One known reason of instrumental nature that affects only one side of the curve results when the bias is ramped from +100mV to -100mV. It is noticed that a small hump is added at the beginning, close to 100mV and it is known to be due to time constant of the lock-in. When sweeping the bias in the opposite direction, the same happens close to +100mV, on the sample as well as on a test resistor.

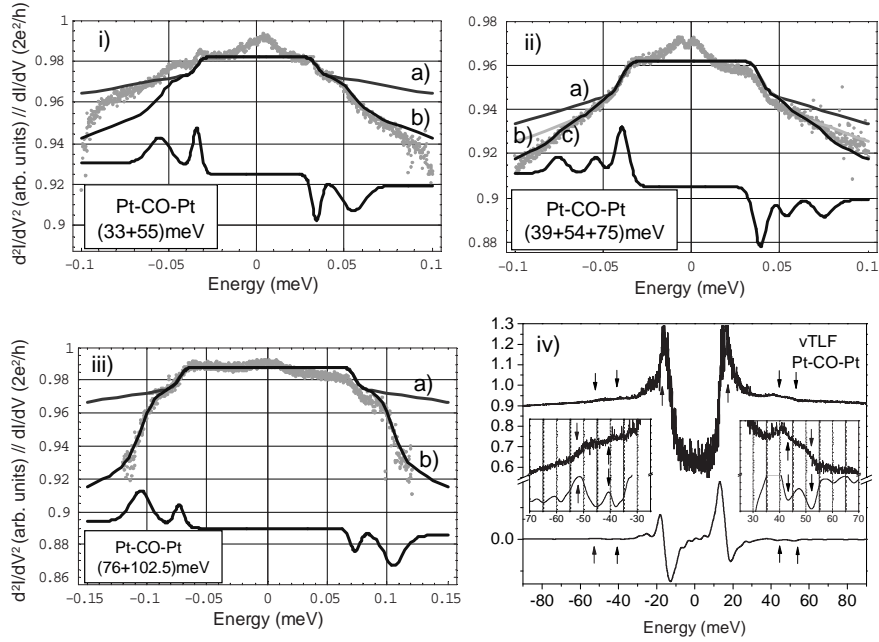


Figure 5.7: Differential conductance (dots) as a function of the voltage. The different fits to the experimental curves are done using the One Level Model introduced in Chapter 1 and the lower curves are  $d^2I/dV^2$  curves obtained from the OLM (except for figure iv)). The clear necessity to include several excitation modes is shown in the fits marked with letters (discussed further in the text). The frequencies of the excitation modes are indicated by the peaks in the  $d^2I/dV^2$  curves and in figure iv) by additional arrows. The step height in different curves is significantly different which suggests that there is strong variation in coupling strength. In panel iv), beside the excitations that will be identified below as  $40 \pm 2 \text{meV}$  and  $52 \pm 3 \text{meV}$  modes, the curve shows a mode at  $22 \pm 3 \text{meV}$  as well, never observed in a regular PCS spectrum but always as a vTLF. The insets on left and right in figure iv) are enlarged areas where the regular PCS excitations are visible.

should be active as well. The fitting parameters are:

$$\begin{aligned}
 &\{\hbar\omega_1 = 39 \text{meV}; T_1 = 18 \text{K}; \gamma_{e-h,1} = 0.75 \cdot 10^{12} \text{s}^{-1}\}, \\
 &\{\hbar\omega_2 = 54 \text{meV}; T_2 = 20 \text{K}; \gamma_{e-h,2} = 0.4 \cdot 10^{12} \text{s}^{-1}\}, \\
 &\{\hbar\omega_3 = 75 \text{meV}; T_3 = 25 \text{K}; \gamma_{e-h,3} = 0.65 \cdot 10^{12} \text{s}^{-1}\}.
 \end{aligned} \tag{5.3}$$

Figure (5.7(iii)) shows a clear presence of two vibration modes, introducing a new excitation which will be classified as the  $110 \pm 12 \text{meV}$  mode. The fitting

parameters are:

$$\begin{aligned} &\{\hbar\omega_1 = 76\text{meV}; T_1 = 10\text{K}; \gamma_{e-h,1} = 0.95 \cdot 10^{12}\text{s}^{-1}\}, \\ &\{\hbar\omega_2 = 102.5\text{meV}; T_2 = 32\text{K}; \gamma_{e-h,2} = 5 \cdot 10^{12}\text{s}^{-1}\}. \end{aligned} \quad (5.4)$$

Figure (5.7(*iv*)) introduces the lowest excitation mode observed in spectroscopic measurements on Pt-CO-Pt bridge. This mode could not be recognized as a regular PCS feature, but only as a vTLF like the one presented in this figure. A possible reason for this is the fact that it is positioned close to the region where a strong signal from the metal phonons is dominant which makes it difficult to distinguish as a regular PCS signal. In the same curve excitations around 42meV and 52meV are present, which can be seen in the left and right insets.

Based on the analysis of the curves presented in Fig.(5.7), but also other curves from about ten measurement series (around 300 curves) not presented here, we conclude that no evidence of any correlation between the appearance of different excitation modes is found. All vibration modes have been observed in combination with any of the other modes. Single excitations are also observed very frequently.

All data collected together are presented in the form of a histogram in Fig.(5.8). The peaks in the histogram constructed from many values collected from individual curves coincide with the excitation frequencies introduced in Fig.(5.7).

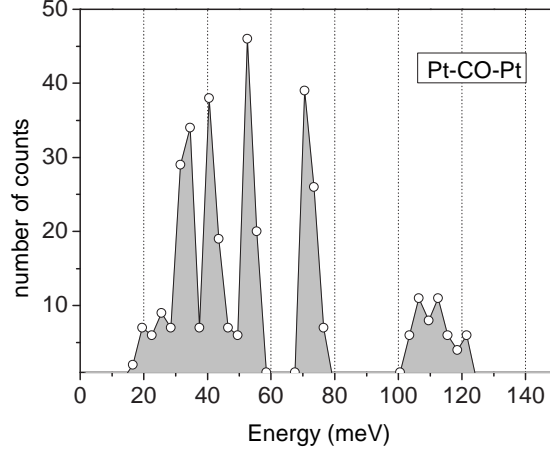


Figure 5.8: *Distribution of vibration frequencies of a Pt-CO-Pt bridge observed in PCS. In this distribution are included data from regular PCS measurements and vTLF which appears only in the mode around 20meV.*

## 5.8 Stretching dependence

Similar to the case of hydrogen, stretching the contact bridged by a molecule means stretching the Pt-molecule bond. Since the strength of the Pt-molecule

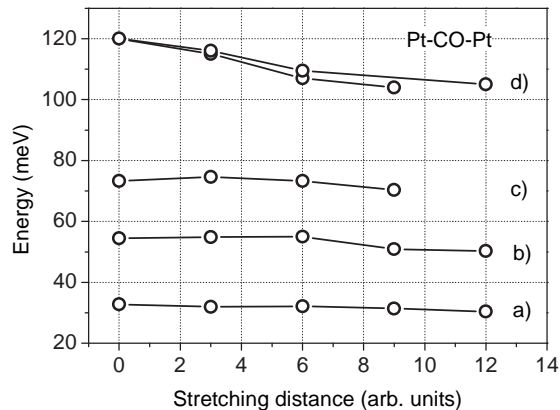


Figure 5.9: Frequencies of some vibration modes as a function of the contact stretching, measured in experiment. The curve marked d) is obtained by relaxing an already stretched contact and stretching it again. Since the different curves are obtained from different measurement runs, the calibration of the horizontal axis is not exactly the same. One stretching unit is estimated to be  $(0.05 \pm 0.005) \text{ \AA}$ .

bond depends on the overlap of the molecular orbitals with Pt electron orbitals, pulling them apart reduces the coupling strength and so decreases the spring constant which decreases the vibration frequency, since  $\omega \sim \sqrt{k}$ . The second effect is the increase of the transversal frequency due to increase in the restitutive force. While the longitudinal modes are affected only by the first effect, the transversal suffer from both. Thus a longitudinal mode can only decrease upon stretching while a transversal mode can do both, increase or decrease, depending on the nature of metal-molecule bond. Fig.(5.9) presents the experimentally observed stretching dependence of some vibration modes for the Pt-CO-Pt bridge. As a general conclusion, the vibration modes of a Pt-CO-Pt bridge are changing very little with stretching over the given range. The only mode which experiences a significant change is the one around 112meV, which strongly decreases.

## 5.9 Model calculations of vibration modes

Performing model calculations of the vibration properties of a Pt-CO-Pt bridge, Strange *et al.* explored a large variety of different configurations (65). In Fig.(5.10) are presented the vibration frequencies for the different systems which were investigated. The calculated frequencies for a CO molecule bound to a Pt

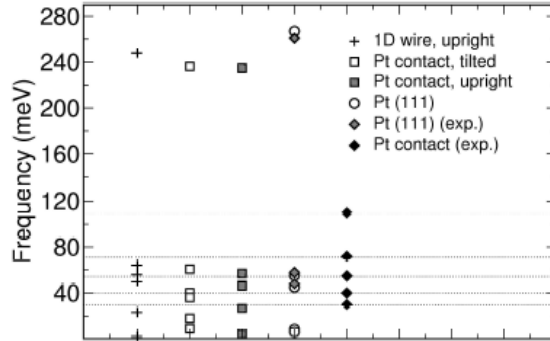


Figure 5.10: Numerically obtained vibrational frequencies for different structures of Pt with CO: CO in upright position in between 1D Pt leads (pluses), CO in Pt contacts (squares and shaded squares), CO on Pt (111) surface (circles), experimental results for CO on Pt (111) surface (shaded diamonds) and the experimental results for CO in Pt leads presented in this chapter. After ref. (65)

(111) surface are in very good agreement with the experimentally measured values. This illustrates the level of agreement that should be expected. The configurations interesting for us are the ones marked with the squares since they are expected to apply for our system.

In both cases, the upright and the tilted bridge configuration, the number of vibration modes is six. The conductance of the contact in both cases is presented in Fig.(5.5) and was discussed already, with the conclusion that no bias dependence of the transmission was observed in our experiments and the conductance of  $1G_0$  was not reproduced by the calculations. A detailed analysis of the stretching dependence of the vibration frequencies in the computational model is presented in Fig.(5.11). In the upper panels of both figures are shown the vibration frequencies as functions of the distance between the contacts. The structure of the electrodes for which the calculations are performed is presented in the insets and the distance is measured between the bulk parts (the first layer of Pt atoms in the pictures). The lower panels show the conductance as a function of the distance between the contacts. In both situations they find that five out of the six oscillations have frequencies between 0 and 60meV. In the case of the upright orientation (Fig.(5.11(left))), all modes decrease upon stretching. The lowest one is the rotation around the contact with an energy below 10meV. The next one is in the range (30-15)meV and corresponds to a center-of-mass (CM) motion parallel to the contact axes. Between  $\simeq 45$ meV and  $\simeq 22$ meV we find a CM oscillation perpendicular to the contact axes. Between  $\simeq 45$ meV and  $\simeq 35$ meV is the hindered rotation mode in the plain perpendicular to the axis of the contact. Hindered rotation in the plain normal to the mirror plain is found between  $\simeq 58$ meV and  $\simeq 45$ meV. The only mode with a frequency well above 60meV is the internal vibration of the molecule and it is in the range between

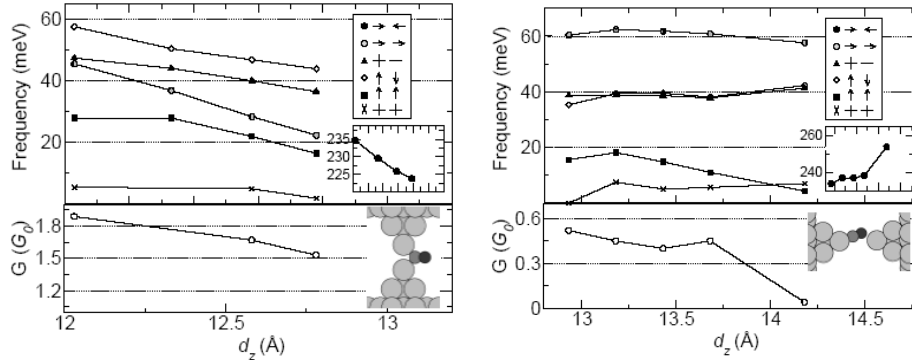


Figure 5.11: *left and right: Vibrational frequencies (upper panel) and conductance (lower panel) as a function of the electrode displacement. The molecule is in an upright position (left) or tilted bridge (right) position in the contact, as shown in the pictures. The motion of the molecule for different modes is described in the legends which refer to the pictures of the contacts in the insets. After Ref. (65)*

235meV and 220meV, also decreasing with stretching. The conductance in this case is also decreasing with increasing distance between the electrodes and for an elongation of  $\simeq 0.8$  Å it drops from  $\simeq 1.9G_0$  to  $\simeq 1.5G_0$ .

In the case of the tilted bridge configuration all modes have a characteristic stretching behavior, non of them being monotonous. The lowest frequency belongs to a transversal CM mode and it increases upon the stretching from 0meV close to 10meV. If we place the system in Cartesian coordinate system with  $\mathbf{x}$  being the axis of the contact, this mode will be the oscillation along the  $\mathbf{z}$  axis. Another transversal mode is found between 5meV and 20meV and it is an oscillation along the  $\mathbf{y}$  axis. The hindered rotation modes in the  $xy$  and  $xz$  plane are almost degenerate and flat around  $(40\pm 5)$ meV. The CM oscillation along the  $\mathbf{x}$  axis is in the range  $60\pm 5$ meV and the internal oscillation of CO molecule is in between 230meV and 255meV, depending on the distance between the electrodes.

Since non of those two models gave the experimentally observed vibration mode around 110meV, Strange *et al.* investigated the possibility of having a molecular bridge consisting of two molecules like the two presented in Fig.(5.12).

The figure on the left presents a configuration with the transmission very strongly dependent on the energy, so the total transmission decreases from  $T=0.78$  at the Fermi energy  $E_F$  down to  $T=0.52$  at  $E_F+ 0.1eV$ . The binding energy of this structure is 0.8eV per molecule, which is much less comparing to the binding energy of a single molecule being 2.5eV, so this is a metastable configuration. The figure on the right forms a system of coupled oscillators with twelve oscillation modes. The total conductance of the structure is very close to  $1G_0$  for zero bias, but still very strongly dependent on the energy, and the

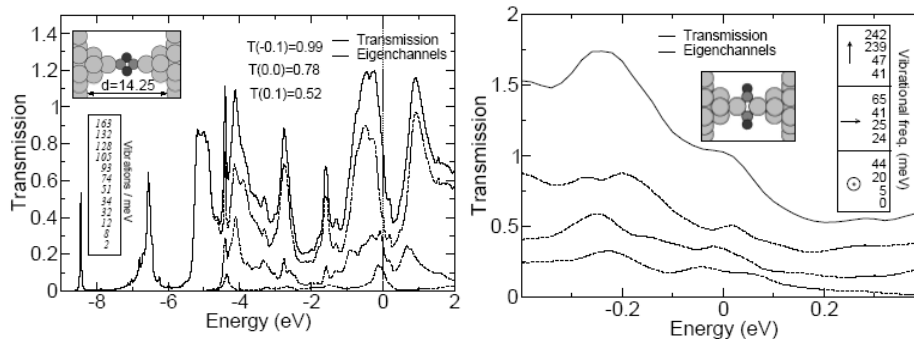


Figure 5.12: *left: Transmission as a function of the energy for a  $C_2O_2$  structure bridging the gap between Pt tips. Oscillation frequencies are shown in the box on the left. right: Transmission as a function of the energy for two upright positioned molecules bridging the Pt tips and the oscillation frequencies of this structure, shown in the box on the right. After ref. (65)*

total transmission results from a combination of three conductance modes.

## 5.10 Discussion of the vibration modes for CO

Spectroscopic data collected from about ten experimental runs make a set which, when presented in the form of a histogram (Fig.(5.8)) gives the preferential values for the oscillation frequencies. The peaks obtained in the histogram correspond to the pronounced spectroscopic features in the individual  $dI/dV$  curves. In many cases several of them appear together, like in Fig.(5.7), proving that we are dealing with distinct vibration modes, not coincidentally created peaks. Looking at the fitting parameters from the OLM we can conclude that the typical coupling strength is of the order of  $\sim 10^{12}s^{-1}$ . It can also be seen that for the different modes, even on the same curve, the coupling strength is usually different and it can differ by a factor of 5 as can be seen from the parameters given in (5.4) referring to Fig.(5.7*iii*). Also, the same mode can have a different coupling strength for different curves, which may be explained by a different positioning of the molecule in the contact or a different arrangement of the Pt atoms in the leads. An interesting observation (as discussed in chapter 4) is that the temperature obtained as a fitting parameter is very often significantly higher than the bath temperature and is higher for the higher modes than for the lower ones as long as they are present in the same curve. Otherwise, the correlation does not hold as can be seen from the 31meV and 76meV excitations presented in the set of fitting parameters (5.2) and (5.4) referring to Fig.(5.7*i*) and (*iii*).

The efforts towards the interpretation of the obtained modes were presented in the stretching dependence of the observed frequencies (Fig.(5.9)). If the frequency of a certain mode increases upon the stretching it can not be a longi-

tudinal mode. In the case of hydrogen and deuterium, it served to select which modes are transversal and which longitudinal. In the case of CO that effort gave no clear result since all modes showed very weak decreasing tendency, except the highest one with a slightly more pronounced decreasing behavior. We were actually looking for the increasing behavior to pick out the transversal ones. However, if the arrangement of the molecule is asymmetric as in the calculation of Fig.(5.12 (*left*)), this simple rule breaks down. As a conclusion we can say that we did not succeed to classify the modes experimentally.

The theoretical effort did not help a lot either. Starting with the model of a molecule in upright position between the contacts (Fig.(5.11(*left*))). In Fig.(5.5 (*right*)) curve (A) presents the transmission of the bridge. The conductance at zero bias is around  $1.5G_0$  which is not the conductance obtained in the experiment. The other peculiar feature is the strong transmission dependence on energy. The only common feature with the experimental data is the general weak decreasing behavior of all modes upon the stretching. There are no characteristic features or behaviors on either experimental or theoretical stretching behaviors which make it possible to establish at least a qualitative correspondence between the predicted and measured modes since the exact values do not match. Although it is far from matching, there are few details which could be in favor of interpretation in terms of the model by Strange *et al* where the molecule evolves from upright to a tilted bridge configuration. In the calculation this configuration appears during the breaking of the contact as the configuration before the one with  $0.5G_0$  conductance, like in the experiment. Also, if we assume that the change from  $1G_0$  to  $0.5G_0$  in experiment is due to the change in molecular orientation, the value of  $0.5G_0$  must be due to the molecule oriented such as to bridge a larger gap between the Pt electrodes than in the case of  $1G_0$ . This would correspond to the upright followed by the tilted bridge configuration. At least the stretching dependence of the vibration modes in the calculation does not contradict the experimentally observed behavior.

Disagreement of the experiment for junctions with  $G \simeq 1G_0$  with the second model where the molecule is in the tilted bridge configuration is even bigger. It also has a strong transmission dependence on energy (Fig.(5.5 (*right*))) curve B). The total conductance during breaking does not match and the values for the frequencies do not match either. The biggest disagreement is in the fact that by further stretching of this configuration, the contact slowly breaks, while the configuration on which the experimental spectra are taken jumps in another stable configuration with conductance of  $0.5G_0$ , but as explained earlier, this could be an artifact.

The other two proposed models may hold a key to the solution, but are not entirely convincing. The one with  $C_2O_2$  presented in Fig.(5.12(*left*)) is only a metastable configuration with a conductance through three partially opened channels, so it does not meet the requirement of one entirely opened channel which is suggested in the experiment from the low conductance fluctuations in the background, but it has a vibration frequency around 120meV as observed in experiments. The model with two upright placed molecules presented in Fig.(5.12(*right*)) has the matching conductance, although carried by three

partially opened channels.

## 5.11 Conclusions

The key features we obtained in the above discussed experiment are two stable configurations with conductances close to  $1G_0$  and  $0.5G_0$  observed in the breaking traces and conductance histograms. For the configuration with the conductance close to  $1G_0$  we measured five or six vibration modes (nearly the full set if a single CO molecule is bridging the gap) and the stretching dependence for some of them. From the OLM we could extract the electron-phonon coupling strengths. Despite the large number of measured characteristics we can not conclude what is the position of the molecule in the junction. Very extensive DFT calculations by Strange, Thygesen and Jacobsen, exploring different possible configurations, corresponding conductances, vibrations and the stretching dependence of the oscillation frequencies could not produce a set of parameters which matches the measured values. One of the main disagreements is in the vibration modes, where the  $110\pm 12\text{meV}$  was not obtained for any of the configurations except the metastable  $\text{C}_2\text{O}_2$  arrangement. In fact, the highest mode in calculations is the internal C-O vibration, which is fairly insensitive to the bridging configuration. If our junction has a single CO molecule and if we have indeed observed six different modes the  $110\text{meV}$  mode must be internal mode, because we find six modes. This would require a very strong modification of the CO bond. It seems more likely that there is more than a single CO involved and that the internal mode is not observed because it is too high in energy. This all shows that the experimental tools which we have available at the moment, together with the computational knowledge and abilities, are not enough to understand the conductance properties of a molecule not much more complicated than hydrogen. Although this conclusion is disappointing it holds an important message: when we consider molecular junctions the actual arrangement realized may differ from the ones we imagine or find in computational modes. At least the large set of parameters that we have measured allows us to refuse the models for Pt-CO-Pt that have been considered to this point.

## Chapter 6

# Towards larger molecules

This work is performed in collaboration with M. Kiguchi.

### 6.1 Motivation

The outline of the experimental part of this thesis presented in the first lines of Chapter 2 led us from  $\text{H}_2$  and its isotopes to more complicated CO and at the end we arrive at experiments with  $\text{C}_2\text{H}_2$  and  $\text{C}_6\text{H}_6$  on the way towards more complex molecules. Here at the beginning it should be stressed that the presented data are preliminary and any possible interpretation based on this limited knowledge is tentative.

### 6.2 Experiments on acetylene ( $\text{C}_2\text{H}_2$ )

Based on experience with  $\text{H}_2$  and the formation of a stable chemical bond between H and Pt,  $\text{C}_2\text{H}_2$  looks like a good candidate which could show if H can be used as a binding element, a sort of interface between the metal (in this case Pt) and the molecule whose integral part this H is. Furthermore, the triple bond is likely to hybridize strongly with the Pt  $d$  orbitals and this opens the possibility of exploring the Pt-triple C-C bond as anchoring group for more extended molecular structures. In acetylene, H and C atoms are bound by sharing a  $1(s)$  and  $2(sp)$  orbital forming a  $\sigma$  bond. Two C atoms are forming a triple bond by one  $\sigma$  bond made from  $2(sp)$  electrons and two  $\pi$  bonds made by pairing  $2p_x$  and  $2p_z$  electrons. Acetylene on Cu surfaces was extensively studied by W. Ho and coworkers and can be found in Ref.(67). Theoretical calculations which will predict the mechanism for  $\text{C}_2\text{H}_2$  binding to Pt atoms in the MCBJ configuration are still needed at this moment. The purity of gas used in the experiments was 99.5%. The experimental setup used for measurements on  $\text{C}_2\text{H}_2$  is identical to the one used for CO. The procedure to introduce  $\text{C}_2\text{H}_2$  in the system was similar to the one described in the CO experiments. The boiling point for  $\text{C}_2\text{H}_2$  is around 180K, so the path which molecules travel to reach the sample must be

heated. The experiment starts with a Pt sample wire mounted in a MCBJ configuration placed in a vacuum pot evacuated to a pressure around  $1 \cdot 10^{-5}$  mBar at room temperature and then cooled down to liquid He temperature (4.2K). The wire is broken under cryogenic vacuum so that it can not be contaminated. The purity of wire is checked by recording a conductance histogram which in case of Pt shows a peak close to  $1.5G_0$  as presented in Fig.(6.1 left).

After the molecules were injected into the chamber, the histogram changed from the one presented in the left panel into the one presented in the right panel in Fig.(6.1) with a peak at  $1G_0$  and a significant count number in the low conducting range. A typical differential conductance curve obtained on a contact with a conductance close to  $1G_0$  is presented in the left panel in Fig.(6.2) and the right panel shows the total distribution of frequencies obtained in all measurements performed on Pt-C<sub>2</sub>H<sub>2</sub>-Pt junctions.

The number of successful measurements on Pt-C<sub>2</sub>H<sub>2</sub>-Pt junctions is quite limited and the distribution of vibration frequencies presented in Fig.(6.2) is collected from about 50 measured curves. The distribution obtained from this set of measurements shows two peaks where one of them is around 53meV and is quite distinct while the other is centered around 67meV and is rather broad so no conclusions about the number of vibration modes should be drawn from this distribution. A critical issue in experiment on Pt-C<sub>2</sub>H<sub>2</sub>-Pt junctions is the possibility of H<sub>2</sub> contamination since H<sub>2</sub> is present at low concentrations in the gas bottle we used ( $< 0.1\%$  H<sub>2</sub>). Although, without heating the capillary no change in the Pt conductance histogram was observed, the H<sub>2</sub> distribution has peaks centered around 54meV and 71meV (see Chapter 2) and these are just in the range where the count numbers in the C<sub>2</sub>H<sub>2</sub> distribution are high. The main arguments that support an interpretation of the signals as due to acetylene are the small but noticeable difference of the conductance histograms and the difference in the main peak position in the distribution of observed frequencies. The way to further examine this is to use the isotope substitution, C<sub>2</sub>D<sub>2</sub> and <sup>13</sup>C<sub>2</sub>H<sub>2</sub> and study the stretching dependance.

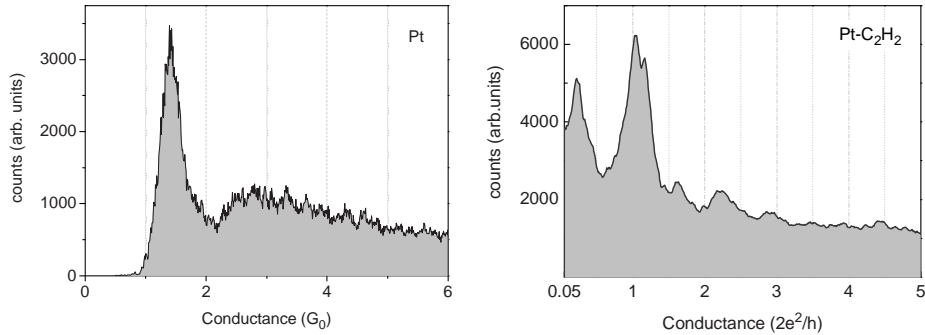


Figure 6.1: *Conductance histogram for clean Pt contact (left) and after C<sub>2</sub>H<sub>2</sub> gas was injected into the sample chamber.*

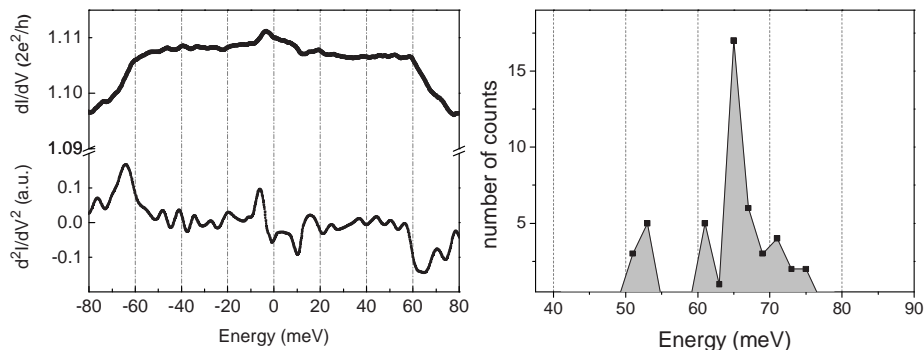


Figure 6.2: *left: Differential conductance ( $dI/dV$ ) as a function of the energy (upper curve) and  $d^2I/dV^2$  obtained as a numerical derivative of  $dI/dV$  curve (lower curve). The peak in the second derivative corresponds to a vibration excitation of the molecule in the contact. right: Distribution of vibration frequencies obtained in all measurements on Pt- $C_2H_2$ -Pt junctions.*

The change in conductance histogram shows the change from Pt conductance of around  $1.5G_0$  to a histogram with structure at low conductance values and a clear peak at slightly higher conductance than  $1G_0$ . This forms an indication that the junctions near  $1G_0$  are not due to  $H_2$  which would give a peak slightly below  $1G_0$ . PCS measurements on contacts with conductance close to  $1G_0$  shows a clear steps in  $dI/dV$  curves which determines the frequencies of molecular vibrations. Observed  $dI/dV$  curves are sometimes quite flat which suggests that in those cases the conductance is probably carried dominantly by one conductance channel. To classify the Pt- $C_2H_2$ -Pt vibration modes more PCS measurements with stretching dependence should be done. The isotope substitutions  $C_2D_2$  and  $^{13}C_2H_2$  need to be tested and shot noise measurements should be done to get closer information on the number of conductance channel of this molecular junction. Since it is very likely that one of the important contributions to conductance through Pt- $C_2H_2$ -Pt bridges comes from the triple C-C bond, it is interesting to perform experiments with  $C_2H_4$  and  $C_2H_6$  instead of  $C_2H_2$  and systematically replace the triple C-C bond by double and single bonds.

## 6.3 Experiments on benzene ( $C_6H_6$ )

Experiments on  $C_6H_6$  have been performed in collaboration with Manabu Kiguchi (68). Since  $C_6H_6$  is in the liquid state at room temperature with a vapor pressure of  $\sim 1\text{mBar}$  at  $250\text{K}$ , a special system to introduce the  $C_6H_6$  vapors was designed. The residual air contaminations unavoidably present in the specially designed glass container after filling the  $C_6H_6$  liquid are removed in freeze-pump-thaw cycles and the  $C_6H_6$  vapors are injected through the capillary heated to around  $300\text{K}$  while the sample wire remains at liquid helium temperature.

### 6.3.1 Introducing $C_6H_6$ molecules into the cryogenic environment

At room temperature benzene is a liquid. The vapor pressure of benzene at  $250\text{K}$  is  $\sim 1\text{mBar}$  and to bring it down to the junction which is placed at the end of  $\sim 1.5\text{m}$  long dipstick running through liquid helium, a special capillary had to be designed. When heated, the coldest spot on it must not be colder than  $260\text{K}$  and when it is not heated it should be at  $4.2\text{K}$  almost along the whole length because otherwise it would allow the diffusion of contaminations from the top of the insert where the vacuum is only  $\sim 10^{-6}\text{mBar}$  and the walls are at room temperature. The solution we have developed is presented in Fig.(6.3). As shown in the drawing, the inner tube is made of two parts. The upper part which is partially above the liquid helium level is made of stainless steel with  $3\text{mm}$  outer and  $2\text{mm}$  inner diameter. The lower part which is always supposed to be entirely below the liquid helium level is made out of copper with  $2\text{mm}$  outer and  $1\text{mm}$  inner diameter. The reason for such two component design is to reduce the heat flow from the room temperature part towards the lower parts of the insert. A possible heat load will increase the chance of contamination,

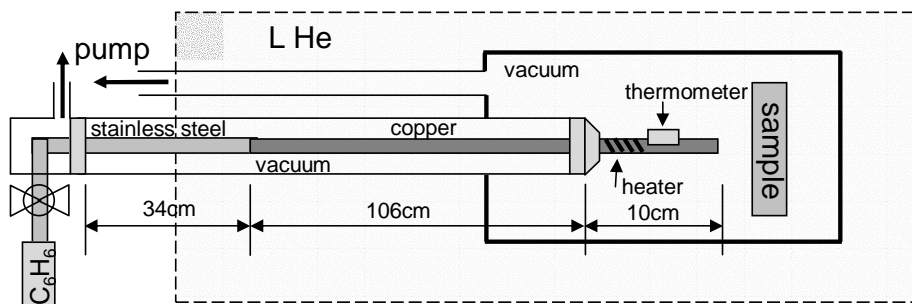


Figure 6.3: Drawing of the double-walled capillary system. The inner capillary consists of an upper part made of stainless steel and a lower part made of copper. The outer tube which is in contact with liquid He is made of stainless steel. In between the two tubes is vacuum. The heater wire is wrapped around the lower end of Cu part.

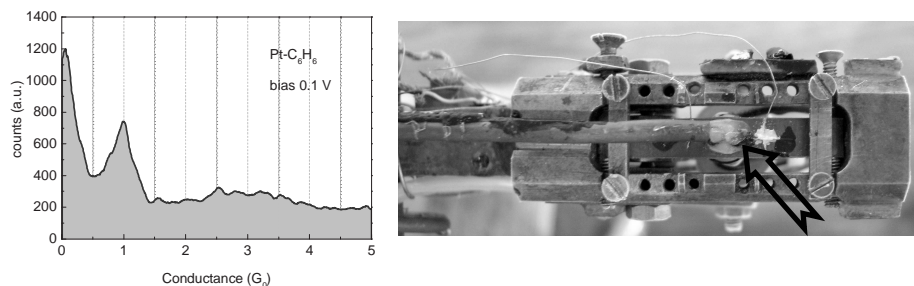


Figure 6.4: *Conductance histogram for Pt after  $C_6H_6$  was injected in the contact (left). On the right is a photo taken immediately after the insert was taken out of the He bath after  $C_6H_6$  was injected. The light shadow pointed by arrow is a patch of frozen  $C_6H_6$ .*

possibly increase the temperature of the sample and increase the liquid helium boil off because the heat transported from the end kept on room temperature will sink in the helium bath. By this design a significant amount of heat is dissipated only during the heating by the heater placed at the bottom. The power dissipated while activating the heater is approximately 2W.

The presence of  $C_6H_6$  molecules in the junction is detected in the conductance histogram. A typical histogram of Pt changes into the one presented in the left panel in Fig.(6.4). Presence of benzene on the sample was also visually observed in an experiment where a large gas amount was admitted. When the setup which was cooled down to liquid He temperature was quickly taken out and opened, a small patch of frozen benzene could be observed on the sample as shown in the picture in right panel in Fig.(6.4). The conductance histogram taken on a Pt contact after  $C_6H_6$  was injected shows a pronounced peak close to  $1G_0$  and a high count at low conductances. Differential conductance measurements were performed in both regions of conductance, close to  $1G_0$  and in the low conductance region.

### 6.3.2 PCS spectra near $1G_0$

An example of PCS spectra taken in the range of conductance close to  $1G_0$  is presented in the left panel in Fig.(6.5) and the distribution of all spectra (around 200 curves) taken at the conductances close to  $1G_0$  are shown in the right panel. As can be seen from the shape of the presented curve, there is a large irregular background present which interferes with vibrationally induced steps in the differential conductance curves. The signals are not as convincing as for the molecules discussed above. The distribution is very broad, but one may recognize three maxima.

### 6.3.3 PCS spectra at low conductances

As can be seen from the conductance histogram presented in the left panel in Fig.(6.4), there is a second peak in the low conductance regime. Its position varies between experiments from  $0.1G_0$  to  $0.4G_0$ . PCS spectra could be obtained on such low conducting contacts and are in shape similar to IETS spectra. The spectra in this range have much better signal to noise than those obtained near  $1G_0$ . One example of such a curve is shown in the left panel in Fig.(6.6). Regardless of the exact conductance of the contact in this low-conductance region, the vibration frequencies obtained from about 200 curves form a quite narrow distribution shown in Fig.(6.6 right). The rather small scatter in the data points makes it possible to see the shift in frequency by substituting  $^{12}\text{C}$  in  $\text{C}_6\text{H}_6$  with  $^{13}\text{C}$ . A rough estimate obtained taking into account only the total difference in mass ( $m(^{12}\text{C}_6\text{H}_6)=78$ ,  $m(^{13}\text{C}_6\text{H}_6)=84$ ) gives that the peak position should shift down by about 2meV since

$$\omega(^{12}\text{C}_6\text{H}_6) = \sqrt{\frac{m(^{13}\text{C}_6\text{H}_6)}{m(^{12}\text{C}_6\text{H}_6)}} \omega(^{13}\text{C}_6\text{H}_6).$$

The observed shift is presented in the right panel in Fig.(6.6).

Based on above presented measurements we can make a tentative interpretation of vibration frequencies observed. The closest frequency of a benzene molecule in the gas phase is around 51meV and it is the ring deformation mode where all even carbon atoms move up while the odd ones move down. When the molecule is placed on a Pt(111) surface, the frequency of that mode increases to around 72meV. Although the frequency increased when the molecule was placed at the surface, it is still possible that it will decrease if placed between two surfaces since the electron density between carbons may decrease due to binding

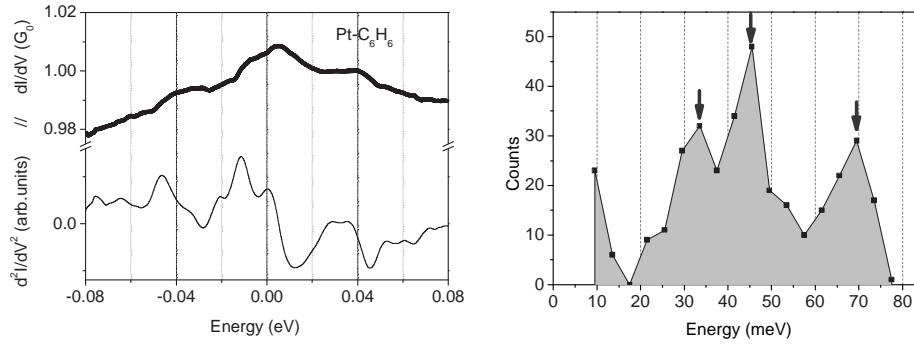


Figure 6.5: left:  $dI/dV$  (upper curve) and  $d^2I/dV^2$  (lower curve, numerical derivative of the upper one) as a function of the energy taken on a  $\text{Pt-C}_6\text{H}_6$  junction with conductance close to  $1G_0$ . right: Distribution of all frequencies obtained in measurements with  $\text{Pt-C}_6\text{H}_6$  junction with conductances close to  $1G_0$ .

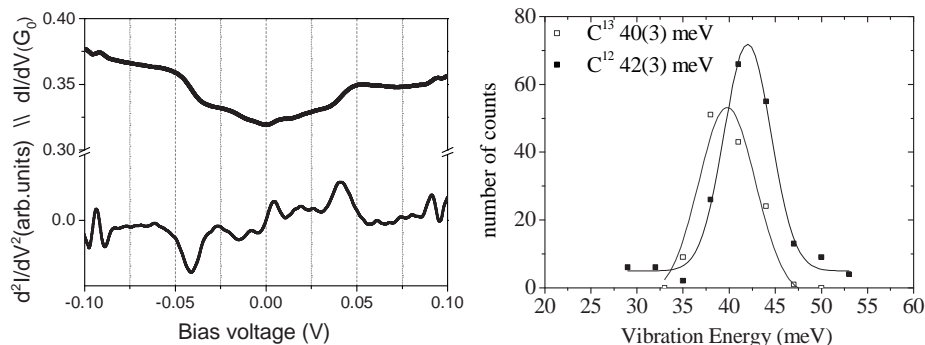


Figure 6.6: *left:  $dI/dV$  (upper curve) and  $d^2I/dV^2$  (lower curve) as a function of the energy, taken on a  $Pt-C_6H_6$  junction with low conductance. right: Distribution of all frequencies obtained in measurements on a  $Pt-C_6H_6$  junction with low conductance. The data obtained when  $^{12}C$  in  $C_6H_6$  was substituted with  $^{13}C$  form a distribution with its center shifted by about  $2meV$  to lower values.*

to Pt atoms. The effect of frequency increase due to elastic Pt-C binding force will now cancel out since it is symmetric from both sides. Preliminary DFT calculations were done by van der Zant and coworkers. They used a simplified model where benzene is sandwiched flat between two Pt atoms. The obtained frequency is around  $42meV$  for the above mentioned mode.

## 6.4 Conclusions

A special setup was designed to be able to inject benzene vapors in the cryogenic environment. The presence of the molecules is recorded by changes in the conductance histogram. Spectroscopical measurements were done on contacts with the conductance close to  $1G_0$  and in the range of conductances between  $0.1G_0$  and  $0.3G_0$ . The differential conductance around  $1G_0$  is significantly influenced by conductance fluctuations but features originating from molecular vibrations were recognizable and the distribution of observed frequencies showed rather large scatter from which it is difficult to judge the number of vibration modes. In the lower conductance regime, conductance fluctuations are significantly suppressed, the observed vibration mode is not influenced by the total conductance and forms quite a sharp distribution so that the frequency shift due to isotope substitution was observed. Preliminary theoretical calculations are performed on a simple model and they need to be verified by a calculation on more realistic system. Experimentally, this may be important example of excitation of internal mode of vibration, in contrast to the vibration modes for  $H_2$  and  $CO$ , so it gives hope for fingerprinting larger molecules. It also shows that metal-molecule bonds can be formed without the use of thiol groups, as is the most frequently used approach in molecular electronics experiments. The direct link between the metal and the delocalized  $\pi$  orbitals of the molecule give rise to a

high conductance of the junction.

## Chapter 7

# Anomalous $dI/dV$ curves: a mechanism of intrinsic signal amplification

This work was performed in collaboration with R. Thijssen, A. Otte and R. Bremer. Accepted for publication in Phys Rev Lett.

### 7.1 Introduction

A very important technique for characterization of point contacts and molecular bridges is Point Contact Spectroscopy (PCS), described and used in earlier chapters. It works well for contacts with very low transmission, like in tunnelling junctions, where it is usually known as inelastic electron tunnelling spectroscopy (IETS), as well as for the contacts with perfect transmission (no partially transmitting channels). But in case of intermediate transmissions or contacts with high conductance, but made of several partially open transmission channels, PCS performs very poorly since the rather small signal becomes entirely lost in conductance fluctuations. Investigating anomalous  $dI/dV$  curves as the ones presented in Fig.(7.1) we developed a model which provides a tool to detect molecular vibrations even if conductance fluctuations are huge and can also be used to detect vibration modes which are weakly coupled to electrons.

## 7.2 Motivation: anomalous dI/dV curves

The model, which is presented below, is based on differential conductance measurements which, instead of conventional spectra like the ones presented earlier in this thesis, gave anomalous curves as the ones in Fig.(7.1).

Similar data can be found in the literature. Goudioso *et al.* in Ref.(69) reported Negative Differential Resistance (NDR) in an STM experiment of pyrrolidine ( $C_4H_8NH$ ) molecules on a copper (001) surface and they attribute it to a flipping of the molecule between two different orientations. The flipping is triggered by intrinsic molecular vibrations and the negative slope in differential conductance is due to the lower conductance in the flipping regime. The conductance above the threshold voltage is the average of the conductance in the first position, below the threshold, and the conductance when the molecule is in the low conductance orientation.

Measurements obtained by Gupta *et al.* are presented in Ref.(70). In low-temperature STM differential conductance measurements on a copper surface

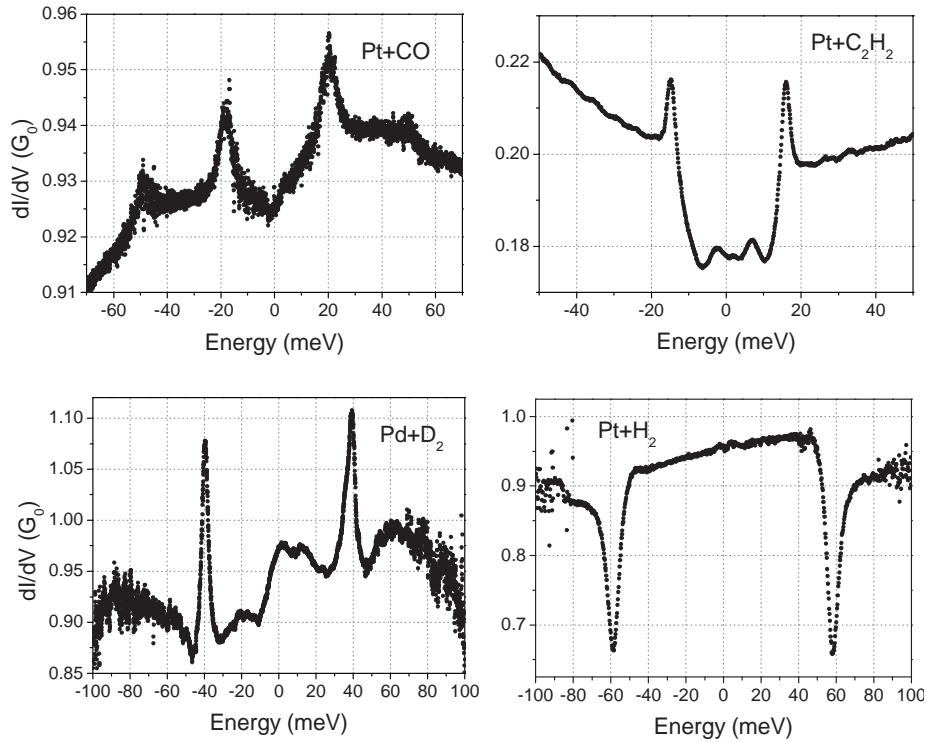


Figure 7.1: *Examples of anomalous differential conductance curves as a function of the voltage. Presented curves are a small selection of curves with peaks and dips at the positions where in normal PCS spectra one finds a signature of vibration excitations.*

with a sub-monolayer of physisorbed hydrogen they observed peaks symmetrically placed at around 120meV for positive and negative voltages. The precise value was seen to depend on the degree of hydrogen coverage. To explain the data they presented a phenomenological model assuming two different conductances of left and right side of a double-well potential.

Another possible example of similar curves comes from Wang *et al.* (71) who measured differential conductance of a alkanedithiol self-assembled monolayer. The layer was sandwiched in between two gold contacts using a micro-fabricated nano-pore. The obtained spectra are regarded as regular IETS spectra (72) despite the unexpected anomalous dips in  $d^2I/dV^2$  curve in Fig. (3) in Ref. (71). Having in mind that our model will be constructed for a single molecule junctions, while the experiment by Wang *et al.* was performed on a thin film of molecules, the shape of sharp peaks and dips in  $d^2I/dV^2$  curves could be reproduced.

The common features in all these three cases are anomalous peaks in  $dI/dV$  curves which we propose to attribute to a vibration excited Two Level System (vTLS). Although many of the ingredients of an interpretation in terms of vibration excited two-level system are discussed in the papers cited above, a complete model has not been proposed. In measurements presented in this thesis such features were observed on all molecules which were under investigation ( $D_2$ ,  $H_2$ , HD, CO,  $C_2H_2$  and  $C_6H_6$  with Pt contacts and  $D_2$  with Pd contacts). Independently, the same features were observed by Robert Thijssen, in our group in Leiden, in experiments with  $H_2$  and  $O_2$  with gold and nickel.

### 7.3 The model

The general idea which will be discussed below is the following: A single molecule is bridging a gap between two atomically sharp tips made by breaking a wire in MCBJ configuration. The molecular junction is assumed to have two configurations which are very close in energy but the energy barrier between the two is still large enough that the system can not spontaneously cross from one to the other. When molecular vibrations are excited, the system can tunnel between the two potential wells. Such a system can be modelled by a system of two potential wells with the barrier in between high enough that the tunnelling between the two ground states is impossible, but system from both ground states can be excited to the levels between which tunnelling is possible. In addition, we assume that the two configurations (molecule in left or right well) have slightly different conductances. Two wells with slightly different conductances will produce a step in the I-V curve which will result in a peak in the  $dI/dV$  curve, as will be shown below.

Let us assume that the molecule is confined by a double-well potential. If there is no tunnel-coupling, and both wells are treated separately, the system can be viewed as two separate harmonic oscillators.  $\Psi_A$  and  $\Psi_B$  are excited states of the left and right harmonic oscillator with the energies  $E_A$  and  $E_B$  respectively. If zero energy is defined as in Fig.(7.2),  $E_A = -\Delta_0$  and  $E_B = \Delta_0$ . When a

tunnelling coupling  $\Delta$  between the two states is included, the Hamiltonian of such a system, represented in the basis  $\{\Psi_A, \Psi_B\}$ , is:

$$H = H_0 + H' = \begin{pmatrix} -\Delta_0 & 0 \\ 0 & \Delta_0 \end{pmatrix} + \begin{pmatrix} 0 & \Delta \\ \Delta & 0 \end{pmatrix}. \quad (7.1)$$

Since  $H$  is a hermitian operator, it can be diagonalized by solving the following eigen problem:

$$H|\Psi_{\pm}\rangle = \begin{pmatrix} -\Delta_0 & \Delta \\ \Delta & \Delta_0 \end{pmatrix} \begin{pmatrix} \alpha \\ \beta \end{pmatrix} = E_{\pm} \begin{pmatrix} \alpha \\ \beta \end{pmatrix} \quad (7.2)$$

The energy levels and eigenstates obtained are:

$$E_{\pm} = \pm \sqrt{\Delta_0^2 + \Delta^2} \quad (7.3)$$

$$\Psi_{\pm} = \alpha_{\pm}\Psi_A + \beta_{\pm}\Psi_B \quad (7.4)$$

with coefficients  $\alpha_{\pm}$  and  $\beta_{\pm}$ :

$$\alpha_+ = \frac{1}{\sqrt{2}} \frac{\Delta}{\sqrt{\Delta^2 + \Delta_0^2 + \Delta_0 \sqrt{\Delta^2 + \Delta_0^2}}}, \quad (7.5)$$

$$\beta_+ = \frac{1}{\sqrt{2}} \frac{\Delta_0 + \sqrt{\Delta^2 + \Delta_0^2}}{\sqrt{\Delta^2 + \Delta_0^2 + \Delta_0 \sqrt{\Delta^2 + \Delta_0^2}}} \quad (7.6)$$

$$\alpha_- = \frac{1}{\sqrt{2}} \frac{\Delta}{\sqrt{\Delta^2 + \Delta_0^2 - \Delta_0 \sqrt{\Delta^2 + \Delta_0^2}}}, \quad (7.7)$$

$$\beta_- = \frac{1}{\sqrt{2}} \frac{\Delta_0 - \sqrt{\Delta^2 + \Delta_0^2}}{\sqrt{\Delta^2 + \Delta_0^2 - \Delta_0 \sqrt{\Delta^2 + \Delta_0^2}}} \quad (7.8)$$

States  $\Psi_A$  and  $\Psi_B$  can be represented in the basis of eigenstates of the coupled system  $\{\Psi_+, \Psi_-\}$ :

$$\begin{aligned} |\Psi_A\rangle &= -\beta_-|\Psi_+\rangle + \beta_+|\Psi_-\rangle, \\ |\Psi_B\rangle &= \alpha_-|\Psi_+\rangle - \alpha_+|\Psi_-\rangle \end{aligned} \quad (7.9)$$

### 7.3.1 Time evolution

The time evolution of a system is given by a simple phase factor only for eigenstates of the system. In the case of TLS those are  $\Psi_+$  and  $\Psi_-$ . If the system is initially prepared in a spatially defined arbitrary state  $\Psi_A$  which is not an eigenstate, the probability to find it in eigenstate state  $\Psi_+$  at any time  $t$  is:

$$\begin{aligned} |\langle \Psi_+ | \Psi_A(t) \rangle|^2 &= |\langle \Psi_+ | e^{i\hat{H}t} [-\beta_-|\Psi_+\rangle + \beta_+|\Psi_-\rangle] \rangle|^2 \\ &= |-\beta_- \langle \Psi_+ | e^{i\hat{H}t} | \Psi_+ \rangle + \beta_+ \langle \Psi_+ | e^{i\hat{H}t} | \Psi_- \rangle|^2 \\ &= |-\beta_- e^{i\frac{E_+}{\hbar}t} \langle \Psi_+ | \Psi_+ \rangle + \beta_+ e^{i\frac{E_-}{\hbar}t} \langle \Psi_+ | \Psi_- \rangle|^2 \\ &= \beta_-^2 \end{aligned} \quad (7.10)$$

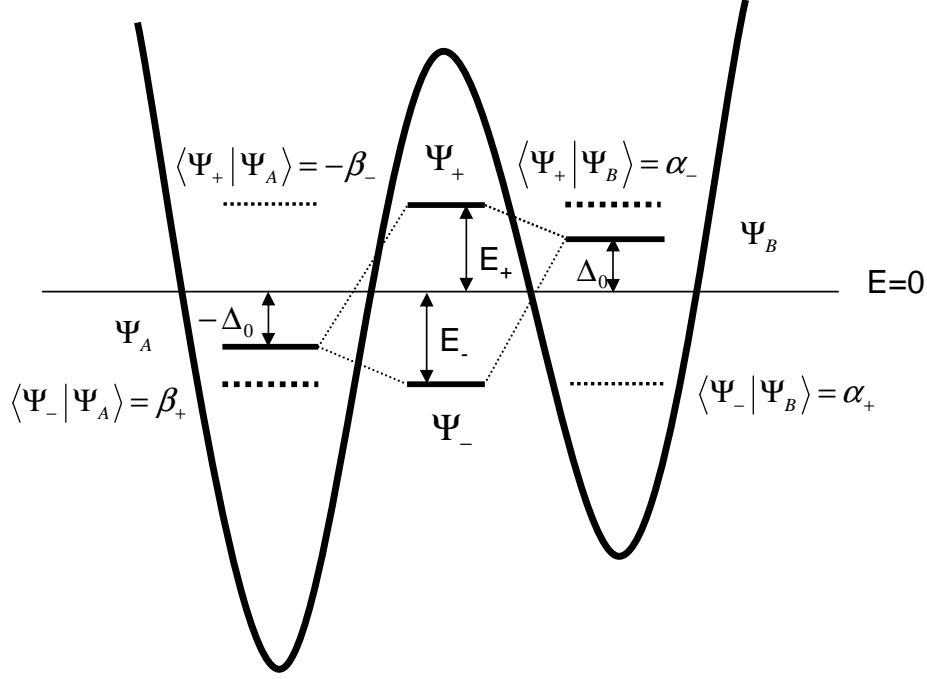


Figure 7.2: Model of a Two Level System (TLS). With no coupling between two wells, the eigenstates are  $\Psi_A$  and  $\Psi_B$ , localized in left and right well with no overlap. When tunnelling coupling is included, the new eigenstates delocalized over the whole system are  $\Psi_+$  and  $\Psi_-$ . The probability for the system initially represented by state  $\Psi_A$  to end in  $\Psi_+$  or  $\Psi_-$  is  $\beta_-^2$  and  $\beta_+^2$  respectively, and is constant in time and presented by dashed lines. Similar holds if the system is prepared in state  $\Psi_B$ .

Similarly:

$$|\langle \Psi_- | \Psi_A(t) \rangle|^2 = \beta_+^2, \quad |\langle \Psi_+ | \Psi_B(t) \rangle|^2 = \alpha_-^2, \quad |\langle \Psi_- | \Psi_B(t) \rangle|^2 = \alpha_+^2 \quad (7.11)$$

Important to notice is that the eigenstates  $\Psi_+$  and  $\Psi_-$  are well-defined energy levels, delocalized over two wells and they contain no information about spatial precession of the system. The probability to find the system after time  $t$  in state  $\Psi_B$  if it was initially prepared in state  $\Psi_A$ , having in mind that states  $\Psi_A$  and  $\Psi_B$  are spatially localized states which are not eigenstates of Hamiltonian is:

$$\begin{aligned} |\langle \Psi_B | \Psi_A(t) \rangle|^2 &= |\langle \Psi_B | e^{-i\hat{H}t} [ -\beta_- \Psi_+ + \beta_+ \Psi_- ] |^2 \\ &= | -\beta_- \langle \Psi_B | e^{-i\hat{H}t} | \Psi_+ \rangle + \beta_+ \langle \Psi_B | e^{-i\hat{H}t} | \Psi_- \rangle |^2 \\ &= | \beta_- e^{-i\frac{E_+}{\hbar}t} \langle \Psi_B | \Psi_+ \rangle + \beta_+ e^{-i\frac{E_-}{\hbar}t} \langle \Psi_B | \Psi_- \rangle |^2. \end{aligned} \quad (7.12)$$

After some algebra, the expression for the probability becomes:

$$|\langle \Psi_B | \Psi_A(t) \rangle|^2 = \frac{\Delta^2}{\Delta^2 + \Delta_0^2} \sin^2\left(\frac{\sqrt{\Delta_0^2 + \Delta^2}}{\hbar} t\right), \quad (7.13)$$

which on time scales much longer than  $\omega^{-1} = \hbar/\sqrt{\Delta^2 + \Delta_0^2}$  averages to:

$$\langle |\langle \Psi_B | \Psi_A(t) \rangle|^2 \rangle_t = \frac{1}{2} \frac{\Delta^2}{\Delta^2 + \Delta_0^2}. \quad (7.14)$$

### 7.3.2 TLS excited by molecular vibration

Our TLS consists of a molecule bridging a point contact gap. In the case of a harmonic potential, a molecule in the contact is essentially a harmonic oscillator with well defined excitation energies. When placed in a double-well potential, if the molecule does not vibrate, the TLS is in the lower ground state,  $\Psi_0$ , with negligible possibility for direct tunnelling to  $\Psi_1$  which is the ground state of the other well. The separation between the two ground levels of the TLS is  $E_\Delta = 2\Delta_0$ . A typical vibration mode energy for the molecules considered here is  $\hbar\omega \approx 60\text{meV}$ , the temperature is around 4.2K, and we will take  $k_B T \ll E_\Delta \ll \hbar\omega$ . An important characteristic of our TLS is that the ground states have well defined and usually different conductances  $\sigma_0$  and  $\sigma_1$ . When the molecule is excited by electron scattering by an energy  $\hbar\omega$ , the TLS is taken from the ground state  $\Psi_0$  to  $\Psi_A$ . At this moment, the TLS of Fig.(7.3) with energy splitting  $\Delta_0$  and the tunnelling probability  $\Delta$  applies. Once excited to  $\Psi_A$ , the system will oscillate between the left and right well, so it will precess between states  $\Psi_A$  and  $\Psi_B$  with the frequency  $\tau^{-1} = \frac{\sqrt{\Delta_0^2 + \Delta^2}}{\hbar}$  provided that it is not perturbed by further electron scattering during this time. When we integrate over long time period, if the system started from  $\Psi_A$ , the probability to find it in  $\Psi_B$  is, as already seen in (7.14) is given by:

$$\langle |\langle \Psi_B | \Psi_A(t) \rangle|^2 \rangle_t = \frac{1}{2} \frac{\Delta^2}{\Delta^2 + \Delta_0^2} \quad (7.15)$$

Since  $\Psi_A$  and  $\Psi_B$  are not eigenstates of the Hamiltonian, they can be represented as a linear combination of  $\Psi_-$  and  $\Psi_+$  which are the eigenstates, as shown in expression (7.9). That means, for the system initially in  $\Psi_0$  and for given  $\hbar\omega$ ,  $\Delta_0$  and  $\Delta$ , instead of  $\Psi_A$  with time dependent probability, we have two orthogonal states  $\Psi_-$  and  $\Psi_+$  with constant probabilities  $|\langle \Psi_- | \Psi_A \rangle|^2 = (-\beta_+)^2$  and  $|\langle \Psi_+ | \Psi_A \rangle|^2 = (\beta_-)^2$  to find the system there. This can also be interpreted that if the state  $\Psi_-$  is populated, it will be found in the left well with probability  $(-\beta_+)^2$ , and  $(-\alpha_+)^2$  to be on the right since  $\langle \Psi_+ | \Psi_A \rangle = -\alpha_+$ . Since the system is now delocalized over two wells, the total conductance will be the weighted sum of  $\sigma_0$  and  $\sigma_1$ , as discussed further below. The crossover between the regime when the system is resting in one well and when it starts to behave as a TLS will produce a characteristic behavior of occupation numbers of  $\Psi_0$ ,  $\Psi_1$ ,  $\Psi_-$  and  $\Psi_+$  which will result in peaks and dips in differential conductance.

### 7.3.3 The scattering rates

Figure (7.3) presents the vibrationally assisted Two Level System (vTLS) model with the weights of eigenstates at the left and right wells and all transition rates between the states. Considering that in dynamic equilibrium the occupation numbers of all states become constant and that their total sum has to be equal to one, from the rates introduced in Fig.(7.3) we find:

$$\begin{aligned}
 \frac{dn_0}{dt} &= -W_{-0} - W_{+0} + W_{0-} + W_{0+} = 0 \\
 \frac{dn_1}{dt} &= -W_{-1} - W_{+1} + W_{1-} + W_{1+} = 0 \\
 \frac{dn_+}{dt} &= -W_{0+} - W_{1+} + W_{+0} + W_{+1} - W_{-+} + W_{+-} = 0 \\
 \frac{dn_-}{dt} &= -W_{0-} - W_{1-} + W_{-0} + W_{-1} - W_{-+} + W_{+-} = 0 \\
 n_0 + n_1 + n_- + n_+ &= 1
 \end{aligned} \tag{7.16}$$

where  $W_{pq}$  represent the rates of transition from state  $q$  to state  $p$  and  $n_0$ ,  $n_1$ ,  $n_-$  and  $n_+$  are the occupation numbers of the states  $\Psi_0$ , and  $\Psi_1$ ,  $\Psi_-$  and  $\Psi_+$  respectively. The system (7.16) reduces to a system of four linear equations

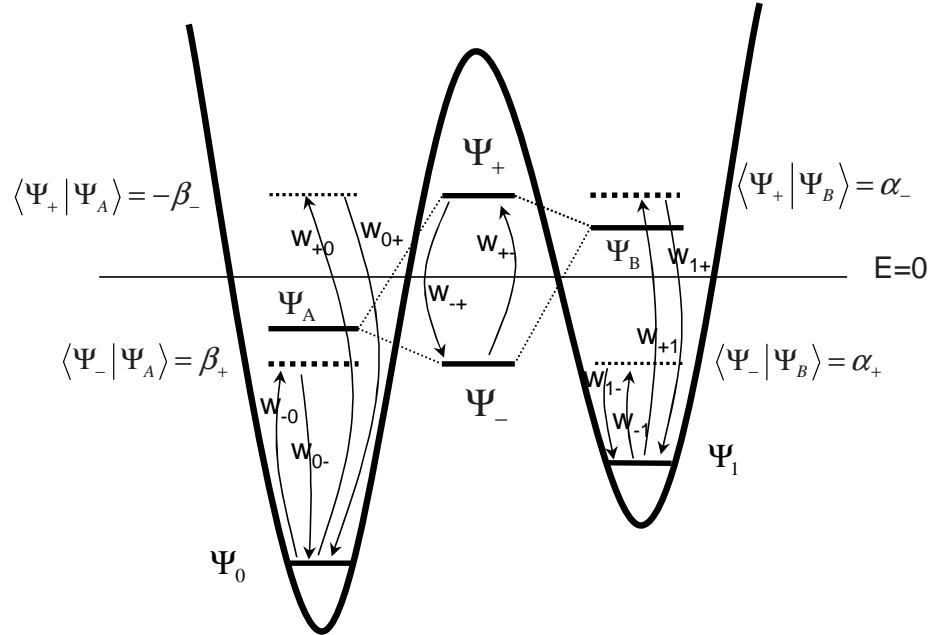


Figure 7.3: Model of a vibrationally assisted Two Level System (vTLS). For simplicity, higher vibrationally excited states and states above the barrier are ignored.

from which we can determine  $n_0$ ,  $n_1$ ,  $n_-$  and  $n_+$ . The inelastic transition rate  $W_{pq}$  for any  $p$  and  $q$  can explicitly be obtained as an integral of products of the non-equilibrium electron distribution function ( $f(E)$ ):

$$f(E, eV) = \frac{1}{2}f_{FD}(E - \frac{eV}{2}) + \frac{1}{2}f_{FD}(E + \frac{eV}{2}) \quad (7.17)$$

It determines the states occupied with electrons which can excite vibrations and  $[1-f(E+\Delta, E)]$  which determines available states for electrons to scatter to after inelastic interaction with a vibration mode, and  $\Delta E$  is the energy exchanged. The rate is also proportional to electron-vibration coupling strength  $\gamma_{e-v}$  and the initial occupation of the level  $n_i$ . As already seen, the matrix elements for excitation from the ground states  $\Psi_0$  and  $\Psi_1$  to  $\Psi_+$  and  $\Psi_-$  are approximately determined by the projections  $\langle \Psi_A | \Psi_- \rangle$ ,  $\langle \Psi_B | \Psi_- \rangle$ ,  $\langle \Psi_A | \Psi_+ \rangle$  and  $\langle \Psi_B | \Psi_+ \rangle$  which depend on the tunnelling coupling  $\Delta$  and the splitting  $\Delta_0$ . We assume that  $\gamma_{e-v}$  and the electron density of states are energy independent which is a valid approximation as long as the scattering is happening within a wide conduction band, which is the case in our experiments. Explicitly, the rates are:

$$\begin{aligned} W_{-0} &= n_0 \int_{-\infty}^{\infty} \gamma_{e-v} \beta_+^2 f(E, eV) [1 - f(E - \hbar\omega_v - \Delta_0 + E_\Delta, eV)] dE \\ W_{0-} &= n_- \int_{-\infty}^{\infty} \gamma_{e-v} \beta_+^2 f(E, eV) [1 - f(E + \hbar\omega_v + \Delta_0 - E_\Delta, eV)] dE \\ W_{+0} &= n_0 \int_{-\infty}^{\infty} \gamma_{e-v} \beta_-^2 f(E, eV) [1 - f(E - \hbar\omega_v - \Delta_0 - E_\Delta, eV)] dE \\ W_{0+} &= n_+ \int_{-\infty}^{\infty} \gamma_{e-v} \beta_-^2 f(E, eV) [1 - f(E + \hbar\omega_v + \Delta_0 + E_\Delta, eV)] dE \\ W_{-1} &= n_1 \int_{-\infty}^{\infty} \gamma_{e-v} \alpha_+^2 f(E, eV) [1 - f(E - \hbar\omega_v + \Delta_0 + E_\Delta, eV)] dE \end{aligned}$$

$$\begin{aligned}
W_{1-} &= n_- \int_{-\infty}^{\infty} \gamma_{e-v} \alpha_+^2 f(E, eV) [1 - f(E + \hbar\omega_v - \Delta_0 - E_\Delta, eV)] dE \\
W_{+1} &= n_1 \int_{-\infty}^{\infty} \gamma_{e-v} \alpha_-^2 f(E, eV) [1 - f(E - \hbar\omega_v + \Delta_0 - E_\Delta, eV)] dE \\
W_{1+} &= n_+ \int_{-\infty}^{\infty} \gamma_{e-v} \alpha_-^2 f(E, eV) [1 - f(E + \hbar\omega_v - \Delta_0 + E_\Delta, eV)] dE \\
W_{+-} &= n_- \int_{-\infty}^{\infty} \gamma_{e-v} (\beta_+^2 \beta_-^2 + \alpha_+^2 \alpha_-^2) f(E, eV) [1 - f(E - 2E_\Delta, eV)] dE \\
W_{-+} &= n_+ \int_{-\infty}^{\infty} \gamma_{e-v} (\beta_+^2 \beta_-^2 + \alpha_+^2 \alpha_-^2) f(E, eV) [1 - f(E + 2E_\Delta, eV)] dE
\end{aligned} \tag{7.18}$$

Since  $\gamma_{e-v}$ , and the  $\alpha$ 's and  $\beta$ 's are constants, the general form of the integrals in (7.18) is,

$$\begin{aligned}
&\int_{-\infty}^{\infty} f(E, eV) [1 - f(E + \Delta E, eV)] dE \approx \\
&\Delta E + \frac{1}{4} \frac{\Delta E - eV}{e^{(\Delta E - eV)/k_B T} - 1}, \quad \Delta E > 0, |\Delta E/k_B T| \gg 1; \\
&\frac{1}{4} \frac{-\Delta E - eV}{e^{(-\Delta E - eV)/k_B T} - 1}, \quad \Delta E < 0, |\Delta E/k_B T| \ll 1.
\end{aligned} \tag{7.19}$$

Solving the system of linear equations (7.16) is a simple computational task and a small Mathematica routine was used for the calculation. Since the analytical expression is rather cumbersome the occupation numbers are presented graphically, as shown in Fig.(7.4) for the choice of parameters shown in the inset.

The parameters are chosen such as to clearly show the main characteristics of the model. Fits to real measured data will be presented below. Since the energy difference between the two lowest states in the left and right well of the TLS is much larger than the thermal energy at low bias there are no transitions between two states. In fact, there are no two-level transitions before the system gets excited from the ground level, so until molecular vibrations are excited. At zero bias voltage, only if the thermal energy is large enough that the system can be excited from  $\Psi_0$  to  $\Psi_-$ , the system can get into the other well. This is illustrated by the behavior of the occupation numbers in the example of Fig.(7.4). Before the molecular oscillation is triggered  $n_0$  is fully occupied, while all other occupation numbers are zero. This means that the system is stable in ground state  $\Psi_0$ . The dashed line at 55mV presents the vibration oscillation

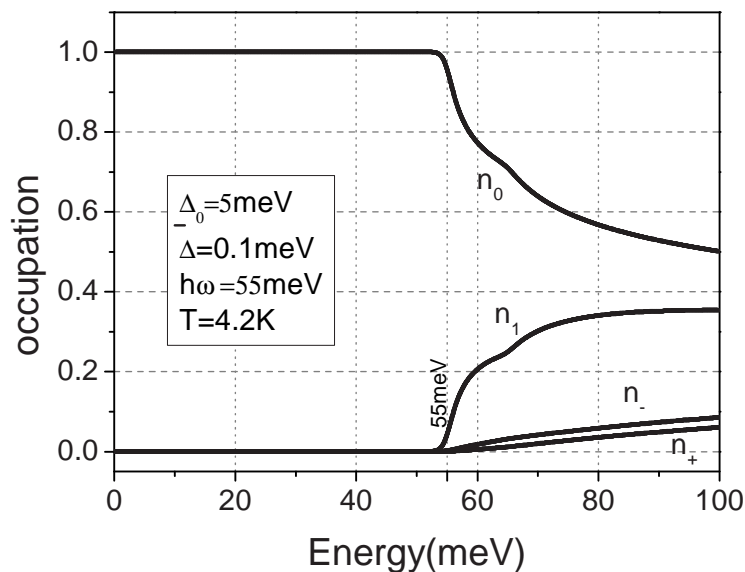


Figure 7.4: Occupation numbers of states  $\Psi_0$ ,  $\Psi_1$ ,  $\Psi_-$  and  $\Psi_+$  as a function of the bias voltage. The system is stable in the ground state  $\Psi_0$  until the excess energy of the electrons reaches the threshold of  $\hbar\omega$ .

energy. At that energy the system actually gets elevated to the state  $\Psi_-$ . That enables the tunnelling to the other well. The probability to tunnel is determined by Eq.(7.14) which is obviously much smaller than 1 for a reasonable choice of parameters. This means that the system, if started from  $\Psi_0$  is mostly localized in the left well. This holds viceversa if the system started initially from  $\Psi_1$ . After a new inelastic scattering event, the system relaxes in one of two wells, with the probability defined in (7.14). The number of excitations per second is proportional to the number of electrons with enough energy to excite a vibration which then bring the system in the excited state where it tunnels between the states, so the average occupation numbers of states  $\Psi_0$  and  $\Psi_1$  approaches to equal values at high bias. The occupations  $n_+$  and  $n_-$  are significantly lower than  $n_0$  and  $n_1$  since there are more electrons available for de-exciting the system as compared to the fraction that can initiate the excitation.

The current through the system is defined by the conductances of two possible configurations of the system. When we assume that the conductance is only determined by the weight of the molecular wave function in each of the wells we obtain,

$$I = (n_0 + \beta_+^2 n_- + \beta_-^2 n_+) \cdot \sigma_0 \cdot V + (n_1 + \alpha_+^2 n_- + \alpha_-^2 n_+) \cdot \sigma_1 \cdot V. \quad (7.20)$$

The existence of two different conductances  $\sigma_0$  and  $\sigma_1$  in two different configurations gives rise to a small step in the current, which is presented in Fig.(7.5) in panels 1a) and 1b). Whether the step will be up, like in the left panel, or

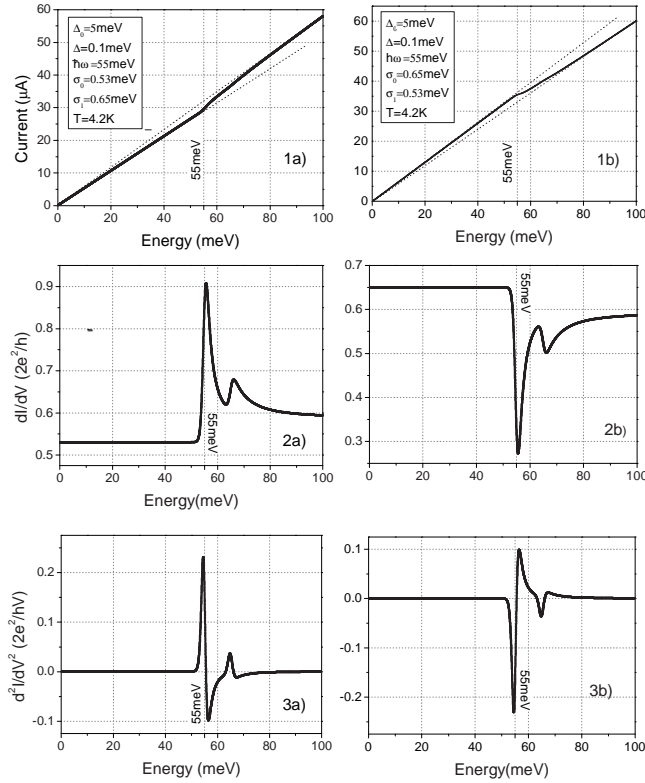


Figure 7.5: 1a) and 1b): Current through the TLS as a function of the voltage. In 1a) conductance  $\sigma_1 > \sigma_0$ , so the current increases, while in 2b) it is the opposite. 2a)  $dI/dV$  as a function of the bias voltage for the case  $\sigma_1 > \sigma_0$ , while 2b) is for  $\sigma_1 < \sigma_0$ . 3a) and 3b) are the second derivatives. There is a clear dip after each peak.

down, like in the panel on the right, will depend on the relative values of  $\sigma_0$  and  $\sigma_1$ . This difference can also be seen from the difference in slope before the vibration excitation energy at  $55 \text{ meV}$  and after. In both I-V curves, for bias voltages below  $55 \text{ meV}$ , the current shows a linear dependence on voltage with conductance  $\sigma_0$ , which changes above  $55 \text{ meV}$  and slowly converges to another slope which is now determined by  $\sigma_0$ ,  $\sigma_1$  and the set of occupation numbers  $\{n_0, n_1, n_-, n_+\}$ , which are energy dependent, but is approximately given by  $\frac{1}{2}\sigma_0 + \frac{1}{2}\sigma_1$ . The effect that the vTLS has on the conductance of the system is best seen in  $dI/dV$  and  $d^2I/dV^2$  curves, as presented in Fig.(7.5) 2a) and 2b) and 3d) and 3b) respectively. There are two peaks clearly visible in  $dI/dV$ . The first peak comes from excitation to the level  $\Psi_-$  which has significant weight  $\beta_+^2$  in the left well. The second peak arises from the level  $\Psi_+$  which is weakly populated in the left well, with weight  $\beta_-^2$ . Figure (7.6) shows how the shape and

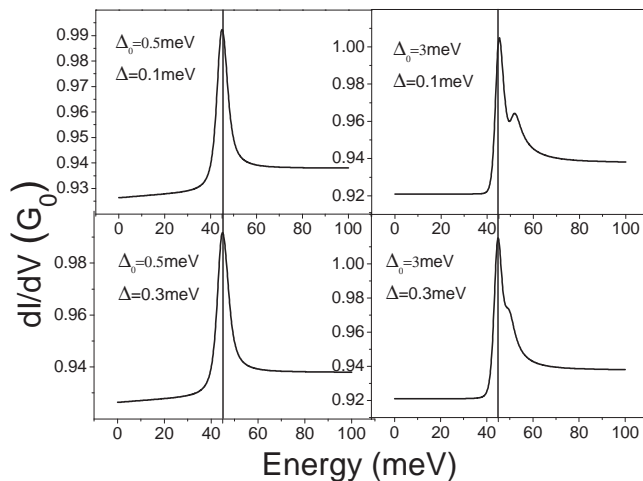


Figure 7.6: *Differential conductance in the vTLS model as a function of the bias for various choices of the energy splitting between two levels ( $2\Delta_0$ ) and the tunnelling coupling  $\Delta$ . The other parameters are kept fixed ( $\hbar\omega=45\text{meV}$ ,  $T=4.2\text{K}$ ,  $\sigma_0=0.921$  and  $\sigma_1=0.955$ ).*

the position of the peaks depend on the choice of the parameters. The model is controlled by six variables: temperature ( $T$ ), vibration frequency ( $\hbar\omega$ ), two conductances ( $\sigma_0$  and  $\sigma_1$ ), the energy splitting between two levels ( $2\Delta_0$ ) and the tunnelling coupling  $\Delta$ . The temperature determines the broadening  $k_B T$  of the Fermi-Dirac distribution in the leads. Although this should be fixed by the bath temperature we have seen in Chapter 6 that the width of the regular phonon step in  $dI/dV$  is larger than expected. For this reason we take  $T$  as a free variable. Since there is essentially no difference in vibration thermalization between experiments described by vTLF and OLM, we expect typical temperatures to be similar. Conductances  $\sigma_0$  and  $\sigma_1$  are roughly set by the observed conductance levels below and above the excitation. Since the total conductance below and above the excitation is determined by the occupation numbers, the optimal values for  $\sigma_0$  and  $\sigma_1$  will also be influenced by the variation of other parameters to a small extent. This can be seen from the difference in the conductances in the left end right panels in Fig.(7.6) where only  $\Delta_0$  was changed while all other parameter are kept constant. The primary fitting parameters in this model are  $\Delta_0$  and  $\Delta$  and the way their choice influences the shape of the curves is illustrated in Fig.(7.6). For  $\Delta_0 \gg \Delta, kT$ , we observe a double peak, which transforms into a single asymmetric peak when  $\Delta_0$  becomes a bit smaller. Note that a difference of only a few percent in  $\sigma_0$  and  $\sigma_1$  leads to a very pronounced peak in  $dI/dV$ .

### 7.3.4 The timescales

Molecular vibrations are inelastically excited and de-excited by electrons. The total number of electrons that inelastically excites molecular vibrations is around 1% of the total number of electrons being transported through the contact as one can judge from the typical step in  $dI/dV$  for regular vibration mode spectra. With a conductance  $\sim 1G_0$  and the bias voltage  $\sim 60\text{mV}$ , the current is  $\sim 5\mu\text{A}$  which means  $\sim 3 \cdot 10^{13}$  electrons per second passing through the contact which makes  $\sim 3 \cdot 10^{11}$  excitations per second. We assume that the lifetime of a single molecular excitation is longer than the tunnelling precession time so the system can relax in both wells. Typically, if  $\Delta_0 \approx 1\text{meV}$  and  $\Delta \approx 0.1\text{meV}$  this gives a precession frequency  $\tau^{-1} = \frac{\sqrt{\Delta_0^2 + \Delta^2}}{\hbar} \approx 1.6 \cdot 10^{-12}\text{s}^{-1}$ . From this is clear that the precession frequency depends only on the energy separation  $\Delta_0$  as long as  $\Delta \ll \Delta_0$ . If we assume that molecular vibrations can relax only through the electrons which are transported through the contact and that the coupling for relaxation is the same as for excitation, the average lifetime would be  $\sim 3 \cdot 10^{-12}$  s, thus the time scales are comparable.

## 7.4 Comparison to experiments and discussion

The above presented model will now be compared with experiments on Pt-H<sub>2</sub>-Pt molecular bridges. When fitting data one should keep in mind what can be expected from the model. Since the vTLS which we consider starts to be active only after the molecule becomes vibrationally excited the step down in the conductance due to regular electron-vibration scattering is unavoidably present above the excitation energy. This decrease is never larger than 3% of the zero bias conductance but it usually is much smaller. Since this inelastic scattering of the electrons is not treated in our vTLF model, we expect it to produce a small mismatch between calculated curves and data. The conductance step due to electron-vibration scattering in PCS is rather small and for vTLF processes with a difference in  $\sigma_0$  and  $\sigma_1$  larger than 10% it can be neglected. Generally, it should be possible to combine the vTLF model with the OLM to capture both effects since their influence on the conductance is rather independent. The inelastic scattering of electrons in the OLM changes  $\sigma_0$  and  $\sigma_1$  in the vTLF by approximately the same amount and it is only the difference that is relevant for describing the peaks in  $dI/dV$ . Another hindering feature unavoidably present in most of  $dI/dV$  curves are the conductance fluctuations originating from the multiple elastic scattering on the defects in the vicinity of the contacts. Due to energy dependent interference between the different electron paths the  $dI/dV$  signal becomes energy dependent even in the parts below the vibration excitations where the conductance should be flat. The left and right panels of Fig.(7.7) show fits to two selected measurements with small conductance fluctuations and having a quite large difference between the conductances above and below the peaks. Since the most sensitive parameters which determine the peak height are  $\sigma_0$  and  $\sigma_1$ , the match one should expect between the shape of the calculated

curve and experimentally measured data will strongly depend on the suppression of conductance fluctuations and the relative importance of PCS signal. By this fitting, we aim to assign physical meaning to the shape of the peaks in the  $dI/dV$  curves and the choice of parameters in the model. In the end, the most important feature of vTLF model will be the peak position which indicates the vibration frequency measured in experiment. It can be used even when conductance fluctuations are large because they do not influence the peak position and this makes it a powerful tool for detection of vibration modes of molecules. It should be noted that the quality of the fits is very good. The model captures the height of the peak in combination with the difference in conductance before and after the peak, and the asymmetric peak shape. The temperature is comparable to temperature obtained for PCS from OLM. The fits are rather insensitive to the value of  $\Delta$  as long as it is small.

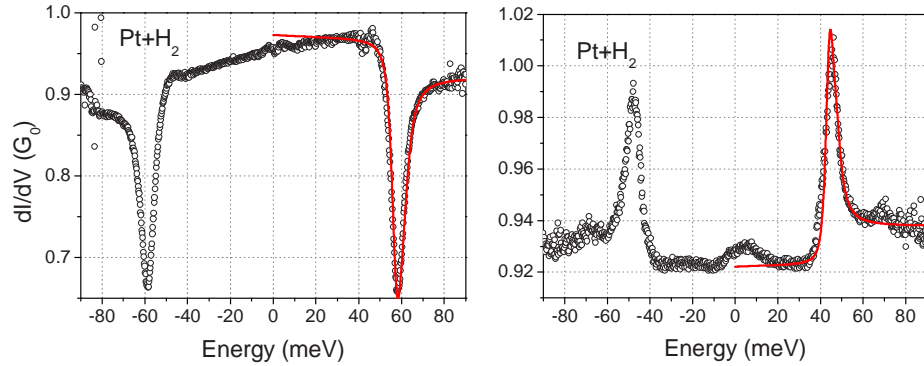


Figure 7.7: Dots represent experimental measurements of  $dI/dV$  as a function of bias and the line is a fit obtained by the vTLF model. The fitting parameters are: left panel- ( $\Delta_0=1\text{meV}$ ,  $\Delta=0.1\text{meV}$ ,  $\hbar\omega=58.5\text{meV}$ ,  $\sigma_0=0.98G_0$ ,  $\sigma_1=0.86G_0$ ,  $T=8.5\text{K}$ ) and right panel- ( $\Delta_0=1\text{meV}$ ,  $\Delta=0.3\text{meV}$ ,  $\hbar\omega=45\text{meV}$ ,  $\sigma_0=0.921G_0$ ,  $\sigma_1=0.955G_0$ ,  $T=7\text{K}$ ).

Since our measurements are done with MCBJ devices we have the possibility of mechanically changing the contact by stretching or relaxing the molecular bridge. Our vTLS exists only for a very particular contact geometry, so by stretching it or relaxing we can explore different geometries, and different heights of the double well potential barrier.

Figure (7.8) presents an example where, by stretching the contact, the molecule arrives in a geometry that produces vTLF's. The initial contact produces the uppermost curve which shows just a normal vibration features perhaps slightly affected by vTLF which results in sharp edges of the vibration step. The following curve is obtained on a configuration which is the same as the previous one, but stretched for about  $0.1\text{\AA}$ . The sharp peaks indicate vTLS, which means that upon the stretching a TLS is formed with a barrier height which enables vibration mode assisted tunnelling. Further stretching changes the system again into a stable configuration which gives normal PCS features. The conductances of

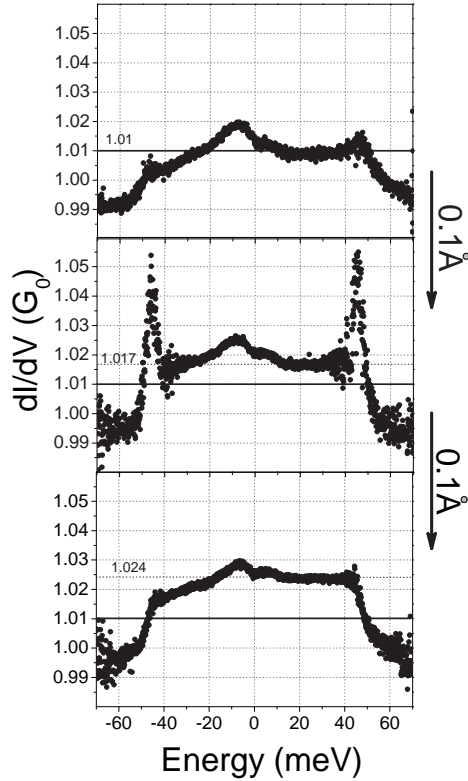


Figure 7.8: A sequence of three measurements for a contact where each next one is stretched for about  $0.1\text{\AA}$ . It can clearly be seen that a regular phonon structure evolves into a structure with peaks and with further stretching it returns again to a regular phonon shape. One should also notice that the zero bias conductance changes upon the stretching in the opposite manner than expected which suggest that the configuration was changed. The black line indicates the initial conductance while the dotted one is the conductance of the present junction.

the first and the last stable configuration are slightly different which indicates that the contact changed configuration. A small conductance decrease upon stretching was observed earlier (in chapter 4 for instance), but in this case the conductance increased with stretching. The middle panel shows the situation where the effects of increase in the conductance made by vTLS and the conductance decrease due to electron back scattering on vibrations are of comparable magnitude. The conductance in the vTLS model, after the vibration excitation ( $\sim (\sigma_0 + \sigma_1)/2$ ) is larger than the conductance before ( $\sigma_0$ ) which produces a peak, but still the increase is so small that the flat part after the peak is overruled by the conductance decrease due to vibration-electron scattering which is

of the order of 1%-3%. This agrees with the small size of the peaks. The series of Fig.(7.8) forms a very strong confirmation that vibration modes are involved in the mechanism responsible for anomalous peaks.

## 7.5 Conclusions

Inspired by anomalous differential conductance curves observed in PCS measurements on molecular bridges, we developed the model presented above. In the experiments presented in this thesis, the effect was observed with  $D_2$ ,  $H_2$ , HD, CO,  $C_2H_2$  and  $C_6H_6$  molecules in between Pt electrodes and for Pd with  $H_2$ . Similar effects were reported in other experiments with different contact metals and molecules (69; 70; 71), so it appears to be a general feature to molecule-metal junctions. The vTLF model can explain the sharp peaks and dips in  $dI/dV$  spectra, as presented above. The total number of 6 adjustable parameters is actually a good test to prove the reliability of the model. The excitation frequency is a well defined value and it has to agree with measurement where vTLF is not present. The broadening, presumably caused by the temperature, usually appears to be slightly higher than 4.2K. This is consistent with the broadening temperatures around 7K to 9K observed in PCS measurement. The two conductances,  $\sigma_0$  and  $\sigma_1$  can also take a very limited set of values because they determine the peak height as well as the difference in conductance before and after the peak.

The most important feature of the model is that it acts like an internal amplification system for molecular vibrations. Therefore, even if conductance fluctuations are large, like in the case of Pd+ $D_2$  presented in Fig.(7.1), the peaks are large and easily detectable. This is of special importance in case of molecules where the conductance is carried through the molecular orbitals which are not perfectly overlapping.

# Bibliography

- [1] M. Paulsson, F. Zahid, and S. Datta. *Resistance of a molecule*. CRC Press (2002).
- [2] B. J. van Wees, H. van Houten H., C. W. J. Beenakker, J. G. Williamson, L. P. Kouwenhoven, D. van der Marel, and C. T. Foxon. Quantised conductance of point contacts in a two-dimensional electron gas. *Phys. Rev. Lett.*, **60**, 848–850, (1988).
- [3] A. Yanson. *Atomic chains and electronic shells: quantum mechanisms for the formation of nanowires*. Rijksuniversiteit Leiden, phd thesis edition, (2001).
- [4] R. Landauer and M. Buttiker. Resistance of small metallic loops. *Phys. Rev. Lett.*, **54**, 2049–2052, (1985).
- [5] A. I. Yanson, G. Rubio Bollinger, H. E. van den Brom, N. Agraït, and J. M. van Ruitenbeek. Formation and manipulation of a metallic wire of single gold atoms. *Nature*, **395**, 783–785, (1998).
- [6] C. J. Muller, J. M. van Ruitenbeek, and L. J. de Jongh. Experimental observation of the transition from weak link to tunnel junction. *Physica C*, **191**, 485–504, (1992).
- [7] H. E. van den Brom. *Noise properties of atomic-size contacts*. PhD thesis, Universiteit Leiden, The Netherlands, (2000).
- [8] A. I. Yanson, I. K. Yanson, and J. M. van Ruitenbeek. Observation of shell structure in sodium nanowires. *Nature*, **400**, 144–146, (1999).
- [9] N. Agraït, A. Levy Yeyati, and J. M. van Ruitenbeek. Quantum properties of atomic-sized conductors. *Phys. Rep.*, **377**, 81–279, (2003).
- [10] R. H. M. Smit, C. Untiedt, G. Rubio-Bollinger, R. C. Segers, and J. M. van Ruitenbeek. Observation of a parity oscillation in the conductance of atomic wires. *Phys. Rev. Lett.*, **91**, 076805, (2003).
- [11] C. Muller. *An experimental study on mechanically controllable break junctions*. Rijksuniversiteit Leiden, phd thesis edition, (1992).

- [12] K. H. Gundlach. *Solid State Electron*, **946**, 12485–12507, (1966).
- [13] O. Yu. Kolesnychenko, O. I. Shklayarevskii, and H. van Kempen. Calibration of the distance between electrodes of mechanically controlled break junctions using field-emission resonance. *Rev. Sci. Instrum.*, **70**, 1442–1446, (1999).
- [14] C. Untiedt, A. I. Yanson, R. Grande, G. Rubio-Bollinger, N. Agrait, S. Vieira, and J. M. van Ruitenbeek. Calibration of the length of a chain of single gold atoms. *Phys. Rev. B*, **66**, 85418, (2002).
- [15] J.K. Viljas, J.C. Cuevas, F. Pauly, and M.Häfner. Electron-vibration interaction in transport through the atomic gold wires. *Phys. Rev. B*, **72**, (2005).
- [16] M.Paulsson, T. Frederiksen, and M. Brandbyge. Modeling inelastic phonon scattering in atomic- and molecular-wire junctions. *Phys. Rev. B*, **72**, 201101(R), (2005).
- [17] B. Ludoph and J. M. van Ruitenbeek. Conductance fluctuations as a tool for investigating the quantum modes in atomic-size metallic contacts. *Phys. Rev. B*, **61**, 2273–2285, (2000).
- [18] B. Ludoph. *Quantum conductance properties of atomic-size contacts*. PhD thesis, Universiteit Leiden, The Netherlands, (1999).
- [19] B. Ludoph, M. H. Devoret, D. Esteve, C. Urbina, and J. M. van Ruitenbeek. Evidence for saturation of channel transmission from conductance fluctuations in atomic-size point contacts. *Phys. Rev. Lett.*, **82**, 1530–1533, (1999).
- [20] R. H. M. Smit, Y. Noat, C. Untiedt, N. D. Lang, M. C. van Hemert, and J. M. van Ruitenbeek. Measurement of the conductance of a hydrogen molecule. *Nature*, **419**, 906–909, (2002).
- [21] R. Smit. *From Quantum Point Contacts to Monoatomic Chains: Fabrication and Characterization of the Ultimate Nanowire*. Rijksuniversiteit Leiden, phd thesis edition, (2002).
- [22] A. Aviram and M. A. Ratner. Molecular rectifiers. *Chem. Phys. Lett.*, **29**, 277–283, (1974).
- [23] M. A. Reed, C. Zhou, C. J. Muller, T. P. Burgin, and J. M. Tour. Conductance of a molecular junction. *Science*, **278**, 252–254, (1997).
- [24] C. Kergueris, J.-P. Bourgoin, S. Palacin, D. Esteve, C. Urbina, M. Magoga, and C. Joachim. Electron transport through a metal-molecule-metal junction. *Phys. Rev. B*, **59**, 12505–12513, (1999).

- [25] J. Reichert, R. Ochs, D. Beckmann, H. B. Weber, M. Mayor, and H. von Löhneysen. Driving current through single organic molecules. *Phys. Rev. Lett.*, **88**, 176804, (2002).
- [26] X. D. Cui, A. Primak, X. Zarate, J. Tomfohr, O. F. Sankey, A. L. Moore, T. A. Moore, D. Gust, L. A. Nagahara, and S. M. Lindsay. Changes in the electronic properties of a molecule when it is wired into a circuit. *J. Phys. Chem. B*, **106**, 8609–8614, (2002).
- [27] L. A. Bumm, J. J. Arnold, M. T. Cygan, T. D. Dunbar, T. P. Burgin, L. Jones II, D. L. Allara, J. M. Tour, and P. S. Weiss. Are single molecular wires conducting? *Science*, **271**, 1705–1707, (1996).
- [28] J. Park, A. N. Pasupathy, J. I. Goldsmith, C. Chang, Y. Yaish, J. R. Petta, M. Rinkoski, J. P. Sethna, H. D. Abruña, P. L. McEuen, and D. Ralph. Coulomb blockade and the Kondo effect in single atom transistors. *Nature*, **417**, 722–725, (2002).
- [29] W. Liang, M. P. Shores, M. Bockrath, J. R. Long, and H. Park. Kondo resonance in a single-molecule transistor. *Nature*, **417**, 725–729, (2002).
- [30] S. Kubatkin, A. Danilov, M. Hjort, J. Cornil, J.-L. Brédas, N. Stühr-Hansen, P. Hedegård, and T. Bjørnholm. Single-electron transistor of a single organic molecule with access to several redox states. *Nature (London)*, **425**, 698–701, (2003).
- [31] B. Xu and N. J. Tao. Measurement of single-molecule resistance by repeated formation of molecular junctions. *Science*, **301**, 1221–1223, (2003).
- [32] Y. García, J. J. Palacios, E. SanFabián, J. A. Vergés, A. J. Pérez-Jiménez, and E. Louis. Electronic transport and vibrational modes in a small molecular bridge: H<sub>2</sub> in Pt nanocontacts. *Phys. Rev. B*, **69**, 041402, (2004).
- [33] J. C. Cuevas, J. Heurich, F. Pauly, W. Wenzel, and G. Schön. Theoretical description of the electrical conduction in atomic and molecular junctions. *Nanotechnology*, **14**, R29–R38, (2003).
- [34] K. S. Thygesen and K. W. Jacobsen. Conduction mechanism in a molecular hydrogen contact. *Phys. Rev. Lett.*, **94**, 036807, (2005).
- [35] D. Djukic, K. S. Thygesen, C. Untiedt, R. H. M. Smit, K. W. Jacobsen, and J. M. van Ruitenbeek. Stretching dependence of the vibration modes of a single-molecule Pt-H<sub>2</sub>-Pt bridge. *Phys. Rev. B*, **71**, 161402,, (2005).
- [36] V.M.Garcia-Suarez, A.R.Rocha, S.W.Bailey, C.J.Lambert, and J.Ferrer S.Sanvito. Single channel conductance of h<sub>2</sub> molecules attached to platinum or palladium electrodes. Preprint, cond-matt/0412726.
- [37] S. Datta. *Electronic Transport in Mesoscopic Systems*. Cambridge University Press, Cambridge, UK, (1997).

- [38] K. S. Thygesen and K. W. Jacobsen. *Phys. Rev. Lett.*, **91**, 146801, (2003).
- [39] M. Brandbyge, J. Taylor, K. Stokbro, J.-L. Mozos, and P. Ordejon. Density functional method for nonequilibrium electron transport. *Phys. Rev. B*, **65**, 165401, (2002).
- [40] B. Hammer and J.K. Nørskov. Electronic factors determining the reactivity of metal surfaces.
- [41] J.K. Nørskov, A. Houmøller, P.K. Johansson, and B.I. Lundqvist. Adsorption and dissociation of  $\text{H}_2$  on mg surfaces. *Phys. Rev. Lett.*, **46**, 257, (1981).
- [42] W. Schottky. Über spontane Stromschwankungen in verschiedenen Elektrizitätsleitern. *Ann. Phys. (Leipzig)*, **57**, 541–567, (1918).
- [43] A. van der Ziel. *Noise in Solid State Devices*. Wiley, New York, (1986).
- [44] H. Birk, M.J.M de Jong, and C. Schonenberger. Shot-noise suppression in the single-electron tunneling regime. *Phys. Rev. Lett.*, **75**, 1610, (1995).
- [45] Ya. M. Blanter and M. Büttiker. Shot noise in mesoscopic conductors. *Phys. Rep.*, **336**, 2–166, (2000).
- [46] A. F. Andreev. The thermal conductivity of the intermediate state in superconductors. *Sov. Phys. JETP*, **19**, 1228–1231, (1964).
- [47] A. H. Steinbach, J. M. Martinis, and M. H. Devoret. Observation of hot-electron shot noise in a metallic resistor. *Phys. Rev. Lett.*, **20**, 3806–3809, (1996).
- [48] M. Büttiker. Scattering theory of thermal and excess noise in open conductors. *Phys. Rev. Lett.*, **65**, 2901–2904, (1990).
- [49] P. Horowitz and W. Hill. *The Art of Electronics*. Cambridge University Press, Cambridge, (1989).
- [50] H. Pothier, S. Gueron, N. O. Birge, D. Esteve, and M. H. Devoret. Energy distribution function of quasiparticle in mesoscopic wires. *Phys. Rev. Lett.*, **18**, 3490–3493, (1997).
- [51] L.D. Landau and E.M. Lifshitz. *Statistical Physics*. Pergamon, Oxford, (1959).
- [52] M. Büttiker. Scattering theory of current and intensity noise correlations in conductors and wave guides. *Phys. Rev. B*, **46**, 12485–12507, (1992).
- [53] G. B. Lesovik. Excess quantum noise in 2d ballistic point contacts. *Sov. Phys. JETP Lett.*, **49**, 592–594, (1989). [*Pis'ma Zh. Eksp. Teor. Fiz.* **49** (1989) 513].

- [54] M. Reznikov, M. Heiblum, H. Shtrikman, and D. Mahalu. Temporal correlation of electrons: suppression of shot noise in a ballistic quantum point contact. *Phys. Rev. Lett.*, **75**, 3340–3343, (1995).
- [55] A. Kumar, L. Saminadayar, D. C. Glattli, Y. Jin, and B. Etienne. Experimental test of the quantum shot noise reduction theory. *Phys. Rev. Lett.*, **76**, 2778–2781, (1996).
- [56] C. J. Muller, J. M. van Ruitenbeek, and L. J. de Jongh. Conductance and supercurrent discontinuities in atomic-scale metallic constrictions of variable width. *Phys. Rev. Lett.*, **69**, 140–143, (1992).
- [57] H. E. van den Brom and J. M. van Ruitenbeek. Quantum suppression of shot noise in atom-size metallic contacts. *Phys. Rev. Lett.*, **82**, 1526–1529, (1999).
- [58] P. Hansma. Inelastic electron tunneling. *Physics Reports*, **30C**, 145,, (1977).
- [59] E. Zarate, P. Apell, and P.M. Echenique. Calculation of low-energy-electron lifetimes. *Phys. Rev. B*, **60**, 2326, (1999).
- [60] A. Downes, Ph. Dumas, and M.E. Welland. Measurement of high electron temperature in single atom metal point contacts by light emission. *Appl. Phys. Lett.*, **81**, 1252, (2002).
- [61] Roberto D’Agosta, Na Sai, and Massimiliano Di Ventra. Local electron heating in nanoscale conductors. *Preprint, cond-mat/0605312*.
- [62] Roberto D’Agosta and Massimiliano Di Ventra. Hydrodynamic approach to transport and quantum turbulence in nanoscale conductors. Preprint, cond-mat/0512326.
- [63] Y.C. Chen and M. Di Ventra. Effect of electron-phonon scattering on shot noise in nanoscale junctions. *Phys. Rev. Lett.*, **95**, 166802, (2005).
- [64] M. Strange, K. S. Thygesen, and K. W. Jacobsen. Electron transport in Pt-CO-Pt nanocontacts: First principles calculations. Preprint, cond-mat/0512138.
- [65] M. Strange and K. W. Jacobsen. Pt-CO: vibrations. Private communications.
- [66] S.N.Krainyukov, A.V.Khotkevich, I.K.Yanson, A.V.Zhalko-Titarenko, V.N.Antonov, and V.N.Nemoshkalenko. *Sov. J. Low Temp. Phys.*, **14**, 127, (1988).
- [67] W. Ho. Single-molecule chemistry. *Journal of Chemical Physics*, **117**, 1103, (2002).
- [68] M. Kiguchi, D. Djukic, and J. M. van Ruitenbeek. Design of a gear for gas dosing at low temperatures. In preparation.

- [69] J.Gaudioso, L.J.Lauhon, and W. Ho. Vibrationally mediated negative differential resistance in a sigle molecule. *Phys. Rev. Lett.*, **85**, 1918,, (2000).
- [70] J.A.Gupta, C.P.Lutz, A.J.Heinrich, and D.M.Eigler. Strongly coverage-dependent excitations of adsorbed molecular hydrogen. *Phys. Rev. B*, **71**, 115416, (2005).
- [71] W. Wang, T. Lee, I. Kretzchmar, and M. Reed. Inelastic electron tunneling spectroscopy of an alkanedithiol self-assembled monolayer. *Nano Lett.*, **4**, 643,, (2004).
- [72] A. Nitzan and M. Ratner. Electron transport in molecular wire junctions. *Science*, **300**, 1384, (2003).

# Samenvatting

De samenleving stimuleert constante verbetering van bestaande apparaten en de mate van succes hiervan kan wellicht het beste worden waargenomen in de wereld van elektronische apparatuur. Elektronische schakelingen zijn in complexiteit, functionaliteit en betrouwbaarheid enorm verbeterd, maar de limieten zijn in zicht. Een nieuwe sprong voorwaarts die de deur kan openen naar verdere ontwikkeling is het concept van moleculaire elektronica waarin organische moleculen met hun natuurlijke eigenschappen de functionele onderdelen vormen. Het in dit proefschrift beschreven onderzoek is een klein aandeel in de totale inspanningen die de wetenschappelijke gemeenschap hiertoe levert. Het specifieke doel van dit onderzoek was het vervaardigen van een modelsysteem waarmee meettechnieken kunnen worden bestudeerd en rekenmodellen getest op weg naar complexere moleculen die de bouwstenen zullen vormen van de moleculaire elektronica.

Ons modelsysteem is de meest eenvoudige elektrische schakeling die men zich kan voorstellen: een Pt-H<sub>2</sub>-Pt moleculair contact. Met onze meetopstelling kan men de elektrische potentiaal over het molecuul controleren en de bijbehorende stroom meten. Middels een speciaal hiervoor ontworpen mechanisme kunnen atomaire contacten herhaaldelijk op gecontroleerde wijze uiteengetrokken en weer samengevoegd worden. Ook kan het Pt-H<sub>2</sub>-Pt moleculair contact met sub-ångstrom precisie opgerekt worden zonder het te breken. Feitelijk worden op deze manier de chemische Pt-H en H-H bindingen verlengd.

Onze experimenten worden uitgevoerd in vacuüm bij de temperatuur van vloeibaar helium, waar alle thermisch mechanische vibraties zijn bevroren. Zoals beschreven in hoofdstuk 1 van dit proefschrift, leidt verhoging van de spanning over het contact tot versnelling van de elektronen door de moleculaire brug. Bij een gegeven spanning zullen de elektronen voldoende energie hebben om een mechanische vibratie van het molecuul aan te slaan, hetgeen wordt waargenomen als een geringe afname in de geleiding. Omdat het molecuul in verschillende richtingen kan trillen waarbij iedere richting een eigen frequentie heeft, kunnen deze afzonderlijk waargenomen worden in een meting aan de differentiële geleiding.

Het enige probleem hierbij is dat we niet weten welke energie correspondeert met welke richting, daar het systeem niet optisch beschouwd kan worden. Dit probleem kunnen we aanpakken door te bestuderen hoe de vibratie-energie van de oprekking van het contact afhangt. Deze techniek is ontwikkeld en toegepast tijdens de in dit proefschrift beschreven experimenten. In hoofdstuk 2 tonen we

de experimentele resultaten aan  $H_2$ ,  $D_2$  en  $HD$  en vergelijken we deze met theoretisch verkregen resultaten. De energieën van de verschillende vibratierichtingen schalen met de wortel van de molecuulmassa hetgeen leidt tot een duidelijk zichtbare verschuiving van de energie na isotopsubstitutie.

Elektronen verplaatsen zich door geleidingskanalen, hetgeen feitelijk de moleculaire elektronbanen zijn. Een belangrijke kwestie is het aantal geleidingskanalen die aan het transport bijdragen en de mate waarin deze aan de geleiding bijdragen. Deze meting wordt behandeld in hoofdstuk 3 en deze tonen aan dat voor moleculaire Pt- $D_2$ -Pt contacten dat aantal één is, hetgeen ook duidelijk laat zien dat we de stroom door een enkel molecuul meten.

Toen we eenmaal de technieken en interpretaties van dit eenvoudige systeem onder de knie hadden, probeerden we ingewikkelder moleculen in onze schakeling toe te passen. De pogingen voor koolstofmonoxide ( $CO$ ) worden behandeld in hoofdstuk 4 terwijl de hoofdstukken 5 en 6 de metingen aan acetyleen ( $C_2H_2$ ) en benzeen ( $C_6H_6$ ) tonen. De complexiteit van het probleem is reeds zichtbaar op het niveau van deze nogal eenvoudige moleculen gezien het feit dat de gedane metingen en berekeningen geen eenvoudig beeld boden zoals in het geval van  $H_2$ . De gegeven gedeeltelijke antwoorden geven echter een duidelijke richting voor verder onderzoek.

Een volledig nieuwe techniek om vibratietoestanden te identificeren wordt gepresenteerd in hoofdstuk 7. Dit zijn vibratiegeïnduceerde tweenniveauctuaties in moleculaire bruggen. Het model demonstreert hoe we gebruik kunnen maken van afwijkende differentiële geleidingskrommen, die worden gezien bij alle door ons bestudeerde moleculen. Het biedt een krachtig stuk gereedschap om moleculaire contacten waarbij de metingen door sterke geleidingsfluctuaties vertroebeld worden toch te analyseren, daar het effect zo uitgesproken is.

De experimenten uit hoofdstuk 2 en 7 bieden een solide en betrouwbare basis terwijl de hoofdstukken 4, 5 en 6 een duidelijke route voor toekomstige experimenten vastleggen op weg naar volledig begrip van het gedrag van moleculaire contacten.

# List of publications

1. **D. Djukić** and J. M. van Ruitenbeek, "Shot noise measurements on a single molecule", Nano Lett. **6**(4) (2006) 789-793
2. **D. Djukić**, K.S. Thygesen, C. Untiedt, R.H.M. Smit, K.W. Jacobsen, and J.M. van Ruitenbeek, "Stretching dependence of the vibration modes of a single-molecule Pt-H<sub>2</sub>-Pt bridge.", Phys Rev. B **71**, 161402(R)(2005)
3. C. Untiedt, D.M.T. Dekker, **D. Djukić**, and J.M. van Ruitenbeek, "Absence of magnetically-induced fractional quantization in atomic contacts", Phys Rev. B **69**, 081401(R) (2004)
4. J.M. van Ruitenbeek and **D. Djukić**, in: "Simple model systems: from atoms to molecules", M. Reed, editor, Oxford University Press, in print.
5. W.H.A.Thijssen, **D. Djukić**, A.F. Otte, R.H. Bremmer and J.M. van Ruitenbeek, "Vibration induced two level systems in single-molecule junctions" (accepted for publication in Phys Rev Lett (2006))
6. **D. Djukić**, O. Tal, M. Kiguchi, M. Strange, K.W. Jacobsen and J.M. van Ruitenbeek, "Investigation of single molecule CO junctions".(in preparation)
7. M. Kiguchi, **D. Djukić** and J.M. van Ruitenbeek, "Conductance properties of a single C<sub>6</sub>H<sub>6</sub> molecule in electrical circuit". (in preparation)
8. M. Kiguchi, M. Krieger, O. Tal, R. Hortensius, **D. Djukić**, and J.M. van Ruitenbeek, "Design of a gas doser for low temperature break junctions". (in preparation)
9. M. Kiguchi, R. Stadler, **D. Djukić**, K.W. Jacobsen and J.M. van Ruitenbeek, "Evidence for H decorated Pt atomic chains". (in preparation)
10. M. Kiguchi, **D. Djukić** and J.M. van Ruitenbeek, "Bonding effect of CO molecules on the conductance of atomic metal wires". (in preparation)

# Curriculum Vitae

November 12th, 1974	Born in Tuzla (Bosnia and Herzegovina)
1980-1988	Primary School (Cavtat - Croatia)
1988-1994	High School (Belgrade - Serbia)
1994-2002	Study of Theoretical Physics at the University of Belgrade (Serbia). During the summer 2000, I spent 3 months at Hahn-Meitner Institute in Berlin in the group of Dr. C. Pettenkofer
2002-2006	Ph.D. student at the Leiden University Supervisor: Prof. Dr. J.M. van Ruitenbeek